Microplasma-Enabled Sputtering of Nanostructured Materials for the Agile Manufacture of Electronic Components

by

Yosef S. Kornbluth

B.A Physics and Mathematics
Yeshiva University, 2016
S.M Mechanical Engineering
Massachusetts Institute of Technology, 2018

SUBMITTED TO THE DEPARTMENT OF MECHANICAL ENGINEERING
IN PARTIAL FULFILLMENT OF THE REQUIREMENTS FOR THE DEGREE OF

DOCTOR OF PHILOSOPHY

AT THE

MASSACHUSETTS INSTITUTE OF TECHNOLOGY

SEPTEMBER 2021

Signature of Author:……
Department of Mechanical Engineering
July 7, 2021

Certified by:……
Luis Fernando Velásquez-García
Principal Research Scientist, Microsystems Technology Laboratories
Thesis Supervisor

Certified by:……
Joseph Jacobson
Associate Professor of Mechanical Engineering and Media Arts and Sciences
Thesis Committee Chair

Accepted by:……..…….
Nicolas Hadjiconstantinou
Professor of Mechanical Engineering
Chairman, Committee for Graduate Students

Microplasma-Enabled Sputtering of Nanostructured Materials for the Agile Manufacture of Electronic Components

by

Yosef S. Kornbluth

Submitted to the Department of Mechanical Engineering on
July 7, 2021, in partial fulfillment of the requirements for the
degree of Doctor of Philosophy in Mechanical Engineering

ABSTRACT

Additive manufacturing has revolutionized the low-volume manufacturing space; for example, polymers can be extruded and joined together to produce arbitrary shapes at the push of a button. However, this revolution is primarily confined to thermoplastics, and more broadly, to structural materials. The ability to add electronic capabilities to these printed shapes would greatly enhance their utility. Unfortunately, most additive manufacturing methods for conductive features do not produce high-quality films, or require processing that can damage printed surfaces.

Cleanroom technology is unmatched in its ability to produce high-resolution, high-quality interconnects and electronic features, but it has rigid requirements. The best results require precision equipment, tightly controlled environments, and are limited to patterning planar wafers and removing unwanted material to produce the desired patterns.

This thesis develops and demonstrates the capabilities of a microplasma-based atmospheric-pressure sputterer, which combines the strengths of both. This microsputterer was developed in order to achieve a direct-write method to deposit arbitrary patterns of electronics-quality thin films for additive manufacturing at room temperature. It uses a sputtering plasma, scaled down to millimeter scale and operated at atmospheric pressure, without the benefit of pre- or post-processing, and with a minimally controlled environment. Process parameters' impact on the material and manufacturing properties (i.e., adhesion, conductivity, resolution, speed) of the deposits are discussed.

The results of this thesis include near-bulk electrical conductivity for gold films with sub-millimeter resolution and significantly better adhesion than traditionally sputtered films, and alumina films with a breakdown strength that surpasses the state of the art. The printer's multimaterial capabilities and control over the sheath gas will allow for the creation of objects made of different materials with different electrical properties. This capability allows for the demonstration of practical applications that showcase the printer's capabilities, including an ultrathin capacitor, produced entirely through microplasma sputtering.

Thesis Supervisor: Luis Fernando Velásquez-García

Title: Principal Research Scientist, Microsystems Technology Laboratories

Table of Contents

Table of Figures

Table of Tables

Acknowledgments

No significant work can be done alone, and this is no exception. I would like to express my gratitude to everyone who helped.

First and foremost, this could not have happened without the support, both practical and emotional, of my wife Yulia. She allowed me to focus on my work while expertly handled the rest of our life, busy as she was. As importantly, she allowed me to focus not just on my work, by reminding me of the other important things in life. “Our printer” is finally finished.

To Shevi, who offered to share her crayons when my printer wasn’t making the lines I needed. May she see the fun in grown-up toys, but not too soon. And to Rachel, who lives as a reminder that happiness is not dependent on research progress. Keep smiling!

To Luis, for balancing guidance and letting me forge my own path. My first mystery novel, The Case of the Missing Tweezers, will come out soon. To my labmates, for the comradery and help: Anthony, Ashely, Zhumei, Brenda, and Hyeonseok.

To the rest of the numerous people who helped at MIT: Lalitha, whose expertise guided me into the world of microelectronics, and to Rick, who showed me that you don’t have to leave tinkering behind. To the MTL staff, who keep this place running and the argon flowing. To the many faculty and staff who give freely of their expertise and equipment to complete strangers: Carl Thompson, Alan Schwartzman, Tim McClure, Ian Hunter, and Aubrey Penn, among others.

This thesis is merely the culmination of a long journey. To my father, who taught me to always ask questions and to my mother, who taught that if something is worth doing, it’s worth doing right. To Dr. Berliner, who introduced me to physics, and Dr. Buldyrev, who introduced me to the joy of research.

To my committee: Joe, Tayo, and Dave, for helping guide me towards perfecting this thesis. I appreciate the help, and hope you enjoy reading this as much as I enjoyed the research.

Most of all, to God, for the opportunities I have been given. The journey has been enlightening; I hope for Your continued guidance in the next steps. I appreciate the glimpse into Your universe.

Chapter 1 – **Introduction**

1.1. Motivation

This thesis will be devoted to the development, characterization, and demonstration of a microplasma sputterer. Microplasma sputtering is a useful tool for the direct-write (i.e., without the use of a static template), that, without the need of any preprocessing or postprocessing, can deposit electronic-quality ultrathin layers on a freeform surface to create electrical components. This chapter will motivate this work by examining the state of electronics manufacturing as compared to manufacturing in general. It will then describe the current state of the art in other direct-write methods for similarly-scaled electronic-quality features. Afterwards, some potential applications for a direct-write capability for microelectronics are described. Sputtering and the accompanying plasma physics will be introduced, inasmuch is necessary for this thesis. Next, the chapter will describe microsputtering—a novel form of sputtering that occurs at small length scales at or near atmospheric pressure, and describe the state-of-the-art in that field. Finally, with that background, the chapter will introduce the rest of the thesis.

1.1.1. Electronics State-of-the-Art

Through the spending of much effort and time, humanity has become very good at creating finely patterned, high-quality electronic components. CMOS manufacturing, through a combination of lithography, coating, and etching, can reliably create features measured in nanometers, made of a variety of materials, with well-controlled and repeatable material properties on planar, smooth, non-porous substrates. These features can be layered and combined in many ways to produce a great variety of electronic components for an astoundingly low per-component cost and monolithically lay out such components in a small surface as integrated circuits for a relatively low per-unit cost.

Specialty circuits, not produced in enough volume to deserve their own integrated circuit, can be constructed with a printed circuit board. Printed circuit boards use larger (> 100 μm) traces to join discrete components that are soldered onto the board. However, the manufacture of printed circuit boards is also a rigid system, requiring a (less precise) manufacturing process, a pattern, soldering, and a planar surface. While the cost to pattern a single board is much lower, and the cost per-board is reasonable, there is a relatively high per-component cost. Whereas an integrated circuit can affordably have billions of components, a printed circuit board with thousands is already prohibitively expensive.

These two manufacturing processes occupy the majority of electronics manufacturing: integrated circuits for large-volume, large-complexity circuits; and printed circuit boards for medium-volume, medium complexity circuits.

1.2. Additive Manufacturing

However, there is still room for innovation at the low-volume end of the industry. To understand this, an examination of physical (i.e., non-electronic) manufacturing is illustrative.

Physical manufacturing, like electronic manufacturing, has a variety of options depending on the volume of manufacturing. Injection molding requires expensive molds, but once the mold is made, the per-unit cost is very low and high-resolution features are possible. Thermoforming, on the other hand, has lower fixed costs, but higher per-unit costs. However, a new technology has captured the low-volume section of the market: additive manufacturing.

Additive manufacturing, sometimes referred to as 3-D printing, excels at low-volume scales. Additive manufacturing typically involves the deposition layer by layer of a material in a pattern defined by a 3-D model of the desired object; that material is fused together into the desired shape. Very little material is wasted and very little is removed from the finished product. This contrasts with traditional manufacturing, which often (e.g., milling) involves subtractive elements.

Because the shape of an additively manufactured object is defined by the movement of a depositing source (nozzle) according to a computer-generated pattern, rather than by the use of a mold, there is minimal economy of scale. While a single object is relatively simple to produce, multiple copies of an object merely repeat the single-object manufacturing process multiple times, with no reusable template that can save time. Thus, additive manufacturing is suited to low-volume manufacturing, such as prototyping, hobbyist-level production, and customized prosthetics. In addition, additive manufacturing has been shown to produce complex geometries at a lower cost, including objects composed of multiple structures made of different materials.

Additive manufacturing centers on the extrusion of plastics and subsequent fusing, either through heat (Fused Deposition Modeling, FDM, also known as Fused Filament Fabrication, FFF) or photopolymerization (Stereolithography, SLA), and on consolidation of objects from powder feedstock, integrated with photons or electrons via melting (Powder Bed Fusion, PBF, and Direct Energy Deposition, DED) [1:1]. The former group is specific to plastics, while the latter group is focused on metals. Polymers, in contrast to metals, have a softening temperature low enough to enable extrusion and subsequent hardening, and polymers, unlike metals, have the chemistry necessary to react to light in a way for photopolymerization to work. On the other hand, metal additive manufacturing requires high temperatures and powers; the thermal gradients involved in the process often cause flaws in the microstructure. Nonetheless, additive metal manufacturing is used for structural objects.

1.3. Direct-Write Methods

Fortunately, for the purposes of electronics manufacture, true 3-D printing, i.e., the assembly of arbitrary shapes in all three dimensions, is rarely necessary. Instead, 2.5-D printing, or the addition of thin layers to already existing three-dimensional surfaces, is sufficient. An interconnect or sensor does not need to have a specific height, it merely needs to follow the contours of an existing shape. Thus, for the purposes of electronics manufacture, it is unnecessary to achieve the volume printing of standard additive manufacturing. Nonetheless, the challenge of producing 2.5-D traces of conductive materials is a challenge. Several methods have been developed to meet this challenge. Several review articles are included in the references [1:2]-[1:5]

and several of the most mature technologies are summarized in this section (Table 1-1).

Method	Summary	Advantages	Disadvantages
Conductive Ink	Nanoparticles suspended in liquid binder are deposited; binder removed. Often annealed	Resolution (1-10 µm best), conductivity (if annealed), mature, cost	Conductivity (if not annealed), high temperature (if annealed), silver only
LIFT	Laser melts droplets off of "toner ribbon"; droplets coalesce into film	Resolution, conductivity, material choice	Heating, ribbon is used quickly
FIBID	Precursor flows over substrate; ion beam dissociates metal from organic byproduct. Byproduct removed	Nanoscale resolution	Expensive equipment, poor film conductivity, limited material choice, substrate damage
Microsputtering	Plasma strips atoms from wire; combine on substrate	Cost, conductivity, adhesion, material choice, no heating	Immature, speed, resolution (without shadow mask)

Table 1-1. Summary of selected direct-write methods and advantages and disadvantages

summarizes these technologies.

1.3.1. Conductive Ink

The most mature of the direct-write technologies for electronics is conductive ink, first pioneered by the Lewis Lab in Harvard University. Conductive silver nanoparticles are suspended in a liquid to form an ink. The ink is deposited with an inkjet nozzle; the liquid is removed, either through evaporation or heating, and the nanoparticles form a conductive trace. To attain the best conductivity, the nanoparticles must be sintered to form a cohesive, conductive layer. This method allows for resolutions as low as 2 µm [1:6] and electrical conductivity as high as bulk metal upon sintering, or 10% of bulk metal with low temperature (75 °C) sintering [1:7].

This method works well, but reliable and repeatable inks can be hard to procure. Additionally, the great majority of ink formulations use silver micro and nanoparticles, and silver is not the ideal choice for all applications, e.g., it easily forms an oxide, reducing its electrical conductivity. Additionally, the need for sintering precludes the use of the ink on temperature-sensitive substrates, e.g. thermoplastics.

1.3.2. Laser-induced Forward Transfer

A less common direct-write method is laser-induced forward transfer (LIFT) [1:8]–[1:11]. A laser shines through a transparent ribbon, melting microdroplets from a film on the ribbon. These microdroplets are deposited on a substrate, where, as they solidify, they fuse together into a

conductive film. As with the conductive inks, substrate heating is a concern. Additionally, the ribbon must be replaced as the ink is used up. However, the resolution (>10 μm) [1:10] and electrical conductivity (5x bulk resistivity; 9 μΩ·cm) [1:9] are excellent.

1.3.3.Focused Ion Beam Induced Deposition (FIBID)

To produce nanoscale structures, a gas, consisting of a metal bonded to an organic group, can be flowed over a substrate. A laser [1:12] or focused ion beam [1:13] selectively rasters a pattern across the substrate; when the beam hits the gas, the gas dissociates into a metal, which is adsorbed, and an organic byproduct, which is not. The remaining gas and precursor are removed, and a pattern, with features less than 10 nm in length, are possible. This is the most expensive and highest resolution direct-write method reported in the literature, used for high-value circuit reworking [1:14], [1:15].

1.4. Applications

1.4.1.Flexible Electronics

While most microelectronics are produced on rigid substrates, such as silicon wafers or printed circuit boards, there is demand for flexible electronics—electronics directly printed on flexible substrates, such as paper or fabric. These electronics, generally centered around a sensor, can move with the flexible substrate. This allows for the collection of data without the need to carry around a small, rigid chip [1:16]-[1:19]. This is useful for medical devices and other cases in which wearable electronics are helpful. Typically, conductive inks are used to print the sensors [1:20], but more exotic methods have also been studied [1:21]

1.4.2.Integrated 3-D Printers

Additive manufacturing can produce structural materials well, but the integration of electronic components to additively manufactured components would open exciting possibilities. If a single printer, using one printhead to print plastic and another to add conductive traces or entire sensors or electronic components, could produce fully functional, inexpensive prototypes, additive manufacturing would be far more useful than it is now. This requires the ability to print on non-planar surfaces, on rough surfaces (like FDM/FFF-deposited plastics), and on temperature sensitive surfaces (such as plastics). Since traditional methods of depositing conductive traces involve planar surfaces, cleanrooms, and elevated substrate temperatures, an alternative is necessary. The first attempts at integration took place recently [1:23]. They have generally used conductive inks or pastes, leveraging existing printing technology, and adding conductive nanoparticles to greatly increase electrical conductivity.

1.4.3.Circuit Repair

Direct-write printing is also useful for the repair of circuits, whether old circuits that have been damaged or prototype circuits that must be modified to correct a design error. Focused-ion beam induced deposition has been used for this with excellent resolution, but it requires expensive facilities [1:24], [1:25]. Other metal deposition methods, including conductive ink and directed energy deposition, have been occasionally tried, despite the high temperatures necessary [1:26].

1.5. Sputtering

1.5.1. Plasma Physics

A plasma is a fluid in which electrical forces dominate. The ions and electrons are separated, while an electric field (usually a combination of an externally applied one and the internal one from charge separation) drives the movement of the charged species. Because charged species naturally leave the plasma or recombine into neutral atoms, there must be a source of electrons and/or ions. In a sputtering plasma, this source is electron impact ionization—when an electron strikes an atom with sufficient energy, the atom can be ionized, separating into a positive ion and an electron. This is the primary source of ions in a sputtering plasma. In a stable plasma, the rate of ion (or electron) production is matched to the rate of ion (or electron) loss through recombination, diffusion, and convection.

To determine the energy of charged particles in a dense plasma (and thus the results of electron impact), it is helpful to consider the reduced electric field, which is defined as the electric field divided by the pressure. This is directly proportional (for a given plasma species) to the average energy imparted by the electric field to a charged particle, in the distance between two subsequent collisions. Collisions thermalize the energized charged particles, robbing them of the energy and momentum that the electric field imparted to them. Thus, the reduced electric field is a measure of how much energy the electric field imparts to charged particles. Because of this, the average energy of charged species is often given as a function of the reduced electric field.

A direct current (DC) glow discharge, or a plasma with relatively low current (such as the plasmas used for sputtering), is struck between an anode and a cathode. Close to the cathode, there is an excess of positive charge and a very strong electric field is directed towards the cathode. This area is known as the cathode fall. Most ionization occurs in this region. The plasma has other regions, which are less significant for the fundamental processes discussed in this thesis.

1.5.2. Traditional Sputtering

Sputtering is a manufacturing process that uses high-energy ions to transfer atoms from a target to a nearby substrate. A plasma is formed, and the electric field forces the positive ions towards the cathode. The ions strike the cathode with a tremendous energy, breaking the bonds of a single (or multiple) atom of the cathode (also called the target). This atom travels to the substrate, where it adsorbs onto the surface [1:27].

Traditionally, sputtering is done in vacuum (~1 mTorr) [1:28]. This allows the sputtered particles and ions to travel ballistically; most particles do not collide from the moment of sputtering or ionization (depending on the particle type) to the moment when they reach a surface.

1.6. Microsputtering

1.6.1. Paschen's Law

As previously described when discussing the reduced electric field, the higher the collisionality of the plasma, the higher the necessary electric field to energize electrons

sufficiently. This can also be expressed by Paschen's law [1:29]. Paschen discovered that the breakdown voltage of a plasma, i.e., the voltage necessary to energize electrons sufficiently to transform an un-ionized gas into a plasma, is a function of the product of the interelectrode distance and the pressure, for a given gas and temperature (Figure 1-1). Since the interelectrode distance is inversely proportional to the electric field (for a given voltage), and the pressure is inversely proportional to the density (in an ideal gas at a given temperature), the product of the interelectrode distance and the pressure is inversely proportional to the reduced electric field. Thus, the reduced electric field, as shown above, is crucial to understanding the behavior of the plasma.

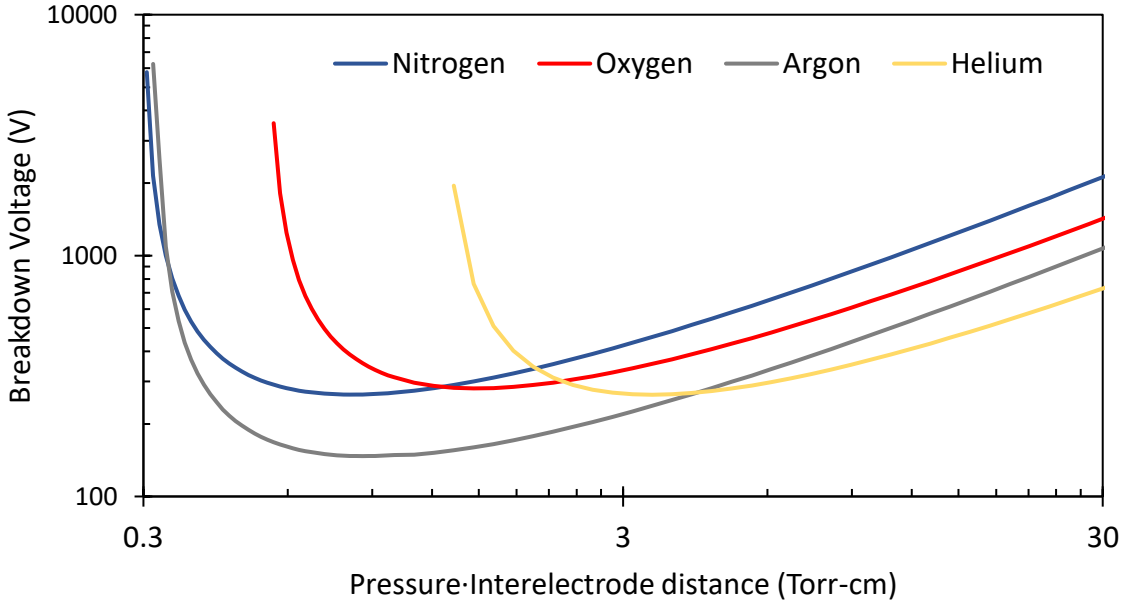

Figure 1-1. Breakdown voltage for selected gases as a function of the product of the pressure and interelectrode distance. On the left of the curve, breakdown does not occur to the rarity of collisions; on the right, collisions are too frequent for the electrons to build up the necessary energy between collisions. Calculated based on data from [1:27].

Other plasma behaviors, such as plasma stability, also depend on the product of the interelectrode distance and pressure. For our purposes, that means that even though plasmas are traditionally maintained in vacuum, we can maintain a similar plasma at atmospheric pressure, provided the interelectrode distance is small enough. The point of greatest stability is at several Torr · cm (several Pa · m). Thus, at atmospheric pressure, an interelectrode distance of ~10 μm would be ideal; we use distances of approximately 1 mm due to manufacturing constraints.

Microplasmas have been used for a variety of modern measurements, primarily chemical. Much work was done in the first decade of this century; several significant review papers are referenced [1:30]–[1:34].

Group	Advances	Deficiencies
Burwell (Case Western)	First direct-write sputtering	No process parameter discussion, heated substrate, no material quality discussion
Abdul	High resolution, first device	Substrate heated/used as anode
Wang	Investigated material quality	Powdered Copper, low conductivity
Zhao	Hydrogen to prevent copper oxidation; RF plasma	Substrate heating, no printhead movement
Guo	Effects of process parameters on nanoparticles	No investigation of other material qualities
Ussenov	Investigation of plasma	Little investigation of deposits

Table 1-2. Summary of other investigations into atmospheric-pressure microplasmas for the purpose of direct-write microsputtering. While all these advances are useful, there is still much work to be done, particular in investigating and improving the material qualities.

1.6.2. Other Work

While this thesis comprises the most thorough investigation of microplasma sputtering, it is not the only study of microsputtering. Microsputtering promises to combine the flexibility of additive manufacturing (e.g., direct-write, atmospheric pressure) with the material quality of sputtering (e.g., atom-by-atom deposition, pure materials). While microsputtering was first seen at the end of the last century [1:35], the first study to harness the direct-write capabilities of microsputtering was done in Case Western Reserve University in 2015 [1:36]. Researchers struck a plasma between two electrodes, sputtering a thin gold wire 75 μm in diameter. An argon gas flow carried the sputtered material to a substrate 5 mm away. Magnets were used to rotate the plasma and thus prevent target overheating.

Additional research occurred in the University of British Columbia. Researchers used the substrate itself as the anode of the sputtering plasma, relying on careful positioning to maintain a 10-20 μm gap between the target, a micromachined copper tip, and the substrate[1:37]. This research yielded a thermocouple; a copper trace was deposited with traditional methods (electron beam evaporation) and Constantan was microsputtered on top [1:38]. The use of the substrate as the anode, while efficient, requires the use of a durable substrate that can withstand the plasma.

Wang et al. sputtered copper with an argon plasma; however, they used powdered copper, instead of a wire electrode. While the use of powder increases throughput, it adds a step (procuring the powdered copper) [1:39]. Zhao et al. evaporate the metal with a plasma, instead of sputtering it, leading to larger grain size [1:40]. There has been little research into the effect of process parameters; however, one notable study by Guo et al. explored the effect of hydrogen on the oxidation of evaporated copper [1:41]. Ussenov et al. explored the chemical composition of the plasma and sputtered films [1:42]

Because atmospheric plasmas do not necessarily heat the substrate, they have been used to sputter metal for antimicrobial coatings for temperature-sensitive plastics [1:43]. However, these coatings do not need to form patterns; rather, an entire medical device is coated [1:44].

There are several other methods that use plasmas to enhance material deposition, such as using the plasma to remove precursors and allow a suspended metal to remain, reduction of compounds, modification of substrates, and the processing of larger particles into nanoparticles [1:45]-[1:48]. However, none of these have the atom-by-atom deposition of microsputtering.

1.7. Structure

This thesis will first outline the hardware developed for our investigation (Chapter 2). It will then discuss the material qualities of the deposits, namely, the feature size (Chapter 3), adhesion (Chapter 4) and electrical conductivity (Chapter 5). Chapter 6 will discuss an important plasma property, the ion energy, and methods to increase that. The thesis will describe two demonstrations of microplasma sputtering, i.e., the coating of nanowires for RF connectors (Chapter 7) and a capacitor (Chapter 8). Chapter 9 will conclude this work with a discussion of the future of microplasma sputtering as a manufacturing tool.

1.8. References

[1:1] Stephens R. Observation of sputtering at atmospheric pressure. Journal of Analytical Atomic Spectrometry. 1988;3(8):1137-9.

[1:2] Reiser A, Koch L, Dunn KA, Matsuura T, Iwata F, Fogel O, Kotler Z, Zhou N, Charipar K, Piqué A, Rohner P. Metals by Micro-Scale Additive Manufacturing: Comparison of Microstructure and Mechanical Properties. Advanced Functional Materials. 2020 Jul;30(28):1910491.

[1:3] Behera D, Chizari S, Shaw LA, Porter M, Hensleigh R, Xu Z, Roy NK, Connolly LG, Zheng XR, Saha S, Hopkins JB. Current Challenges and Potential Directions Towards Precision Microscale Additive Manufacturing–Part II: Laser-Based Curing, Heating, and Trapping Processes. Precision Engineering. 2020 Dec 31(68):301-318.

[1:4] Chizari S, Shaw LA, Behera D, Roy NK, Zheng X, Panas RM, Hopkins JB, Chen SC, Cullinan MA. Current challenges and potential directions towards precision microscale additive manufacturing–Part III: Energy induced deposition and hybrid electrochemical processes. Precision Engineering. 2020 Dec 15(68):174-186.

[1:5] Saengchairat N, Tran T, Chua CK. A review: Additive manufacturing for active electronic components. Virtual and Physical Prototyping. 2017 Jan 2;12(1):31-46.

[1:6] Ahn BY, Duoss EB, Motala MJ, Guo X, Park SI, Xiong Y, Yoon J, Nuzzo RG, Rogers JA, Lewis JA. Omnidirectional printing of flexible, stretchable, and spanning silver microelectrodes. Science. 2009 Mar 20;323(5921):1590-3.

[1:7] Walker SB, Lewis JA. Reactive silver inks for patterning high-conductivity features at mild temperatures. Journal of the American Chemical Society. 2012 Jan 25;134(3):1419-21.

[1:8] Willis DA, Grosu V. Microdroplet deposition by laser-induced forward transfer. Applied Physics Letters. 2005 Jun 13;86(24):244103.
[1:9] Adrian FJ, Bohandy J, Kim BF, Jette AN, Thompson P. A study of the mechanism of metal deposition by the laser-induced forward transfer process. Journal of Vacuum Science & Technology B: Microelectronics Processing and Phenomena. 1987 Sep;5(5):1490-4.
[1:10] Rapp L, Ailuno J, Alloncle AP, Delaporte P. Pulsed-laser printing of silver nanoparticles ink: control of morphological properties. Optics express. 2011 Oct 24;19(22):21563-74.
[1:11] Serra P, Piqué A. Laser-induced forward transfer: Fundamentals and applications. Advanced Materials Technologies. 2019 Jan;4(1):1800099.
[1:12] Kochemirovsky VA, Skripkin MY, Tveryanovich YS, Mereshchenko AS, Gorbunov AO, Panov MS, Tumkin IY, Safonov SV. Laser-induced copper deposition from aqueous and aqueous–organic solutions: State of the art and prospects of research. Russian Chemical Reviews. 2015;84(10):1059.
[1:13] Della Ratta AD, Melngailis J, Thompson CV. Focused-ion beam induced deposition of copper. Journal of Vacuum Science & Technology B: Microelectronics and Nanometer Structures Processing, Measurement, and Phenomena. 1993 Nov;11(6):2195-9.
[1:14] Shedd GM, Lezec H, Dubner AD, Melngailis J. Focused ion beam induced deposition of gold. Applied physics letters. 1986 Dec 8;49(23):1584-6.
[1:15] Stewart DK, Stern LA, Morgan JC. Focused-ion-beam induced deposition of metal for microcircuit modification. In Electron-Beam, X-Ray, and Ion-Beam Technology: Submicrometer Lithographies VIII 1989 Aug 1 (Vol. 1089, pp. 18-25). International Society for Optics and Photonics.
[1:16] Wong WS, Salleo A, editors. Flexible electronics: materials and applications. Springer Science & Business Media; 2009 Apr 9.
[1:17] Gates BD. Flexible electronics. Science. 2009 Mar 20;323(5921):1566-7.
[1:18] Yang Y, Gao W. Wearable and flexible electronics for continuous molecular monitoring. Chemical Society Reviews. 2019;48(6):1465-91.
[1:19] Gao W, Ota H, Kiriya D, Takei K, Javey A. Flexible electronics toward wearable sensing. Accounts of Chemical Research. 2019 Feb 15;52(3):523-33.
[1:20] Russo A, Ahn BY, Adams JJ, Duoss EB, Bernhard JT, Lewis JA. Pen-on-paper flexible electronics. Advanced Materials. 2011 Aug 9;23(30):3426-30.
[1:21] Sun Y, Rogers JA. Inorganic semiconductors for flexible electronics. Advanced Materials. 2007 Aug 3;19(15):1897-916.
[1:22] Li J, Wasley T, Nguyen TT, Ta VD, Shephard JD, Stringer J, Smith P, Esenturk E, Connaughton C, Kay R. Hybrid additive manufacturing of 3D electronic systems. Journal of Micromechanics and Microengineering. 2016 Aug 23;26(10):105005.
[1:23] Han D, Lee H. Recent advances in multi-material additive manufacturing: methods and applications. Current Opinion in Chemical Engineering. 2020 Jun 1;28:158-66.

[1:24] Matsui S, Kaito T, Fujita JI, Komuro M, Kanda K, Haruyama Y. Three-dimensional nanostructure fabrication by focused-ion-beam chemical vapor deposition. Journal of Vacuum Science & Technology B: Microelectronics and Nanometer Structures Processing, Measurement, and Phenomena. 2000 Nov;18(6):3181-4.
[1:25] Harriott LR, Wagner A, Fritz F. Integrated circuit repair using focused ion beam milling. Journal of Vacuum Science & Technology B: Microelectronics Processing and Phenomena. 1986 Jan;4(1):181-4.
[1:26] Saboori A, Aversa A, Marchese G, Biamino S, Lombardi M, Fino P. Application of directed energy deposition-based additive manufacturing in repair. Applied Sciences. 2019 Jan;9(16):3316.
[1:27] Lieberman MA, Lichtenberg AJ. Principles of plasma discharges and materials processing. John Wiley & Sons; 2005 Apr 8.
[1:28] Wasa K, Hayakawa S. Handbook of sputter deposition technology. Elsevier; 2012.
[1:29] Paschen F, Ueber die zum Funkenübergang in Luft, Wasserstoff und Kohlensäure bei verschiedenen Drucken erforderliche Potentialdifferenz, Annalen der Physik 1889; 273(5):69-96.
[1:30] Karanassios V. Microplasmas for chemical analysis: analytical tools or research toys?. Spectrochimica Acta Part B: Atomic Spectroscopy. 2004 Jul 30;59(7):909-28.
[1:31] Tendero C, Tixier C, Tristant P, Desmaison J, Leprince P. Atmospheric pressure plasmas: A review. Spectrochimica Acta Part B: Atomic Spectroscopy. 2006 Jan 1;61(1):2-30.
[1:32] Becker KH, Schoenbach KH, Eden JG. Microplasmas and applications. Journal of Physics D: Applied Physics. 2006 Jan 20;39(3):R55.
[1:33] Kogelschatz U. Applications of microplasmas and microreactor technology. Contributions to Plasma Physics. 2007 Feb;47(1-2):80-8.
[1:34] Foest R, Schmidt M, Becker K. Microplasmas, an emerging field of low-temperature plasma science and technology. International Journal of Mass Spectrometry. 2006 Feb 15;248(3):87-102.
[1:35] Barborini E, Piseri P, Milani P. A pulsed microplasma source of high intensity supersonic carbon cluster beams. Journal of Physics D: Applied Physics. 1999 Nov 7;32(21):L105.
[1:36] Burwell IV ED. A microplasma-based sputtering system for direct-write, microscale fabrication of thin-film metal structures. 2015. (Masters dissertation, Case Western Reserve University).
[1:37] Abdul-Wahed AM, Roy AL, Xiao Z, Takahata K. Direct writing of metal film via sputtering of micromachined electrodes. Journal of Materials Processing Technology. 2018 Dec 1;262:403-10.
[1:38] Abdul-Wahed AM, Roy AL, Takahata K. Microplasma drawing of thermocouple sensors. In 2016 IEEE SENSORS 2016 (pp. 1-3). IEEE.

[1:39] Wang T, Lv L, Shi L, Tong B, Zhang X, Zhang G, Liu J. Microplasma direct writing of a copper thin film in the atmospheric condition with a novel copper powder electrode. Plasma Processes and Polymers. 2020 Aug;17(8):2000034.

[1:40] Zhao P, Zheng W, Meng YD, Nagatsu M. Characteristics of high-purity Cu thin films deposited on polyimide by radio-frequency Ar/H2 atmospheric-pressure plasma jet. Journal of Applied Physics. 2013 Mar 28;113(12):123301.

[1:41] Guo QJ, Ni GH, Li L, Lin QF, Zhao YJ, Sui SY, Xie HB, Duan WX, Meng YD. Effects of input power, gas flow rate and hydrogen concentration on Cu film deposition by a radio frequency driven non-thermal atmospheric pressure plasma jet. Thin Solid Films. 2018 Aug 30;660:493-8.

[1:42] Ussenov YA, Toktamyssova MT, Dosbolayev MK, Gabdullin MT, Daniyarov TT, Ramazanov TS. Thin-film deposition by combining plasma jet with spark discharge source at atmospheric pressure. Contributions to Plasma Physics. 2021 Mar;61(3):e202000140.

[1:43] Kredl J, Kolb JF, Schnabel U, Polak M, Weltmann KD, Fricke K. Deposition of antimicrobial copper-rich coatings on polymers by atmospheric pressure jet plasmas. Materials. 2016 Apr;9(4):274.

[1:44] Chung M, Chu CC. Catheter inner surface metal coating by sputtering with microplasma. In 2008 IEEE 35th International Conference on Plasma Science 2008 Jun 15 (pp. 1-1). IEEE.

[1:45] Mariotti D, Sankaran RM. Microplasmas for nanomaterials synthesis. Journal of Physics D: Applied Physics. 2010 Jul 29;43(32):323001.

[1:46] Sawada Y, Tamaru H, Kogoma M, Kawase M, Hashimoto K. The reduction of copper oxide thin films with hydrogen plasma generated by an atmospheric-pressure glow discharge. Journal of Physics D: Applied Physics. 1996 Oct 14;29(10):2539.

[1:47] Sui Y, Zorman CA, Sankaran RM. Plasmas for additive manufacturing. Plasma Processes and Polymers. 2020 May;17(5):2000009.

[1:48] Tan JH, Sing SL, Yeong WY. Microstructure modelling for metallic additive manufacturing: A review. Virtual and Physical Prototyping. 2020 Jan 2;15(1):87-105.

Chapter 2 – **Microsputtering System**

2.1. Introduction

This chapter describes the various versions of the printhead and printing setup developed for this thesis. Over the course of the five-year research program, the setup was upgraded and modified numerous times; ranges of parameters are given for cases in which a given parameter changed over time, rather than an exhaustive enumeration of the historical versions of the printer. Where the exact setup used is significant for a set of results, a note will be made in the following chapters.

The microsputterer harnesses and accounts for plasma effects, fluid effects, and electrostatic effects. An overview can be seen in Figure 2-2. This chapter will outline the subsystems of the printer: the sputtering plasma, the wire feed, the gas system, the electrical system, the substrate, the mobility system, and the nozzle. Where applicable, a note will be added if a subsystem is discussed in greater detail later in the thesis.

2.2. Sputtering Plasma

The heart of the system is the sputtering plasma. It consists of a grounded target wire (the plasma cathode) and a charged anode, with a gap between them (the electrode-target gap). This gap is typically approximately 1 mm in size. Voltage is supplied to the anode by a Keithley 2657A power supply, which is current-controlled. Typical currents are 1-5 mA; the higher end of this range was used for larger diameter wires, generally in the last two years of the research program. Higher currents increase the deposition rate, but can overheat and melt the target wire. A ballast resistor, typically 200-500 kΩ, is placed between the power supply and anode to stabilize the plasma and prevent rapid fluctuations in plasma behavior due to parasitic capacitance. The power supply can operate at a maximum voltage of 3 kV; while this high voltage was necessary to strike the plasma, the plasma was typically operated with a plasma voltage (i.e., excluding the voltage drop across the ballast resistor) of 500-1500 V. The dependence of the printer's operation on the energy of the charged species, and thus on the plasma voltage, is discussed in Chapter 6. Briefly, higher voltage increases the ion energy, but also can cause the wire to melt.

2.3. Wire Feed

Originally, the target wire was 50 µm diameter gold (99.99% purity, Sigma Aldrich), but was replaced with a 100 µm diameter wire (99.95% purity, Alfa Aesar) three years into the research program to enable greater heat dissipation and thus allow higher current without melting the wire. Aluminum wire, 127 µm in diameter (99.999 purity, Alfa Aesar) was used for the production and deposition of alumina (Chapter 6).

As the wire is sputtered, it is depleted. To prevent this depletion from negatively impacting the operation of the printer, we introduce a wire feed system. The target wire is fed by a capstan-roller system (Figure 2-3); the wire is pinched between a rubber roller and a metal capstan; a knob, either manually controlled or electronically driven, drives the rubber roller and forces the wire up and down a glass tube (referred to in this thesis as the inner capillary tube, with an outer diameter of 1-1.5 mm and an inner diameter of 0.5-1.1 mm). The wire exits the tube after 8 cm, and typically

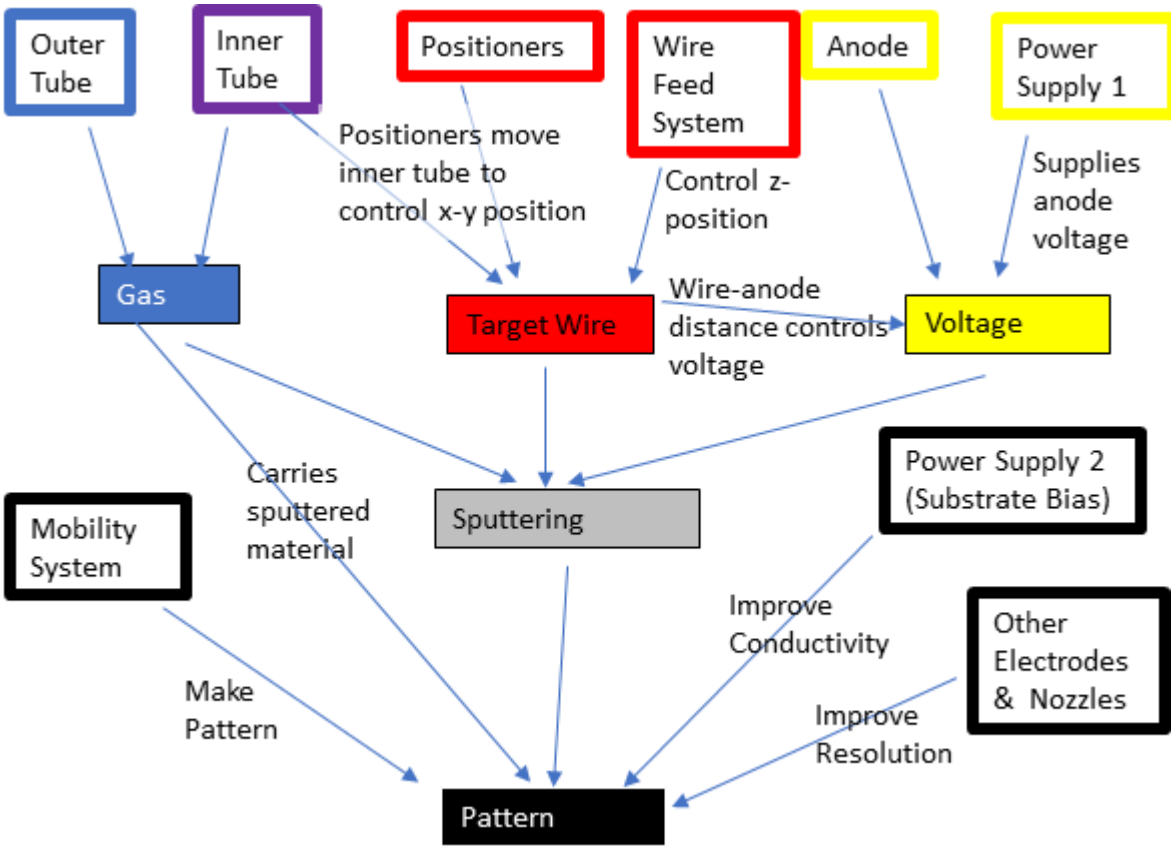

Figure 2-1. A conceptual schematic of the various systems needed for microsputtering. Effective sputtering requires control of the gas surrounding the target wire, a strong electric field, and a target wire. To transform sputtered atoms into a direct-write mechanism, other systems, in black, are needed.

protrudes from the tube approximately 1 mm. This protrusion allows the plasma to reach it directly (rather than climbing up the inner glass tube), prevents it from melting to the inner tube, yet is close enough to the mouth of the tube to allow the gas flow to surround it.

While the initial design could accomodate a single wire, most electronic components need multiple materials. Consequently, in the third year of the project, a multimaterial wire feed was introduced. This system consists of three rollers: a central one that can be turned through a knob, and two side rollers, connected to a second knob, referred to in this thesis as the *wire selector*, and are electrically grounded. Each of the two wires is fed between the central roller and one of the two side rollers; by rotating the wire selector, the side rollers can be moved so that a given wire is pinched between its side roller and the central roller. Once the wire is pinched, rotating the central roller will extend or retract that wire; that wire is also electrically grounded through the side roller that is now in contact with it (Figure 2-2). Once both wires are fed through the inner capillary tube, the plasma can be switched from one wire to the other by retracting the active wire 3 mm, rotating the wire selector to pinch the other wire, and extending the newly pinched

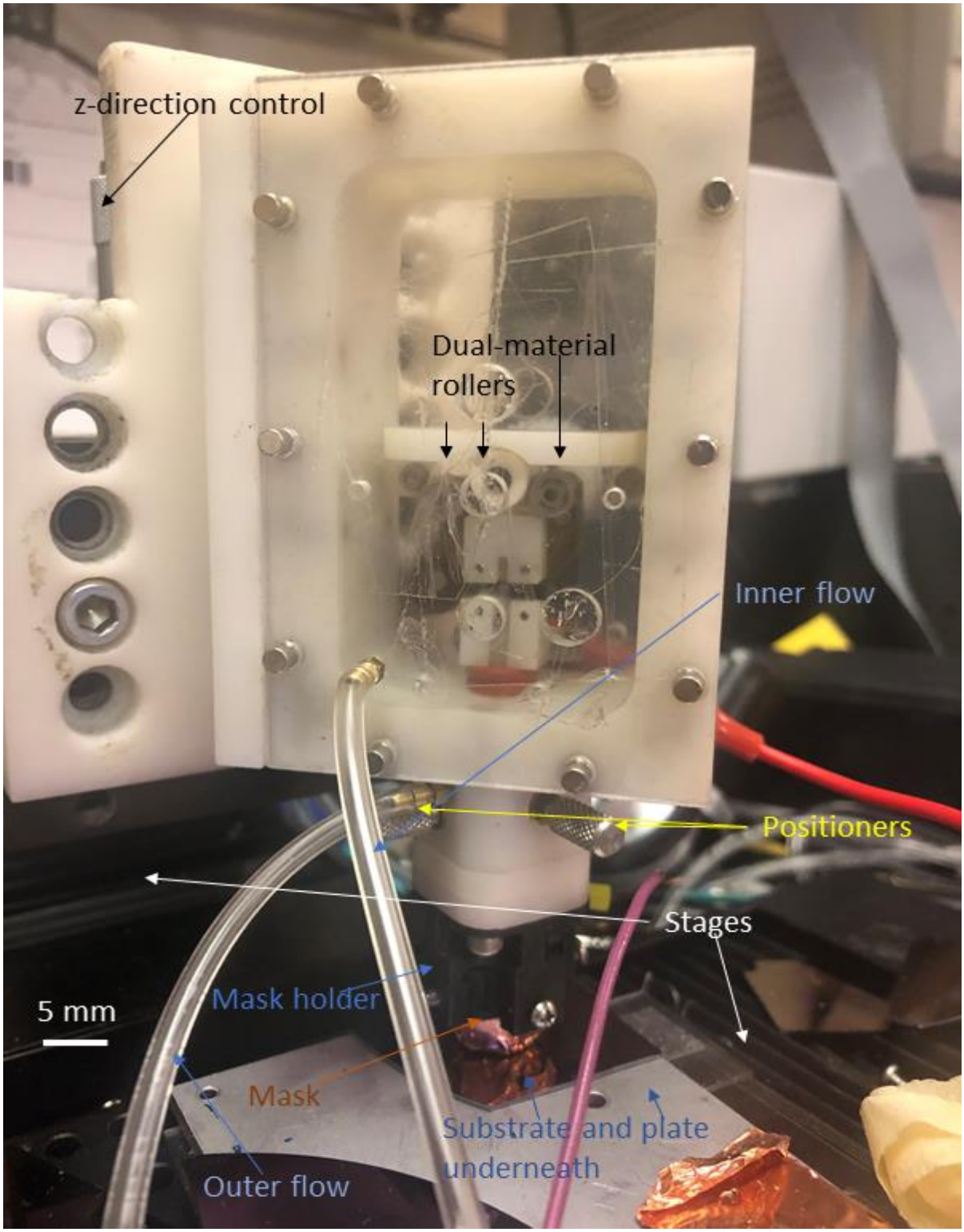

Figure 2-2. A photograph of the entire microsputtering system described in this chapter. The electrodes and target wire are covered by the nozzle and nozzle holder.

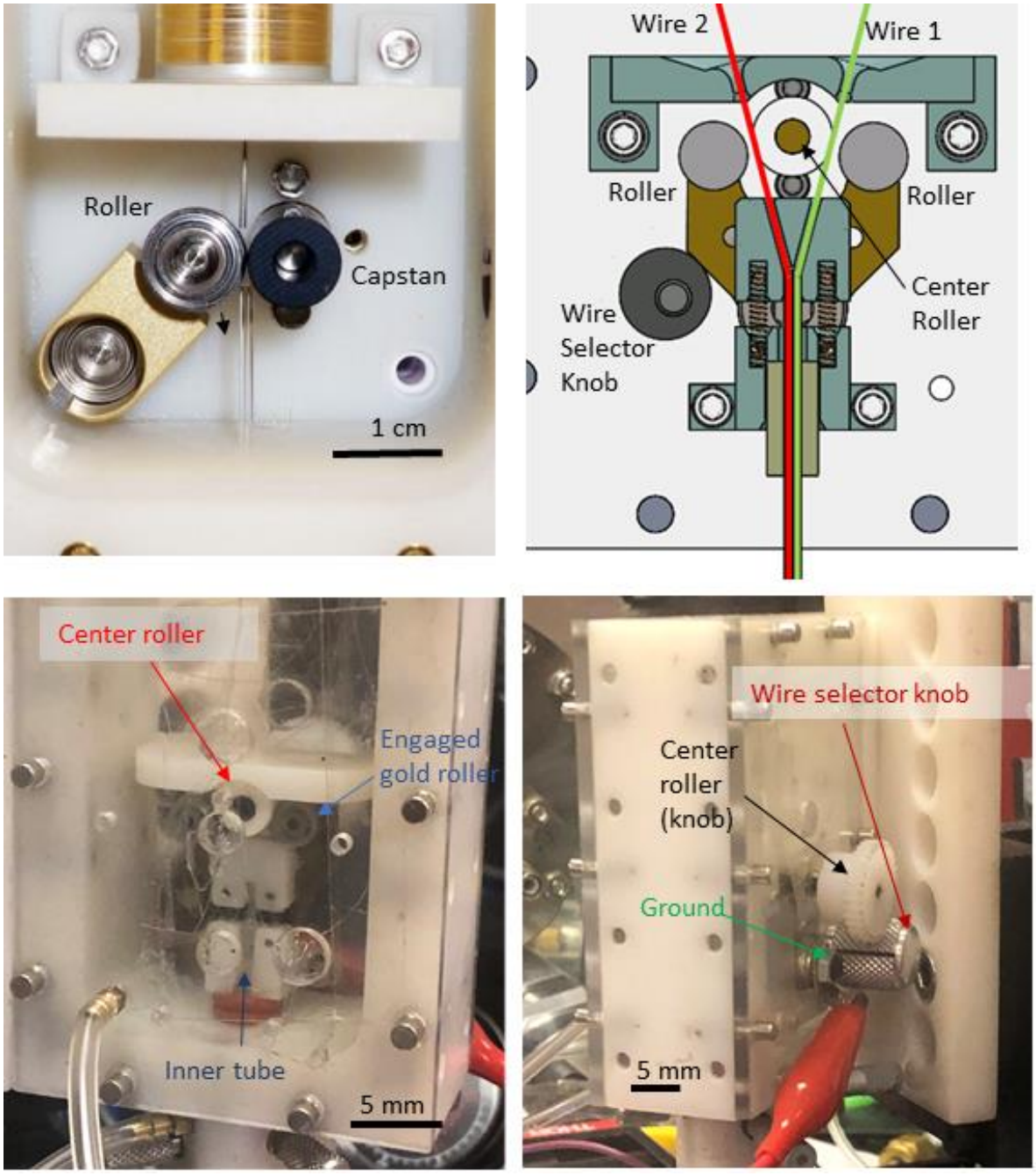

Figure 2-3. The wire feed system, both for the single feed (top left) and dual-feed (remainder) systems. A schematic of the dual-feed system is shown in the top right. In the current configuration (bottom row), the gold wire, on the right side (bottom right), is engaged with the central roller of the dual-feed system. That can be changed by turning the selector knob (bottom right image). The alligator clip for grounding the target wire is visible in the right image.

wire. Doing so will momentarily extinguish the plasma, as for a short time, both wires will be retracted, but the new wire can be sputtered without disassembling the head or even moving it. The multimaterial head will be used in Chapter 8.

The exact position of the inner capillary tube was found to greatly influence the behavior of the plasma. Most simply, a larger target-electrode distance resulted in a greater plasma voltage. Additionally, the placement of the inner capillary tube has a strong impact on the finely-tuned electrostatic focusing mechanisms that were implemented [2:1]. To control and vary the placement of the inner capillary tube, a system of four positioners was installed; two positioners, separated 90 degrees from each other are spring-loaded and, when armed, will expand until they reach a stronger force; the other two have vernier controls and can position the inner capillary tube in the x and y directions with 200 µm precision (Figure 2-4).

2.4. Gas Flow

This inner capillary tube, in addition to controlling the position of the target wire, is part of the gas delivery system. Two independent streams of gas flow through the printer. One, the *inner gas flow*, flows through the wire chamber and then through the inner gas tube. The second, the *outer gas flow*, flows through a nozzle and then through a larger glass tube that surrounds the inner capillary tube; this has an outer diameter of 5 mm and an inner diameter of 3 mm. In later experiments, it was found that a tube with an inner diameter of 2 mm improves the resolution These two concentric flows can be controlled independently to shape the fluid velocity field for ideal transport. They can also supply different gases, such as argon and air, and cool the target wire via convection. The tubes, along with the positioning controls, can be seen in Figure 2-3.

The gas flow can be controlled via a mass flow controller (MFC) (for low flows, <500 sccm), pressure valves (1-15 psi, >10 slm), or, for the intermediate regime, pressure valves connected to a long (25 or 50 ft) narrow plastic tube (1/16" inner diameter). The flow through this long, narrow tube is sufficiently slowed that a pressure valve can be used for fine control of the flow in this intermediate regime. Specifically, the Darcy-Weisbach equation show that Q, the volumetric flow rate, can, in the laminar regime, be found by

$$Q = \frac{\pi D_c^4 \Delta P}{128 L \mu} \tag{2-1}$$

where D_c is the tube diameter, ΔP the pressure drop over the tube, L the length of the tube, and µ the viscosity. For air in our given parameters, $\frac{Q}{\Delta P}$ is 0.467 slm/psi (0.067 slm/kPa) for the 25 ft tube; due to other head loss in the fluid system, the experimental value is approximately 75% of that (0.35 slm/psi). With a pressure regulator with 0.5 psi precision, we can reach nearly the entire range of desired flow; a longer tube (50 ft) is used to inexpensively enable access to the rest of the regime.

Air is supplied by the building's supply of compressed dry air, while a tank of argon (20-40 cf, 99.99% pure, Airgas) stores the argon necessary for the system's operation. The two gases can also be mixed through a T-junction of the Tygon tubes. The mixture will be discussed in Chapter 6.

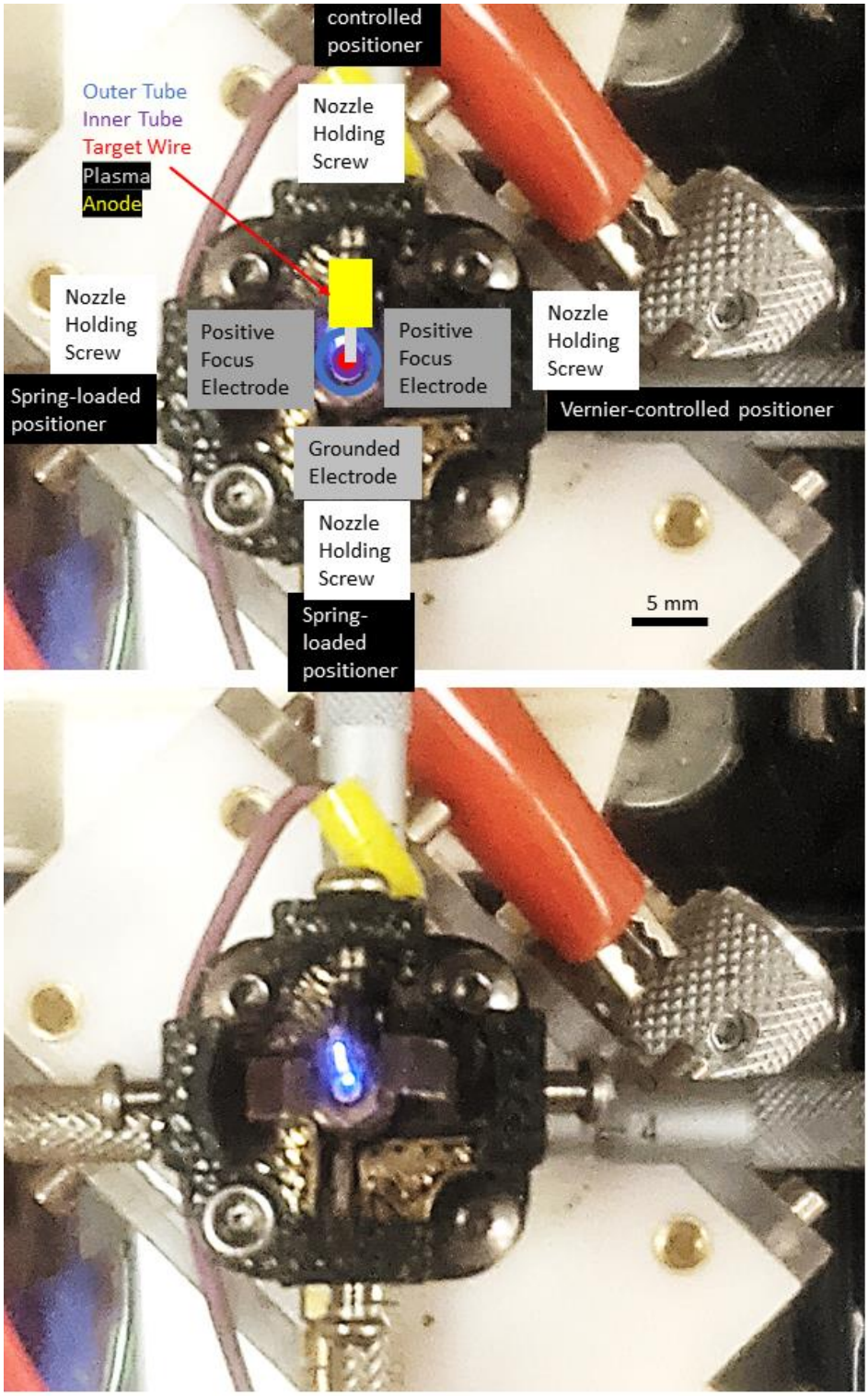

Figure 2-4. A view of the bottom of the microsputterer, with annotated (top) and unannotated (bottom) photographs. The two tubes, inner tube positioner, lit plasma, and electrodes, are all visible.

2.5. Electrical

Numerous electrical features are positioned around the printhead. The plasma near the target is positively charged; by directing the positively charged plasma, the sputtered material can also be manipulated, through the principle of ion flux [1], [2]. This phenomenon is crucial to the feature resolution (Chapter 3), and highly relevant for the studies into the electrical conductivity (Chapter 5). These include a substrate bias and focusing electrodes.

In the second year of the program, as a result of the findings in Chapter 5 that electric fields improve the electrical conductivity, a negative bias voltage (approximately -300 V) was placed under the substrate, using a HP 6516A power supply. The bias voltage attracts the positively charged plasma and sputtered material towards the substrate. Our initial arrangement, used for the experiments of Chapter 5, used a negatively charged plate underneath the substrate, with the substrate electrically isolated from that plate [2:3]. Later experiments, beginning in the third year of the project (Chapters 4, 6-8), connected the substrate directly with the negative power supply in order to minimize the effect of charge buildup on the substrate. To prevent a plasma from being struck between the electrodes and substrate, 0.5-1 MΩ of resistance was introduced between the

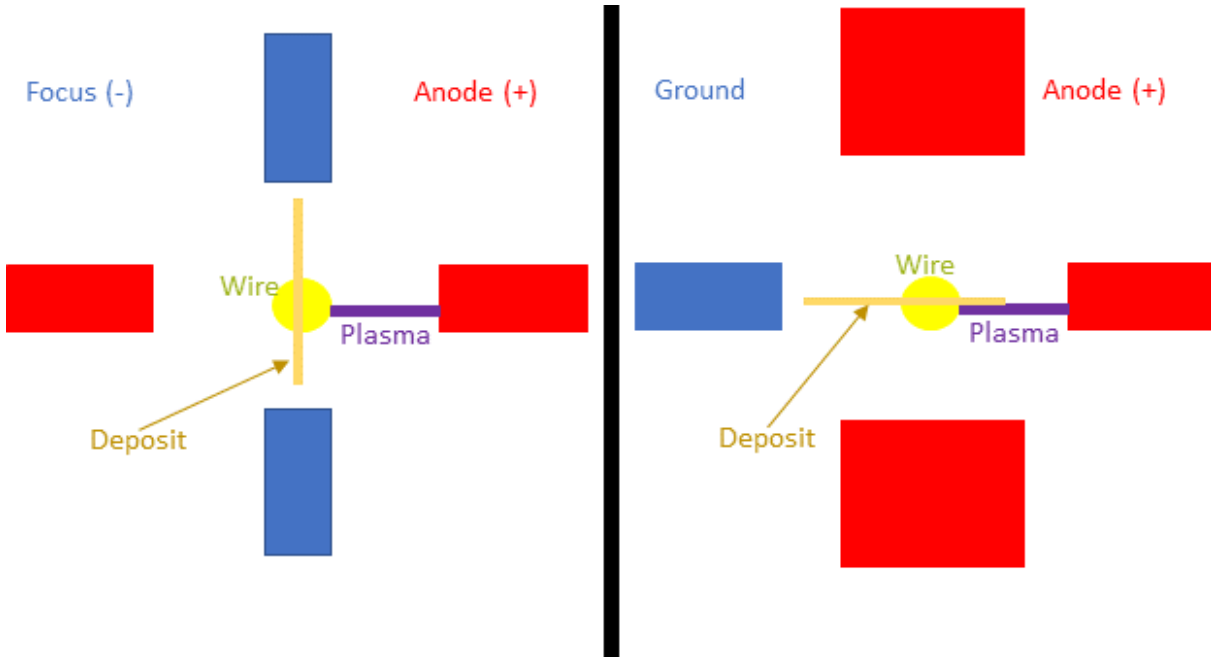

Figure 2-5. Original (left) and updated (right) electrode configurations. In the left configuration, the deposit is perpendicular to the plasma, attracted by the negatively biased focus electrodes (in blue) and repelled by the positively charged electrodes (in red). However, once the substrate is negatively charged, the electrodes must be rearranged so that the deposit is parallel to the plasma, since the plasma carries sputtered material to the charged substrate. Three positively biased electrodes (in red) repel the sputtered material, which is drawn to a grounded plasma (in blue). The positively biased electrodes on the side are wider, to further shape the electric fields so that the field lines are parallel to the desired direction of the printed line as much as possible.

substrate and the negative power supply. The voltage drop across this resistance is monitored in order to measure the current that reaches the substrate; the current is typically in the range of 100 nA-50 µA.

An electrostatic focusing mechanism consisting of the plasma's anode and another 3 electrodes, spaced equidistant (2 mm) from the center of the printhead and 90 degrees from each other. In the first configuration, all electrodes are 0.5 mm wide. The anode and electrode opposite the anode were positively biased, while the two electrodes 90 degrees from those two (referred to as the *focus electrode*) were negatively biased. The positive electrodes were designed to repel the positively charged sputter flux, while the negative electrodes attracted them, shaping the sputter flux into a long, narrow line running from negative electrode to negative electrode (Figure 2-5). Details of this arrangement and its efficacy are given in [2:1],[2:2].

However, the introduction of the previously mentioned negatively charged substrate (as described in Chapter 5) modifies the transport phenomena of our sputterer. Specifically, the negatively charged substrate pulls the highly charged positive region of the plasma towards the substrate. This region stretches from the anode to the target wire, along the axis that had previously been minimized to improve the resolution. As such, it became necessary to modify the electrostatic focusing system. Three electrodes, namely the anode and the two electrodes 90 degrees away, were all positively biased; the fourth electrode, opposite the anode, was grounded, with an aim that the plasma, repelled from the other three electrodes, would be drawn towards the grounded electrode and focused into a long, narrow line. The two *focus electrodes* that are 90 degrees from the anode were also made wider (3 mm), to improve the uniformity of the electric fields, and separated from the power supply with a 1 MΩ resistor, to ensure that the plasma is struck between the target and the anode, not the target and the focus electrodes (Figure 2-5).

2.6. Mobility System

The printhead is positioned 1-5 mm above the substrate. In its original form, the system is movable along all three axes; the X and Y axes are controlled each by a Thorlabs NRT100; one moves the printhead along one axis while the other moves the substrate along the other (Figure 2-6). This allows 80 mm of movement in each direction, with computer-controlled motion at speeds ranging from 50 µm/s to 5 mm/s and precision of 10 µm. The Z axis is controlled by a manual vernier-controlled stage, with 500 mil (12.7 mm) of range and 1 mil (25 µm) of precision. An improved stage, at use at MIT Lincoln Laboratory, uses a Meca500 robotic arm (Mecademic), with 6 joints, 5 µm precision, and computer-controlled motion [2:4] (Figure 2-6).

2.7. Nozzle

As described in Chapter 3, a nozzle is necessary for the definition of fine features. Although the printer does not heat the substrate significantly, the nozzle, closer to the plasma, does heat to approximately to 80 °C. To prevent damage to the nozzle, ULTEM 1010, a polymer designed to withstand up to 209 °C, is used [2:5]. However, the manufacturing resolution of ULTEM 1010, 1 mm, is too large for our purposes; instead FunToDo Industrial Blend, a high-temperature-compatible (225 °C) resin with better (~75 µm) resolution is chosen [2:6],[2:7]. However, even at such low temperatures, the FunToDo resin outgases slightly; although the nozzle is not damaged,

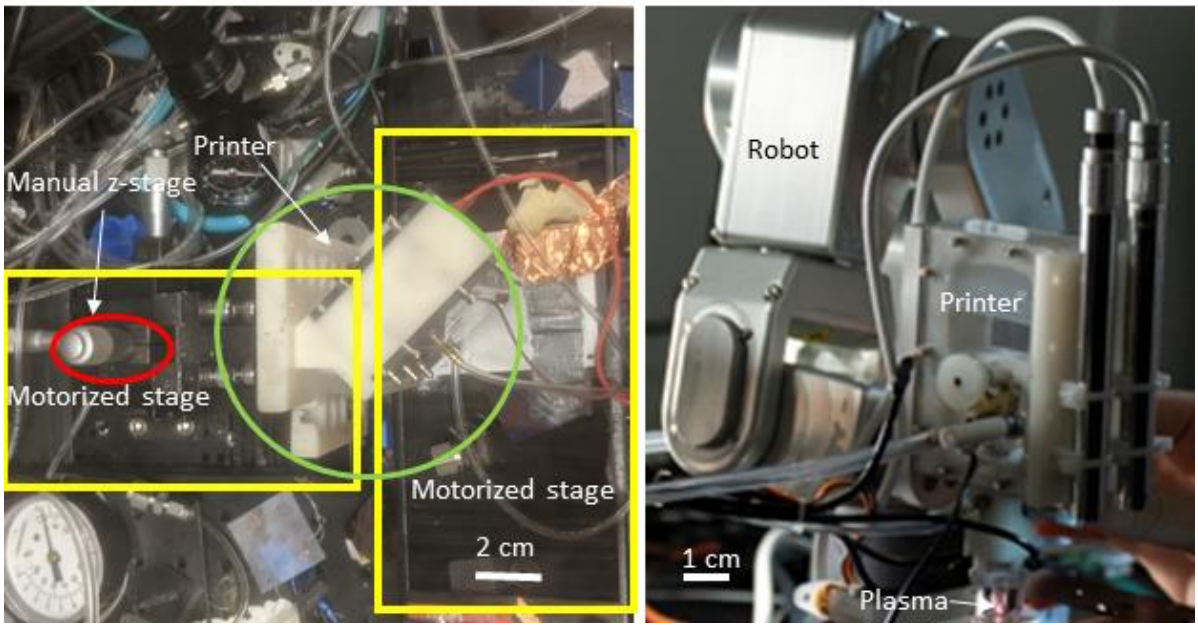

Figure 2-6. The NRT motorized stage (left), installed at MIT, and the Mechademic robot (right), installed at MIT Lincoln Laboratory. The motorized stages are outlined in yellow, while the printer is circled in green and the z-stage is circled in red in the left image .Note that the plasma is visible in the right image, as are two unused cameras and the operator's fingers.

the vapors interfere with the thin films deposited by microsputtering. Thus, copper tape is applied to the bottom surface of the nozzle, preventing any vapors from reaching the substrate. The tape can be seen in Figure 2-2. With the copper tape applied, EDX measurements do not detect any carbon, a sign that plastic vapors do not reach the substrate.

The design of the nozzle is shown in Figure 2-7; it includes an aperture and two viewholes, which allow for the visual inspection of the plasma. The aperture of the nozzle that was implemented in our setup is a rectangle, measuring 4 to 8 mm in length and 0.6 mm to 2 mm in width at the bottom, with a wider opening towards the top to prevent shadowing effects by the sidewalls of the aperture. This nozzle is attached to a nozzle holder with a set of screws, which can be loosened or tightened to ensure a tight fit and so that the nozzle surface is exactly parallel with the substrate surface. Specifically, the nozzle is lowered within the nozzle holder until it is parallel with and touching the substrate surface. The screws are then tightened and the printhead is raised a small distance (~100 µm) (Figure 2-7). Further details regarding the efficacy of this design can be found in Chapter 3, Section 4.

2.8. Conclusion

This chapter has outlined the hardware employed and developed for this thesis. The printhead brings together fluid, electrical, and multiple mechanical systems for the ambitious goal

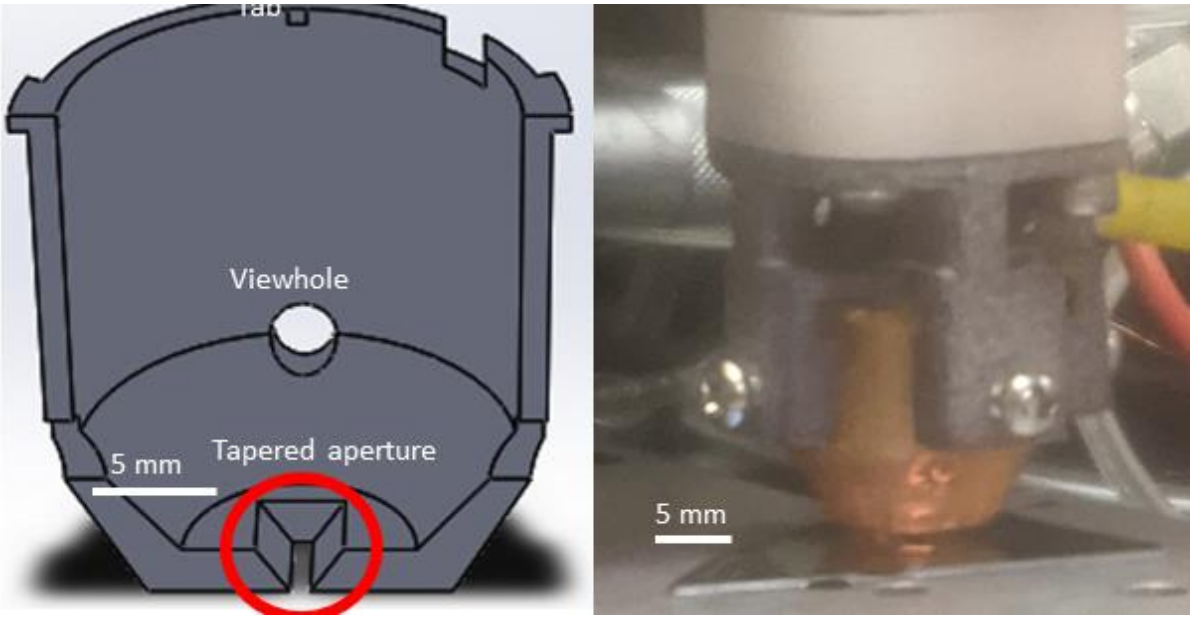

Figure 2-7. Schematic of nozzle (left) and photograph (right) of ULTEM 1010 nozzle attached to nozzle holder. Note the viewhole, which allows for observation of the plasma, and the tabs, for easier attachment of the nozzle to the nozzle holder. The levelling screws are visible in the nozzle holder.

of developing an additive manufacturing system for electronics. We integrate all these systems into a single printhead; the imprints created by the printhead will be discussed in the remainder of this thesis.

2.9. References

[2:1] Kornbluth YS. Focused atmospheric-pressure microsputterer for additive manufacturing of microelectronics interconnects (Master's dissertation, Massachusetts Institute of Technology).

[2:2] Kornbluth YS, Mathews RH, Parameswaran L, Racz LM, Velásquez-García LF. Microsputterer with integrated ion-drag focusing for additive manufacturing of thin, narrow conductive lines. Journal of Physics D: Applied Physics. 2018 Apr 4;51(16):165603.

[2:3] Kornbluth YS, Mathews RH, Parameswaran L, Racz LM, Velásquez-García LF. Room-temperature, atmospheric-pressure microsputtering of dense, electrically conductive, sub-100 nm gold films. Nanotechnology. 2019 Apr 24;30(28):285602.

[2:4] https://www.mecademic.com/en/meca500-robot-arm, accessed 2/2/21.

[2:5] Wu H, Sulkis M, Driver J, Saade-Castillo A, Thompson A, Koo JH. Multi-functional ULTEM™ 1010 composite filaments for additive manufacturing using Fused Filament Fabrication (FFF). Additive Manufacturing. 2018 Dec 1;24:298-306.

[2:6] Máximo DV, Velásquez-García LF. Additively manufactured electrohydrodynamic ionic liquid pure-ion sources for nanosatellite propulsion. Additive Manufacturing. 2020 Dec 1;36:101719.

[2:7] http://www.funtodo.net/our-3d-resin-blends.html, accessed 5/4/21.

Chapter 3 – **In-Plane Resolution**

3.1. Introduction

Given that microplasma sputtering is being developed as a direct-write capability for electronics, it must be capable of writing very small (down to micron level) features. This chapter describes the methods explored in this thesis to increase the resolution of the imprints beyond electrostatic focusing (the approach explored in previous work [3:1],[3:2]). In particular, this chapter will describe the limitations of electrostatic focusing with regard to material that escapes the plasma, the millimeter-scale resolution of hydrodynamic focusing, the efficacy (~50 μm) and thermal effects of minimizing the substrate-plasma gap, and our preferred solution—the use of shadow masks, attached to the printhead, to help resolve very fine features (~300 μm).

3.2. Minimum Feature Size Reduction via Electrostatic Focusing

In previous work, an electrostatic focusing method based on tailoring the electric fields surrounding the microsputterer exit port to guide the positively charged plasma into a long, narrow line was explored [3:1],[3:2]. The charged ions would, due to the high collisionality of our system, shepherd the neutral gold atoms into the same line (ion drag), leading to a highly focused imprint in one direction (down to 9 μm linewidth). However, the physics of the problem are not compatible with focusing the beam on both directions because of the pressure buildup that would occur when a dense gas is compressed into a point.

More significantly, this approach created a feature artifact that affects the effective resolution capabilities of the printing method. While most of the sputtered material can be shepherded by the plasma's ion drag, some of the sputtered gold diffuses away from the main part of the plasma. Once the sputtered material leaves the plasma, it is no longer controlled by the ion drag of the electrostatic focusing and diffuses farther away. This is responsible for a "halo" effect, in which a tightly focused line (~ 200 nm thick) is surrounded by a very thin deposit (> 5 nm thick) with a much larger area. This is obviously deleterious to many working devices, including those that process high-frequency signals, for which the diffuse halo causes plasmonic effects (Figure 3-1).

Electrostatic focusing elegantly harnesses the plasma to help focus the sputtered material. However, this elegance also causes the downfall of this method—while the deposit might have a low full width half maximum (FWHM) dimension, it has a very wide halo. Any material that escapes the plasma is no longer controlled at all. Thus, although electrostatic focusing is helpful to focus the bulk of the plasma, it cannot serve as the full solution. We thus must explore additional methods, which do not depend on the plasma's ion drag, to produce high-resolution patterns. Even if these other methods have higher FWHM dimensions, if they can eliminate or reduce the halo, they might be preferred in our use cases.

3.3. Minimum Feature Size Reduction via Hydrodynamic Focusing

Without electric fields, the transport of the sputtered material to the substrate is driven by diffusion and convection. To estimate each of these methods' contribution to the line width, we

Figure 3-1. A photograph of a focused line. Although the effects of electrostatic focusing are clear in this asymmetric deposit, the light-colored halo surrounding the deposited line shows evidence of errant particles that escaped the plasma and electrostatic focusing mechanism.

define characteristic lengths for each transport process. This section will show that although hydrodynamic focusing (i.e., focusing in which the particles move together with the fluid, in contrast to aerodynamic focusing, in which the particles are separated from the bulk fluid) can produce millimeter-scale resolution under the best of cases, no matter what combination of flows are chosen, we cannot achieve submillimeter resolution. A set of characteristic lengths, representing the radial dispersion of the sputtered material in each phase of the gas's flow, will be defined. These characteristic lengths will represent the maximum dispersion of the sputtered material as it diffuses and convects through the widening flow towards the substrate and allow for the calculation of the sputtered material's spread without the running of an entire simulation for each set of parameters.

To begin, assume there is no outer gas flow. The inner gas flow has an average speed, as it leaves the inner tube, called *v*. As described in Chapter 2, *v* can be adjusted from 0.2 m/s to 200 m/s with a combination of pressure gauges, mass flow controllers, and tubing, as described in Chapter 2. The gas flow is modelled as an incompressible Poiseuille flow with the viscosity of air, coming from a nozzle $d = 700$ μm in diameter, hitting an infinite plate a distance $G = 3$ mm away (Figure 3-2).

With these dimensions, the flow is laminar (Re<2000) for *v* less than 40 m/s, which includes the areas of highest interest. Turbulent flow will lead to more undesired spreading of the sputtered material, due to vortices and eddies. As a result, the analysis will primarily focus on the laminar regime, noting that when the turbulent regime is examined, the resolution found is an upper bound, since the calculations neglect the deleterious effects of turbulence.

Following [3:3], the flow is divided into three regions (Figure 3-2). As the flow leaves the nozzle, it streams vertically (towards the substrate) with minimal interference from the substrate; this is known as the *free-flow region*. As the flow nears the substrate, the pressure buildup near the point at which the flow impinges on the substrate causes the flow lines to expand radially; this region of expansion is known as the *impingement region*. Once the flow is near the substrate, its velocity towards the plate becomes insignificant, and the streamlines point in the radial direction, parallel to the substrate; this region is known as the *wall jet region*.

Convection is present in the two latter regions. To model the species' transport due to convection, we must first understand, qualitatively, the behavior of the fluid. We use mass continuity and conservation of momentum equations, assuming an incompressible fluid, as is appropriate for the flow speeds (far smaller than the speed of sound, i.e., 343 m/s) and neglect viscosity (Re>>1) and gravity. The continuity equation is

$$-\frac{\partial v_z}{\partial z} = \frac{1}{r}\frac{\partial (r v_r)}{\partial r} = \frac{\partial v_r}{\partial r} + \frac{v_r}{r} \tag{3-1}$$

and the conservation of momentum equations are:

$$v_r \frac{\partial v_r}{\partial r} + v_z \frac{\partial v_r}{\partial z} = 0 \tag{3-2}$$

$$v_r \frac{\partial v_z}{\partial r} + v_z \frac{\partial v_z}{\partial z} = 0 \tag{3-3}$$

By defining a velocity v_0 and a length x_0, (e.g., initial velocity and G) and defining

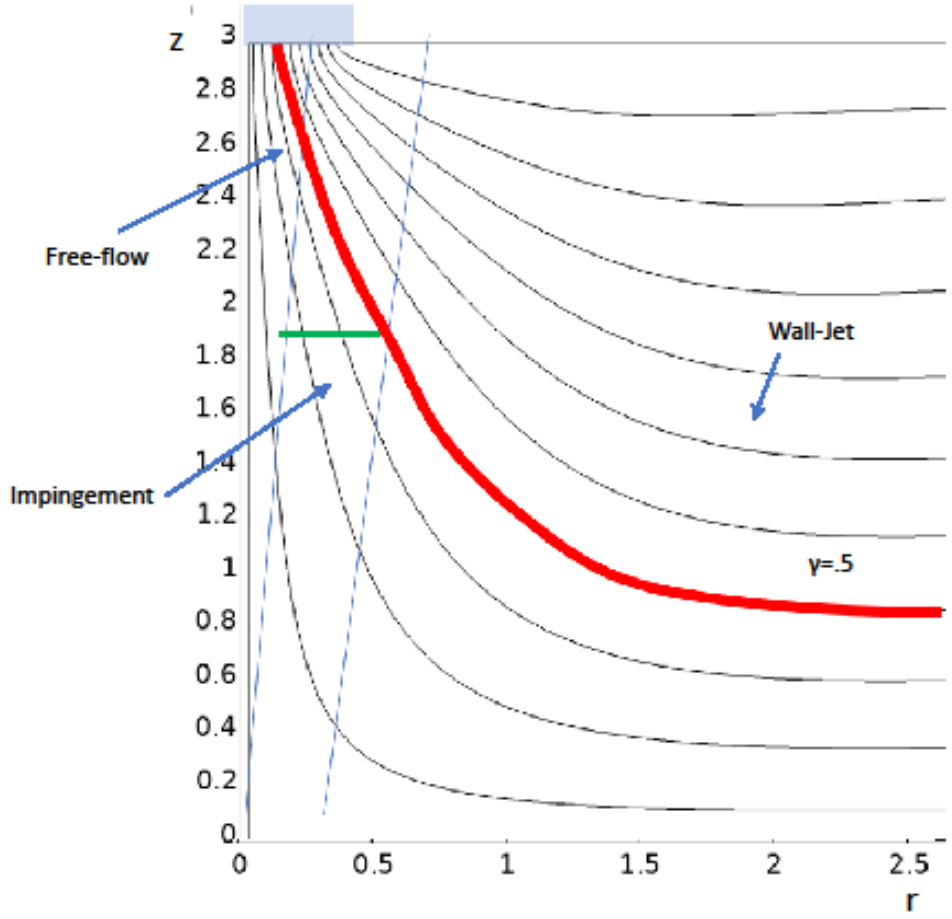

Figure 3-2. Streamlines of the inner gas flow in a typical geometry. Once the gas flow enters the wall-jet regime, it expands to fill the entire gap. The shape of streamlines does not depend on the velocity, allowing for a partially-analytical exploration of the parameter space. A given streamline, for a γ of 0.5 (i.e., halfway towards the inner diameter of the inner tube) is highlighted in red; a green line, stretching from the radial distance where the streamline leaves the nozzle to where it has a 45 degree angle, is the impingement characteristic distance. The nozzle is displayed as a transparent blue rectangle.

$$\alpha = \frac{v_z}{v_0}, \tag{3-4}$$

$$\beta = \frac{v_r}{v_0} \tag{3-5}$$

$$R = \frac{r}{x_0} \tag{3-6}$$

$$Z = \frac{z}{x_0} \tag{3-7}$$

we can nondimensionalize these equations, so that Equations (3-8) – (3-10) are parallel to Equation. (3-1) – (3-3):

$$-\frac{\partial \alpha}{\partial Z} = \frac{\partial \beta}{\partial R} + \frac{\beta}{R} \tag{3-8}$$

$$\beta \frac{\partial \beta}{\partial r} + \alpha \frac{\partial \beta}{\partial Z} = 0 \tag{3-9}$$

$$\beta \frac{\partial \alpha}{\partial r} + \alpha \frac{\partial \alpha}{\partial Z} = 0 \tag{3-10}$$

Since the choice of v_0 is independent of the choice of x, it is clear that the shape of the streamlines, for a given geometry, are independent of the velocity. That is, for a given solution to the dimensionless equations (3-8) – (3-10), an appropriate v_0 and x_0 can be selected to scale to the chosen conditions. In these investigations, x_0 will not change, but v_0 will be changed as v is varied. This allows for the exploration the behavior of the flow for a wide range of values of v at once.

COMSOL Multiphysics was used to simulate this axisymmetric system, using the Laminar Flow Module to find a stationary (i.e., not time-dependent) solution for the boundary conditions. The streamlines of the 700 μm-diameter inner flow are traced. The simulations show, as is derived above, that over a long range of gas speeds, there is no change in the streamlines, and thus the convective transport of the fluid. Instead, each streamline begins flowing downwards from the tube, and, as it approaches the substrate surface, it will flow parallel to the substrate, displaced set vertical distance from the substrate. An impingement region separates these two flows.

Consider the free-flow region first. Assuming, as the literature suggests, e.g., [3:3],[3:4], that the flow speed is nearly constant as the gas streams towards the substrate in the free-flow regime, the sputtered material will reach the substrate in approximately

$$t = \frac{G}{v} \tag{3-11}$$

From the diffusion equation,

$$\varphi(x,t) = \varphi_0 e^{\left(-\frac{x^2}{4Dt}\right)} \tag{3-12}$$

where φ and φ_0 are the concentration and initial concentration respectively, x is the distance across which the material diffuses, D is the diffusion constant and t is the time of Equation (3-11), a characteristic diffusion length, the first characteristic length, can be defined:

$$x = \sqrt{4Dt} = \sqrt{\frac{4DG}{v}} \tag{3-13}$$

which for gold in air in the geometry used, is $\frac{5.1\times10^{-4}m^{1.5}s^{-0.5}}{\sqrt{v}}$. For the aforementioned range of $v = 0.2 - 40$ m/s, this length ranges from 1.1 mm to 80 μm—large at low speeds, but less significant at high speeds.

In order to take advantage of the independence of the shape of the flow field on the velocity, a dimensionless parameter γ is defined. γ represents the fraction of the inner gas flow radius that will have an appreciable amount ($\varphi = \frac{\varphi_0}{e}$) of sputtered material. The parameter γ can be found by adding the target wire diameter to the free-flow characteristic diffusion length, and then dividing the sum by the radius of the inner gas flow ($\frac{d}{2}$, 350 μm in this case); consequently, γ ranges from 3.4 (0.2 m/s) to 0.37 (40 m/s) over the laminar flow range. At very low speeds, the sputtered material diffuses far outside the inner gas flow, while at high speeds its diffusion is limited to slightly more than a third of the radius of the gas flow. The streamlines are assumed to expand and contract proportionally, i.e., the streamline that begins a fraction γ between the outermost streamline and innermost streamline will always be that fraction between those two streamlines.

For the impingement region, where the flow is partially towards the plate and partially towards the sides, the definition of a characteristic length is not obvious. The radial flow, which contributes to the radial spread, not the flow towards the plate, which is larger in magnitude for a majority of the impingement region, is of interest. Thus, a radial distance is used, measured between where the outermost streamline that carries sputtered material (i.e., $\gamma \cdot d/2$) and where that streamline's radial and vertical velocities are equal (see Figure 3-2). At this point, the outer streamline is still far from the substrate, and thus diffusion from this streamline to the substrate is insignificant, but the flow still carries the sputtered flux radially outwards, before any significant diffusion to the substrate. Thus, this can be seen as the radial distance that convection carries the sputtered material before the diffusion of the wall-jet region becomes relevant. For the given choices of d and G, this value, the second characteristic length, is

$$1.95\gamma d, \tag{3-14}$$

with the prefactor being found computationally by measuring the angle of the flow's streamlines. Compared to the free-flow characteristic diffusion length, $0.5\gamma d$, it is apparent that the impingement characteristic distance is approximately quadruple the free-flow characteristic diffusion length. Physically, this represents the phenomenon that the flow will approximately quadruple in diameter between the nozzle and the point at which the radial and vertical velocities are equal; once sputtered material reaches the outer portions of the flow, convection carries it much further away from the center of the flow than diffusion allow would carry it.

For the wall-jet stage, the diffusion equation described above (Equation (3-12)) is used to describe a characteristic t. Rearranging Eq. (3-12),

$$t = \frac{L^2}{4D} \tag{3-15}$$

after which time a significant amount of the flux will diffuse from the uppermost streamline that carries sputtered material to the substrate, where it will be adsorbed. Since the streamlines are assumed to expand proportionally, and the uppermost streamline is $0.9G$ (2.7 mm) above the surface, the uppermost streamline that carries sputtered material is $0.9\gamma G$ above the surface, with that distance used as L in Eq. (3-15). Note that, in contrast to [3:4], [3:5], transport due to vortices is neglected. Vortices are neglected both for computational simplicity and because, at the velocities present, the Reynolds number is low enough (Re<2000) that vortices can be ignored.

The time, $t = \frac{.81\gamma^2 G^2}{4D} = \gamma^2 65$ ms, can then be multiplied by the characteristic speed of the gas, v, to calculate a distance. This distance is a measure of **convective** transport (in contrast to L, which is a measure of **diffusive** transport); the distance measures how far (radially) the flow can carry the diffused material while material that has diffused outwards during the free-flow regime can now diffuse back inwards during the wall-jet regime. Thus, the characteristic lengths are tracking sputtered material as it diffuses outwards, is convected by the flow through the impingement region, and then diffuses towards the substrate. This calculation is an oversimplification; as the fluid flows radially, it will slow, due to conservation of mass. Nevertheless, this characteristic distance is a useful approximation.

This convective characteristic distance can also be connected to traditional dimensionless numbers. The distance, the third characteristic length is just

$$\frac{0.81\gamma^2 G^2 v}{4D} = \frac{L^2 v}{4D} = L * \frac{Pe}{4} \tag{3-16}$$

where Pe is the dimensionless Peclet number, the traditional measure of the relative strength of convection as compared to diffusion. Thus, our characteristic length is simply the distance that material must diffuse, divided by four and multiplied by a factor converting diffusive length to conductive length.

Thus, there are three characteristic distances: one for diffusion—the distance the sputtered material will spread during the free-jet flow; one for the width of the impingement region— the distance that the material will convect as the flow changes direction; and one for convection—the distance the material will spread during the wall-jet phase before it diffuses towards the substrate and adsorbs onto the substrate. Physically, the sum of these distances represents the spread of material that diffuses outwards during the free-flow regime, follows the streamline during the impingement regime, and diffuses back towards the substrate during the wall-jet flow, with each term describing the radial spread of one of those stages. These are graphically shown for a typical geometry for a range of gas speeds (Figure 3-3). It is clear that, over the entire range of interest, the convection in the wall-jet region dominates. Even at the slowest speeds, where all three lengths are of similar size, the sum of the lengths is over 12 cm—far too large.

The addition of an additional flow, while helpful, is insufficient to achieve the desired resolution. One control available to change the shape of these streamlines is the outer flow. In the absence of an outer flow, the inner flow will expand to fill the entire gap between the substrate and

the printer in the wall-jet phase. However, the addition of an outer flow will compress the

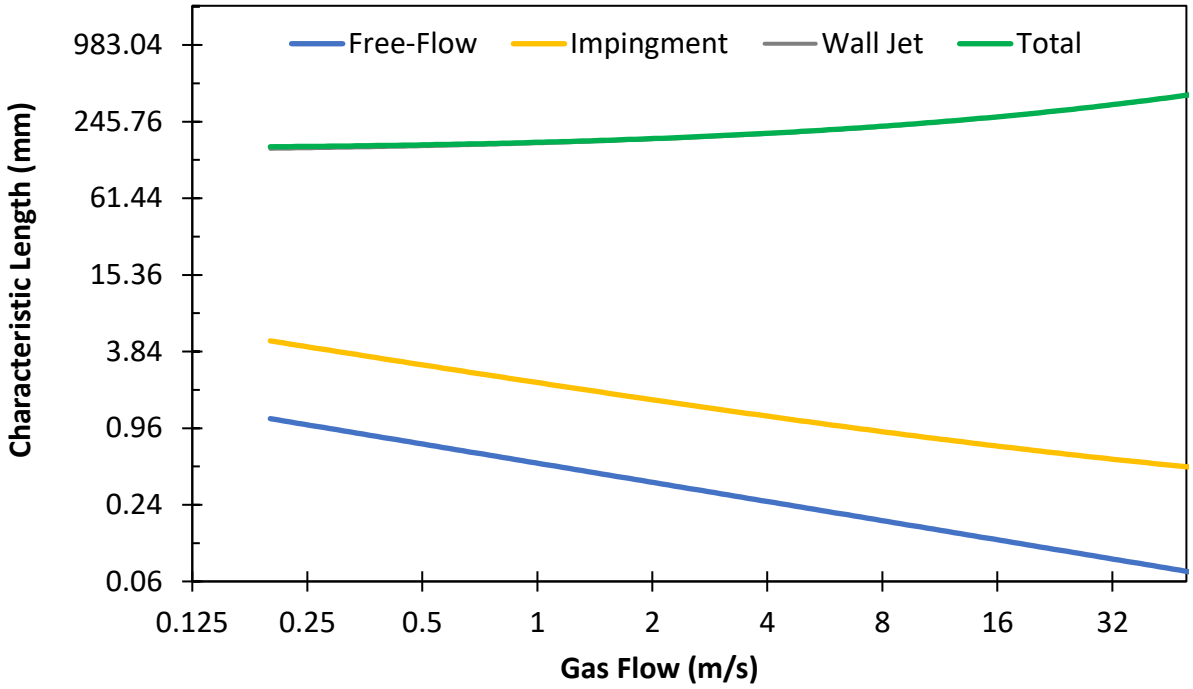

Figure 3-3. Characteristic lengths for the single-jet model, across the range of the laminar flow regime. The convection in the wall jet region dominates, at all speeds; the total characteristic length is nearly identical to the wall jet characteristic length.

inner flow to a fraction of that area [3:7], [3:8]. An extremely strong outer flow (100-fold faster than the inner flow) will remove the impingement regime and compress the inner flow, in its radial regime, to 40 µm above the substrate (Figure 3-4). In this extreme case, the characteristic distances are lower, but still too high (Figure 3-5). Note that only the lowest values of v_0 are physically reasonable for this equation; once $v_0 > 3.4\frac{m}{s}$, the outer gas flow exceeds the speed of sound, and the laminar flow model is entirely inappropriate. Nonetheless, this physically impossible region is included in the graph for the sake of completeness. Even in the range of $v_0 > 3.4\frac{m}{s}$, as the outer flow approaches the speed of sound, the compressibility of the outer flow must be accounted for. If compressibility is neglected, the calculations will overestimate the focusing effects of the outer flow. Thus, by neglecting compressibility, these calculations give an upper bound on the resolution and a lower bound on the characteristic distances.

Even with such a set of parameters, the sum of characteristic distances would only be 325 µm, or a line width of 750 µm, including the initial 100 µm width of the wire. If we limited ourselves to an outer flow a mere 30x faster than the inner flow of 11 m/s, approaching the speed of sound, the transition region would still disappear (Figure 3-6), but the minimum sum of characteristic distances would be 410 µm, or a line width of 920 µm – millimeter scale, in the best

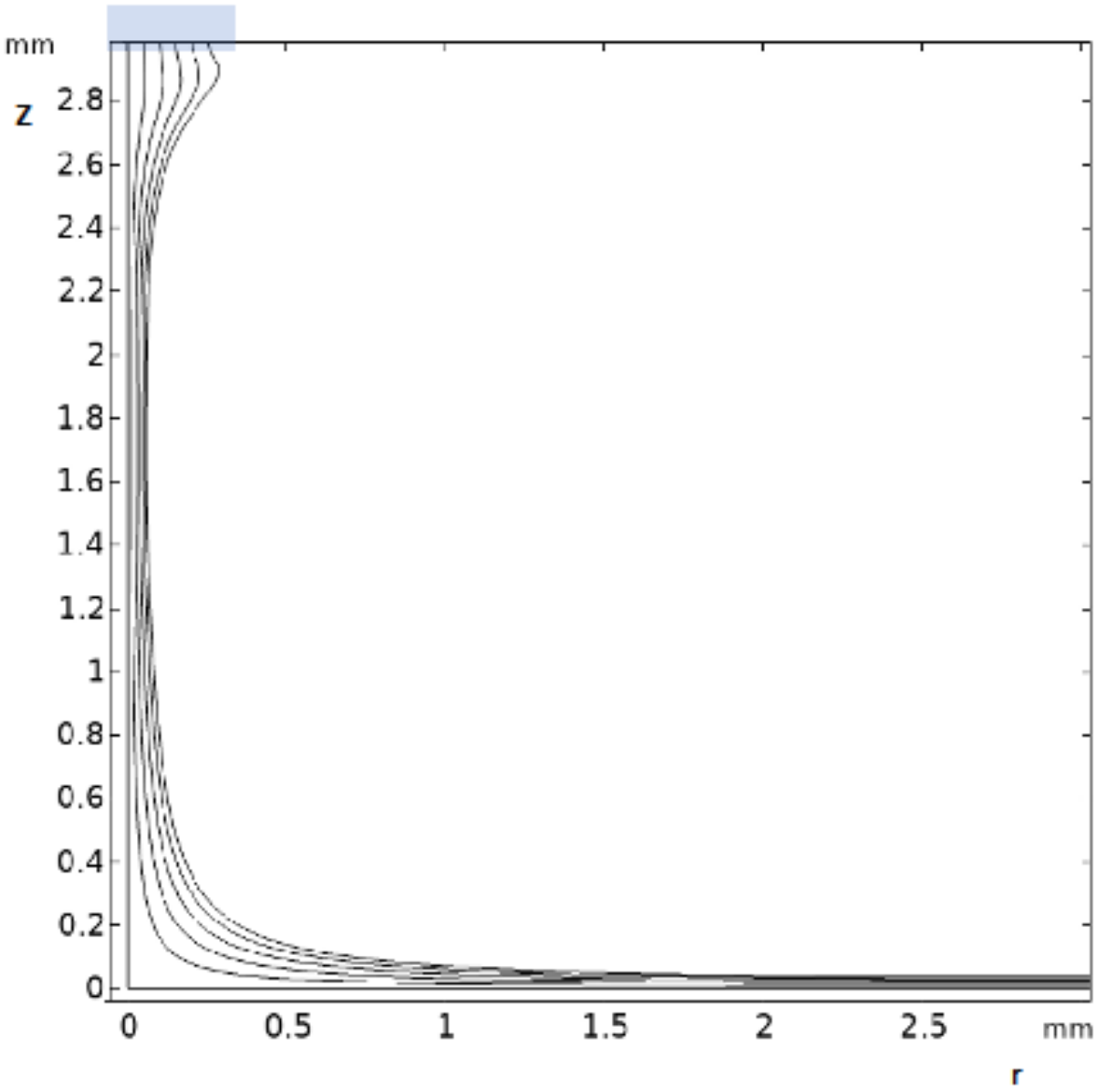

Figure 3-4. Streamlines of the inner flow from a system with both an inner gas flow and an outer gas flow, separated by a 400 µm glass tube wall and with the outer flow 100x faster. The faster outer flow compresses the inner flow in both the free-flow and wall-jet regions, and shrinks the impingement region to a minimal size. The nozzle is represented by a transparent blue box.

of circumstances, and still require approaching the speed of sound and neglecting compressibility (Figure 3-7).

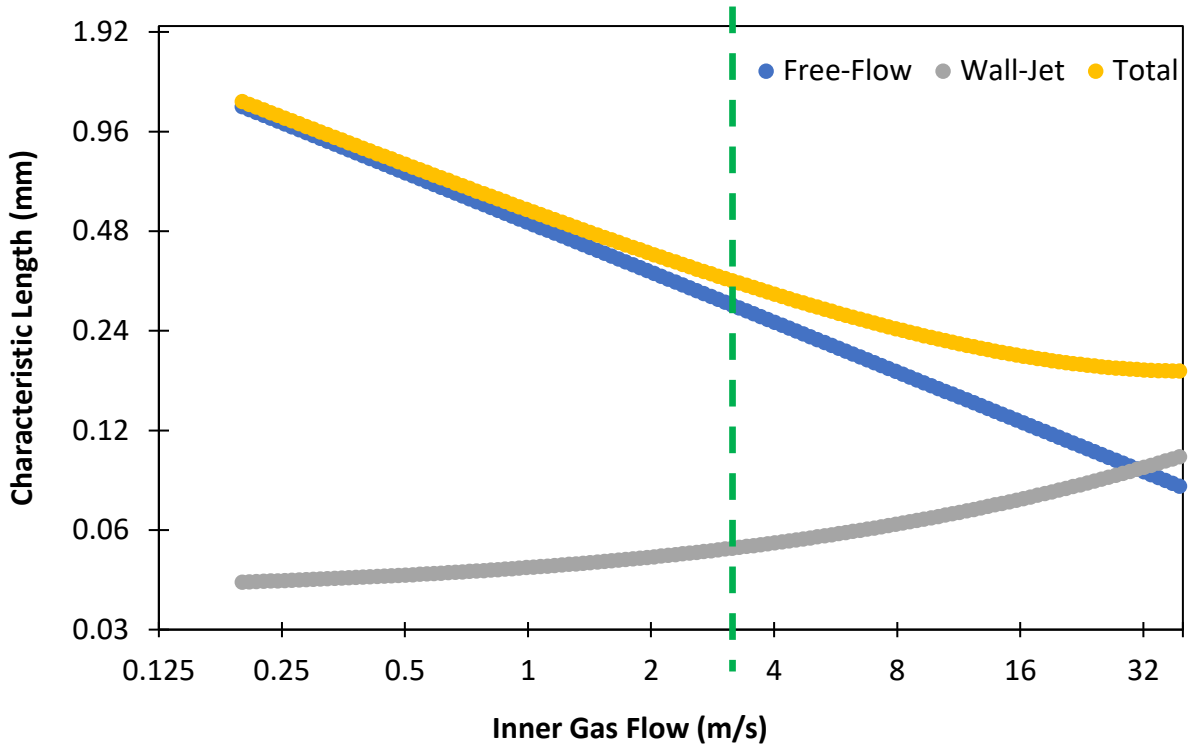

Figure 3-5. Characteristic lengths of the inner flow, when the outer flow is 100x the velocity of the inner flow. Note that at the higher end of this regime (right of the green line; inner flow >3.4 m/s), the outer gas flow is supersonic and outside the range of our model. Thus, although the resolution at such a point is attractive, much of this graph is not physically valid.

Thus, using fluid transport only, the resolution cannot be improved beyond millimeter scale. Fast flow leads to poor resolution due to diffusion, while slow flow leads to poor resolution due to convection. This problem has plagued other additive manufacturing methods that also depend on gas flows, such as ink-jet methods [3:9]. Even when clever manipulation of the flow can concentrate particles in a particular region, a small fraction of particles will always escape [3:10].

Consequently, although the beam can be highly focused, whether electrostatically or with other methods, in one direction until the moment it impinges on the substrate, once it impinges on the substrate, the velocity towards the substrate will quickly change direction, due to conservation of kinetic energy. This will not significantly affect the fraction of the sputtered material nearest the center of the deposit, but it will carry a small fraction of the diffused sputtered material away from the focused line itself.

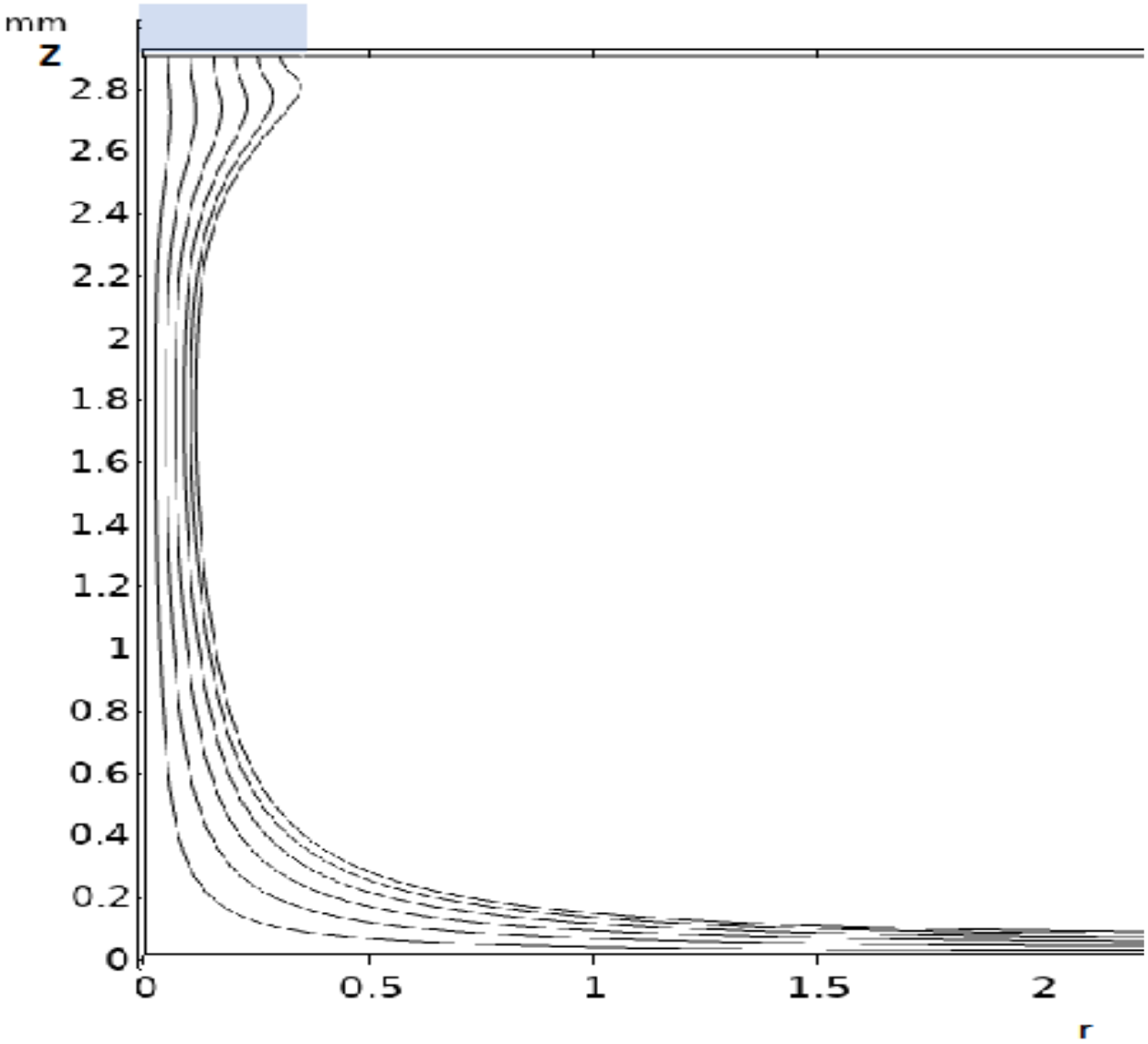

Figure 3-6. Inner flow streamlines of a system with an inner gas flow and an outer gas flow, separated by a 400 µm glass tube wall and 30x faster than the inner flow. The faster outer flow compresses the inner flow in both the free-flow and wall-jet regions, and shrinks the impingement region to a minimal size, although not to the same extent as in Figure 3-4.

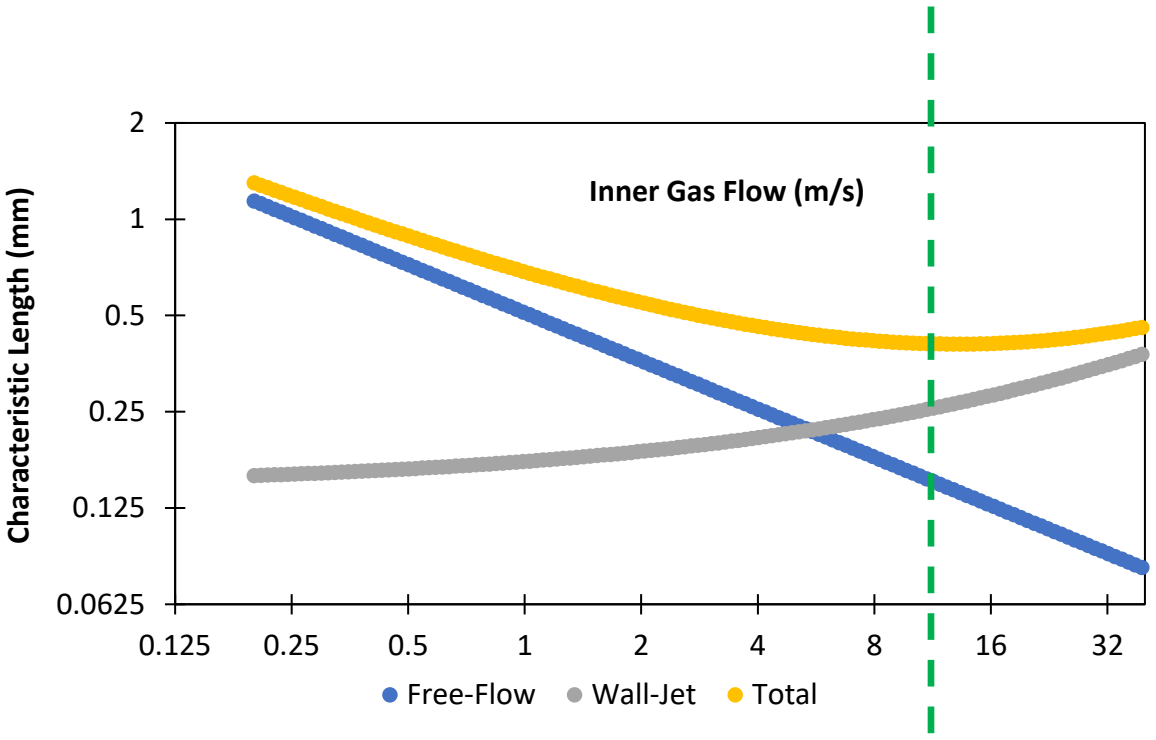

Figure 3-7. Characteristic lengths of the inner flow, when the outer flow is 30x the velocity of the inner flow. The minimum characteristic length is 407 µm, albeit with a barely supersonic outer gas flow. As before, the green line demarcates the speeds at which the outer flow is supersonic; at the green line, the minimum characteristic length is 410 µm. This shows the futility of relying solely on gas flow to constrain the sputtered material.

3.4. Minimum Feature Size Reduction via Nozzle Separation and Mask Shadowing

Note that all of the characteristic lengths discussed previously are dependent on G, the plasma-substrate distance; the free-flow diffusive length (Equation (3-12)) on $\sqrt{G}$, the impingement distance (Equation (3-14)) on $\gamma \propto G + 0.5d$, and the wall-jet's convective length (Equation (3-16)) on $G^2\gamma^2 \propto G^2(G + 0.5d)^2$. Thus, by minimizing G, all of these lengths are decreased, particularly the convective length, which, for most cases, is the largest. This section will introduce two methods of doing so, lowering the printhead and introducing a nozzle.

Most simply, both diffusion and horizontal convection can be minimized by placing the source of the flow near the substrate. However, this has shown to cause unacceptable substrate heating in reported microplasma sputterers [3:11]-[3:13].

Instead, the sputtering system is separated from the source of the flow with the use of a nozzle. Because our system operates at low power (~2 W), a plastic nozzle placed a short distance

(~4 mm) away from the printhead does not reach its softening temperature. To allow for an even shorter nozzle-printhead gap (1.5 mm) and higher power, ULTEM 1010 and FunToDo Industrial Blend, high-temperature resins, are used, as described in Chapter 2.8.

The aperture of the nozzle is placed 5 mil (127 µm) above the flat substrate surface, held into place with leveling screws. This very short distance allows for the minimizing of spread caused by either diffusion or convection; a relatively slow flow (500 sccm inner flow and 1000 sccm outer flow; 18 m/s and 6 m/s, respectively) does not have significant diffusion or convection once the stream leaves the aperture. This has been confirmed experimentally as well (Figure 3-8). Specifically, the total line width of our deposit is approximately the sum of the aperture width and the nozzle-substrate gap, or 200 µm wider than the aperture. The halo is nearly non-existent (Figure 3-9)

Ideally, even this 127 µm gap should be minimized. Consequently, 10 µm-wide apertures patterned on a 100 µm-thick Kapton film were laid directly on the substrate; with such setup, definition of 1.5 µm linewidth was possible (Figure 3-10). There was significant shadowing; much of the sputtered material adhered to the Kapton, as is expected with any masking technique that uses rectangular apertures in a thick mask.

While laying the film directly on the substrate leads to excellent resolution, it is not suitable for a direct-write system. A direct-write system requires that the aperture move with the substrate to trace out arbitrary patterns. Thus, in our embodiment, the aperture must to be attached to the printhead, as the nozzle is. Even so, the advantages of the Kapton mask can be captured by shrinking the gap between the mask and the substrate to an infinitesimal size. An optical alignment system can improve on our current contact-based alignment system to reach this. However, this is beyond the scope of this thesis.

3.5. Comparison to Prior Work

The use of a nozzle is not, in and of itself, particularly groundbreaking. However, it is an important step in the development of a direct-write system for microelectronics. With a 3-D printed nozzle, we can build on the results of [3:2], eliminating the undesired halo. With the combination of electrostatic focusing and a nozzle, line widths as narrow as 300 µm with no halo have been demonstrated, and with the use of a Kapton mask laid directly on the substrate, line widths as narrow as 1.2 µm have been shown.

This advance makes atmospheric microsputtering competitive with other direct-write methods for electronics, even without the advantages that other methods have. Other methods typically use a liquid binder to hold together conductive nanoparticles, or aerodynamic focusing to separate large nanoparticles from smaller air molecules. Microsputterer printing cannot manipulate a liquid, because it has have no liquid binder, and cannot use aerodynamic focusing because the smallest particles, individual sputtered atoms, are the same size as the carrier gas's molecules. In this context, these results should not be seen as merely duplicating other results, but as finding a new method that works in microsputtering.

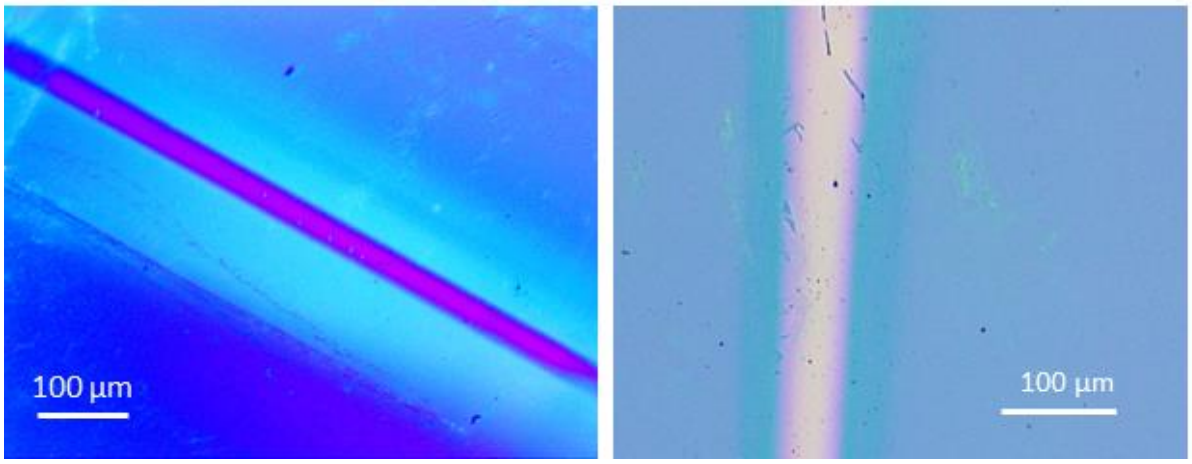

Figure 3-8. Photographs of two aperture-defined lines, with minimal halos. Both lines are well defined and the halo is small (total line width with halo: 150 µm on left, 90 µm on right) and the size of the gap between the bottom of the nozzle and the substrate (gap on left:125 µm; gap on right, 25 µm).

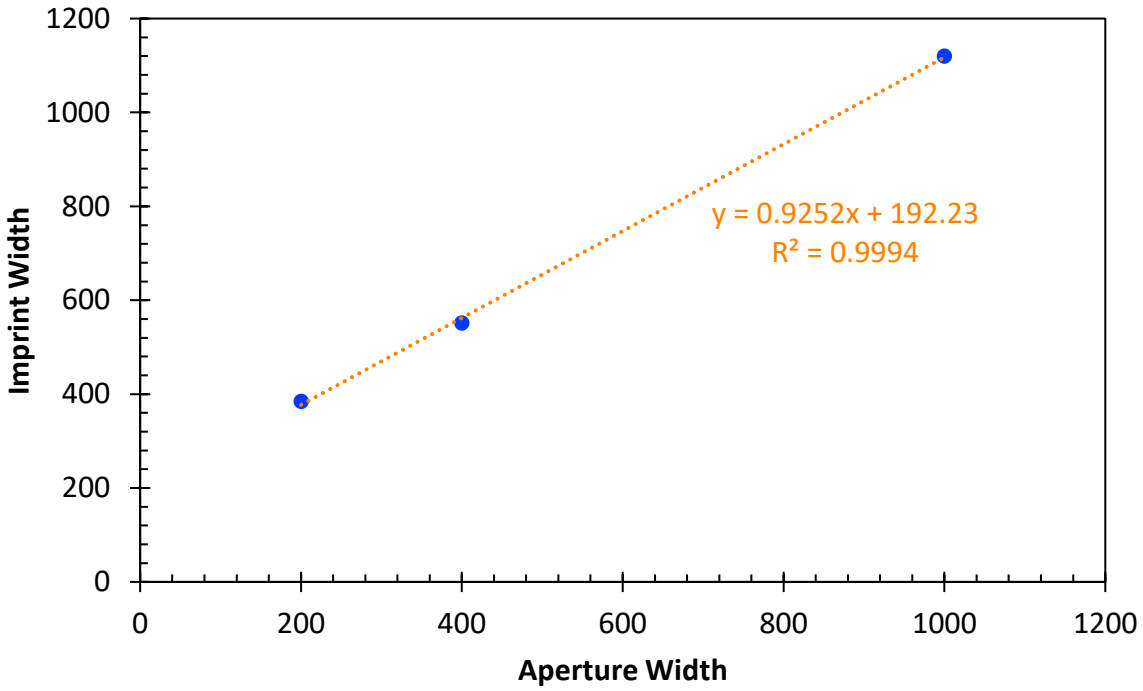

Figure 3-9. Deposit width as a function of aperture width, for a variety of different nozzles. The nozzle was kept 125 µm above the substrate in each case, and the total line width is approximately the sum of the aperture width and 200 µm, representing 100 µm of spread from the aperture on each side. A smaller nozzle-substrate gap, as in Figure 3-8, lessens this.

Specifically, compare our results to the best results of inkjet printing, aerosol printing, and microsputtering. The finest resolution inkjet printers report resolution of ~100 µm, due the

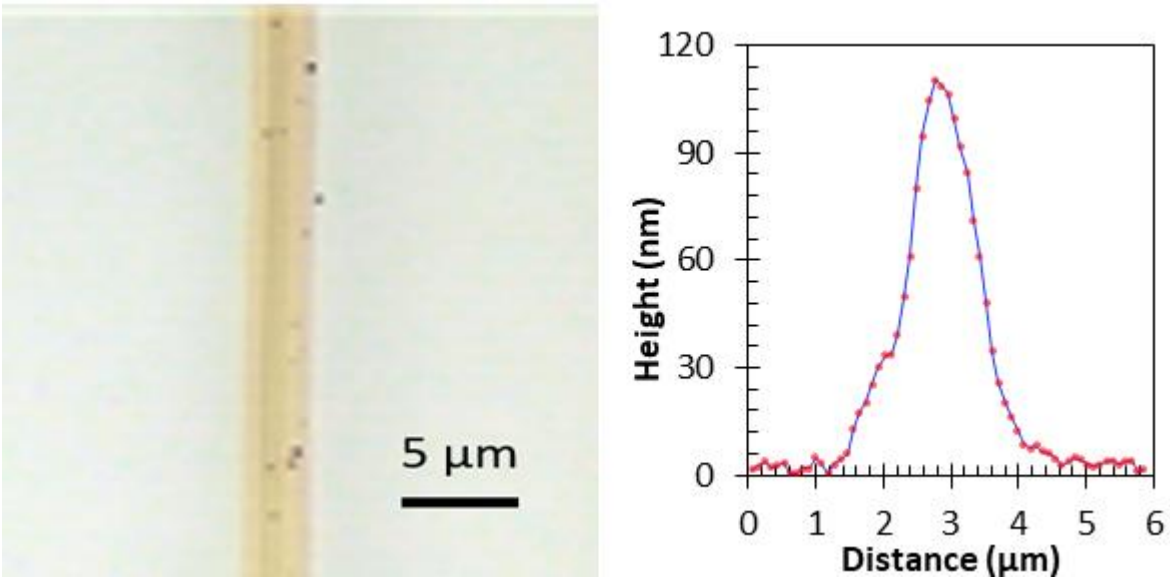

Figure 3-10. Micrograph and profile of deposit defined by Kapton mask laid directly on the substrate. While this method of masking is not suitable for direct-write manufacturing, it shows the limit of aperture-defined resolution.

rheological properties of the ink [3:14]. Aerosol jets, such as Optomec, use aerodynamic focusing (i.e. separate large particles from the carrier gas, as opposed to hydrodynamic focusing, in which the particles and carrier are treated identically) to achieve a linewidth of 10 µm [3:15]. Other microsputtering devices, which minimize the substrate-target gap, have a linewidth of 50 µm [3:13]. Our linewidth is within an order of magnitude of these values. To improve it further, we might improve the alignment between the nozzle and the substrate, as described, or mill a nozzle out of metal, to further decrease its aperture's dimensions.

3.6. Summary

In this chapter, we extended the work reported in [3:1],[3:2]. We described how electrodynamic focusing, while it leads to narrow linewidths if we only look at the FWHM metric, also leads to unacceptable "halos"—very wide, very thin collections of metal outside the main deposit. Several methods of removing the halo were explored. Hydrodynamic focusing, with an ideal set of flows, can only achieve millimeter resolution due to the deleterious effects of convection and diffusion. Minimizing the substrate-plasma gap can lead to 50 µm resolution, but at the cost of substrate heating. Features as narrow as 2 µm were demonstrated. More practically, an aperture in a nozzle, which combines the thermal properties of a large plasma-substrate gap with the transport of a small gap, was found to allow for 90 µm resolution. This chapter further identified a path forward towards even finer resolutions, although this refinement has not yet been implemented.

3.7. References

[3:1] Kornbluth YS, Mathews RH, Parameswaran L, Racz LM, Velásquez-García LF. Microsputterer with integrated ion-drag focusing for additive manufacturing of thin, narrow conductive lines. Journal of Physics D: Applied Physics. 2018 Apr 4;51(16):165603.

[3:2] Kornbluth YS. Focused atmospheric-pressure microsputterer for additive manufacturing of microelectronics interconnects (Masters dissertation, Massachusetts Institute of Technology, 2018).

[3:3] Deshpande MD, Vaishnav RN. Submerged laminar jet impingement on a plane. Journal of Fluid Mechanics. Cambridge University Press; 1982;114:213–36.

[3:4] Van Hout R, Rinsky V, Grobman YG. Experimental study of a round jet impinging on a flat surface: flow field and vortex characteristics in the wall jet. International Journal of Heat and Fluid Flow. 2018 Apr 1;70:41-58.

[3:5] Anderson SL, Longmire EK. Particle motion in the stagnation zone of an impinging air jet. Journal of Fluid Mechanics. 1995 Sep;299:333-66.

[3:6] Scholtz MT, Trass O. Mass transfer in the laminar radial wall jet. AIChE Journal. 1963 Jul;9(4):548-54.

[3:7] Wang XK, Tan SK. Experimental investigation of the interaction between a plane wall jet and a parallel offset jet. Experiments in Fluids. 2007 Apr;42(4):551-62.

[3:8] Mondal T, Das MK, Guha A. Numerical investigation of steady and periodically unsteady flow for various separation distances between a wall jet and an offset jet. Journal of Fluids and Structures. 2014 Oct 1;50:528-46.

[3:9] Feng JQ. Mist flow visualization for round jets in Aerosol Jet® printing. Aerosol Science and Technology. 2019 Jan 2;53(1):45-52.

[3:10] Feng JQ. A Computational Study of Particle Deposition Patterns from a Circular Laminar Jet. Journal of Applied Fluid Mechanics. 2017;10(4):1001-12.

[3:11] Burwell IV ED. A microplasma-based sputtering system for direct-write, microscale fabrication of thin-film metal structures (Masters dissertation, Case Western Reserve University, 2016).

[3:12] Abdul-Wahed AM, Roy AL, Xiao Z, Takahata K. Direct writing of thin and thick metal films via micro glow plasma scanning. In2016 IEEE 29th International Conference on Micro Electro Mechanical Systems (MEMS) 2016 Jan 24 (pp. 443-446). IEEE.

[3:13] Abdul-Wahed AM, Roy AL, Xiao Z, Takahata K. Direct writing of metal film via sputtering of micromachined electrodes. Journal of Materials Processing Technology. 2018 Dec 1;262:403-10.

[3:14] Valentine AD, Busbee TA, Boley JW, Raney JR, Chortos A, Kotikian A, Berrigan JD, Durstock MF, Lewis JA. Hybrid 3D printing of soft electronics. advanced Materials. 2017 Oct;29(40):1703817.

[3:15] Feng JQ, Renn MJ. Aerosol jet® direct-write for microscale additive manufacturing. Journal of Micro and Nano-Manufacturing. 2019 Mar 1;7(1).

Chapter 4 – **Influence of Nanoparticles on the Adhesion of Microsputtered Gold Thin Films**

4.1. Introduction

This chapter discusses how the creation of nanoparticles in the plasma and their spatial stacking during film formation can be harnessed to greatly improve the adhesion of microsputtered gold thin films. Much of the material in this chapter was published in the journal *Additive Manufacturing* [4:1] in December of 2020.

Specifically, the chapter first reviews the state of the art on thin film adhesion. Then, the chapter demonstrates via a series of experiments that the gas flow rate fed to the microplasma reactor has the strongest effect on film adhesion across all the process parameters. After that, the chapter shows via simulations, plasma theory, and contemporaneous work that at high (>4 slm) flow rates nanoparticles are created in the plasma; these nanoparticles can be large (>100 nm, streaming near the axis of the flow) or small (created in the periphery of the plasma or streaming around the central, large-nanoparticle volume). Finally, the chapter describes how, by controlling the gas flow rate and rastering the print head, tight packing of nanoparticles of different sizes is achieved, resulting in films with large adhesion.

4.2. Sources of Film Adhesion

Film adhesion can be characterized by measuring the force, either normal or tangential, necessary to delaminate the film, i.e., to break the atomic bonds between the thin film and the substrate [4:2]. The sources of film adhesion can be divided by the nature of the atomic bonds involved. For example, some atomic bonds are caused by Van der Walls forces, where the mere placement of the film's atoms next to the substrate's atoms causes a small amount of charge separation and electrical attraction. This force is relatively weak, but it can be enhanced by increasing the surface area between the thin film and the substrate, which can be done by either (i) removing contaminants from the interface between the film and the substrate via physical and chemical methods [4:3], or (ii) increasing the contact area between the film and the substrate's surface, either by roughening the surface or by adding a naturally rough adhesion layer, e.g. chromium or titanium [4:4]. Given that all films have a certain porosity, ensuring that the portion of the film in direct contact with the substrate is as dense as possible can also increase adhesion.

Another source of film adhesion is the use of covalent bonds. If the thin film's and substrate's atoms can form a compound, the covalent bond makes it more difficult to separate the thin film from the substrate. This compound bond can be strengthened by (i) removing contaminants from the film-substrate interface [4:5]; (ii) introducing a material that bonds to both substrate and film; (iii) encouraging thermal migration of the film's atoms into the substrate, so that instead of a sharp transition between materials, a continuum, with a gradual gradient of film material, is formed [4:6]; or (iv) modifying the substrate with pre-sputtering to prime it to bond to

the soon-to-be deposited film [4:7]. All of these chemical methods heavily depend on the choice of substrate and film material; unfortunately, gold is notoriously inert.

4.3. Film Structure of a Static Gold Microsputtered Imprint

In the absence of a strong gas flow (<500 sccm) and without rastering the printhead, the microsputtered gold film is homogenous and generally dense, with the presence of small voids dependent on the energy of sputtered atoms, as described in Chapter 5. However, in the high-flow case (>4 slm; intermediate regimes between 500 sccm and 4 slm were not explored until Chapter 6) referred to in this thesis as *the jet-assisted microsputtering regime*, without rastering the printhead, the film shows two distinct regions: a first region, right below the microsputterer target, that is optically dark and highly porous, with pores as large as 100 nm; these regions are called

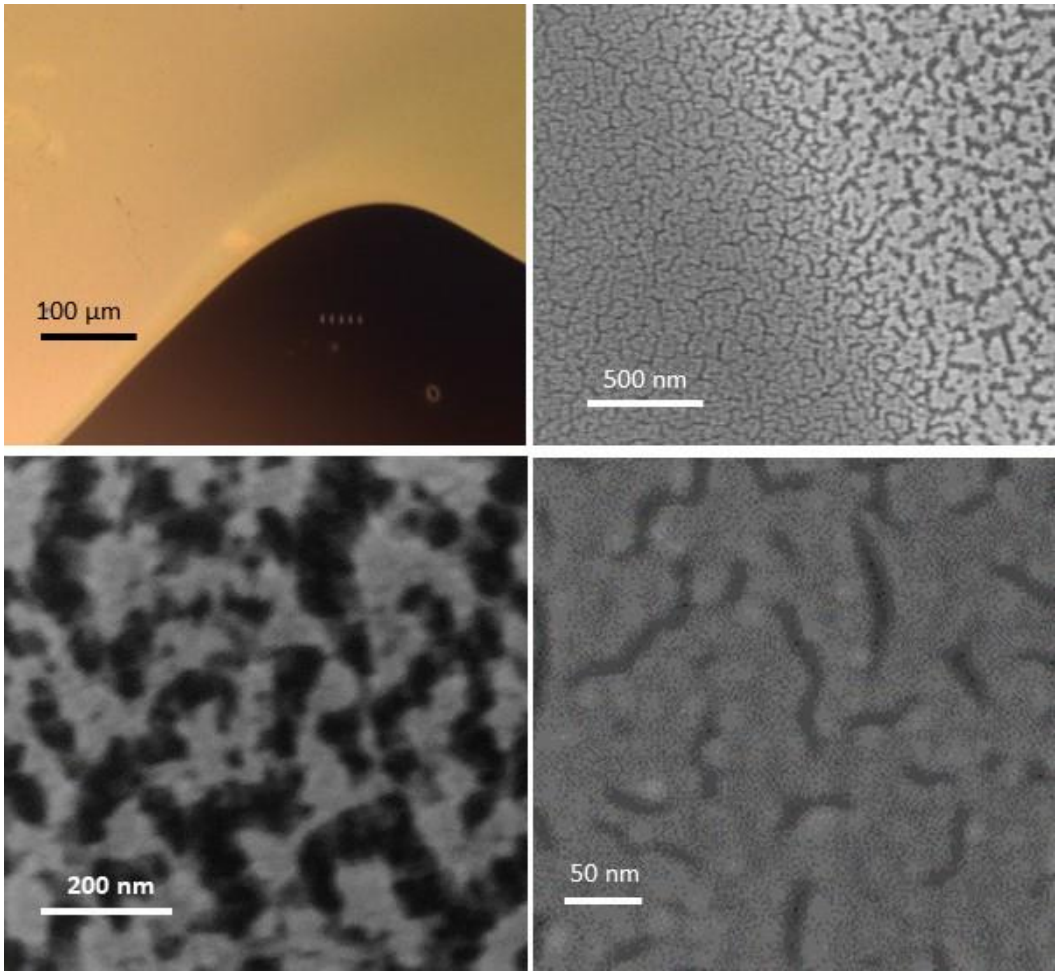

Figure 4-1. Optical (top left) and SEM (remainder) micrographs of the porous structure produced via jet-assisted microsputtering. Directly under the printhead, the deposit is highly porous (bottom left) and optically dark. Farther away, the film is significantly denser (bottom right) and gold colored. The transition between the two regions is small but visible in SEM (top right).

dark in this thesis. A second region, surrounding the porous region, is significantly denser (while still being slightly porous) and mirrors the dense films with small voids that will be discussed in Chapter 5; these regions are called *light* in this chapter. The nanostructure of the film shifts from dark to light regions sharply, over the course of several hundred nanometers (Figure 4-1). In both kinds of regions, the film is not a monolayer; instead, multiple layers of deposits are visible using a SEM.

4.4. Film Adhesion Dependence via a DOE of Nanoscratch Tests

In the absence of a strong gas flow, the microsputtered gold film adheres poorly to both silicon (with a thin native oxide) and silicon dioxide [4:8]. However, in the presence of a strong gas flow (> 4 slm), the film adhesion drastically improves for both substrates. Moreover, the high-flow films pass the tape test (ASTM D3359) [4:9].

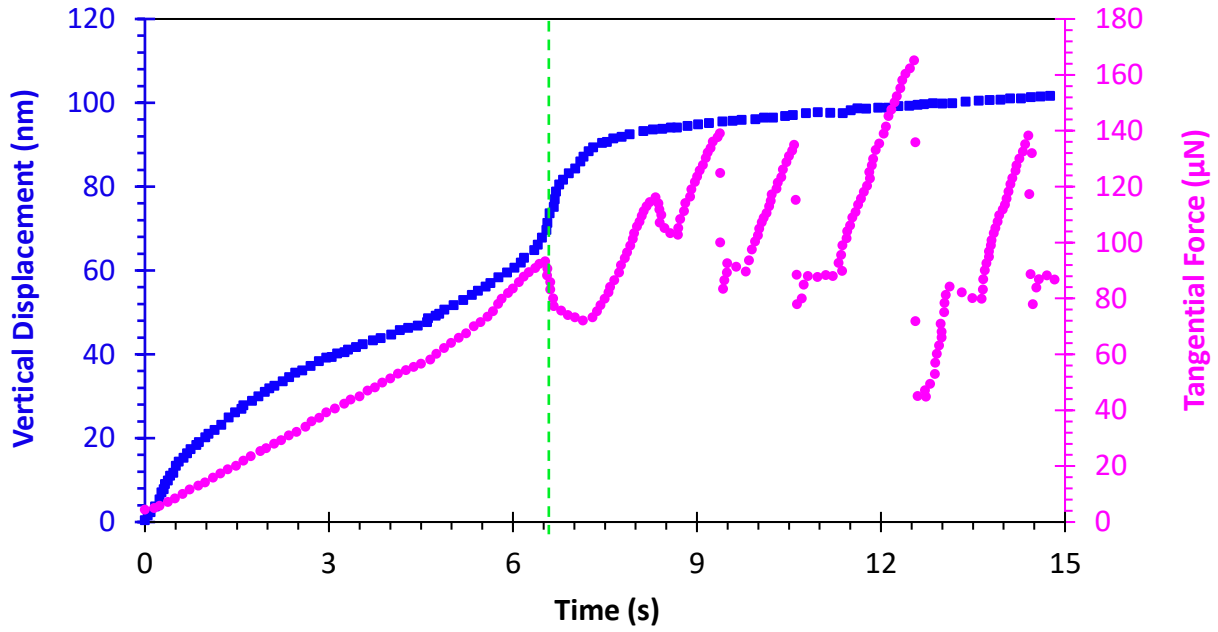

Figure 4-2. Lateral force and vertical displacement versus time during one of the nanoscratch tests. The normal force increases over time, causing the probe to dig deeper into the film, increasing the vertical displacement, and also increasing the lateral force. Eventually, the lateral force surpasses the film adhesion strength, causing its delamination. The film delamination can be seen in the data plot as a sudden and drastic drop in the lateral force applied to the film, in parallel to a sudden increase of the vertical displacement. The time at which film delamination takes place in the data plot (6.53 s) is indicated with a dotted green line; the normal force at that point (438 µN for the data set; not shown) is used as our figure of merit to indirectly characterize the adhesion strength of the film.

Using a Hystiron TI 950 TriboIntenter, a series of nanoscratch tests part of a design of experiments (DOE) was conducted to quantitatively characterize the film adhesion to the substrate and to

explore the functional dependence of the control parameters. A nanoscratch test, described in [4:10], uses a 1-μm diameter diamond conospherical tip to slowly scratch the film. As the normal force increases, pushing the tip deeper into the film, the tangential force applied by the tip to the film also increases. Eventually, the tangential force becomes large enough to tear the film off the substrate (Figure 4-2); this force can be related to the adhesion strength using a variety of equations [4:10]-[4:12]. Consequently, measuring the normal force at the point of film delamination is a direct quantitative measure of the film adhesion strength.

Parameter	Minimum Value	Maximum Value
p_o (Outer inlet pressure)	2 kPa	14 kPa
$p_i - p_o$ (Difference between inner and outer inlet pressures)	7 kPa	28 kPa
Target-to-substrate distance	2.5 mm	4.4 mm
Anode-to-target distance	1 mm	5 mm
Substrate bias voltage	-300 V	0
Plasma bias voltage	660 V	1450 V
Substrate current	220 nA	5.2 μA

Table 4-1. Parameters used and varied in the DOE to explore film adhesion. Note that the first five parameters were controlled directly, while the last two were recorded and effected by the other parameters, but not controlled.

Parameter	Effect	σ	p-value
v_o (mean velocity in outer tube)	-3.10 μN-s/m	1.07 μN-s/m	0.0115
Plasma bias voltage	0.427 μN/V	0.105 μN/V	0.00241

Table 4-2. Reduced-order model for the light region part of a static deposit. The p-value is found from Student's t-test. It is not adjusted for the variables that were excluded from this reduced order model. The quantitative method of adjusting is somewhat disputable; instead, we show using a quantile-quantile chart (Figure 4-3), that the p-values of the ensemble of models must be, as a whole significant. Regardless, even for the most conservative adjustments, these parameters are clearly significant, with $p<0.05$.

Parameter	Effect	σ	p-value
v_i (velocity in inner tube)	-4.05 μN-s/m	1.415 μN-s/m	0.0104

Table 4-3. Reduced-order model for the dark region part of a static deposit. The p-value is unadjusted; Figure 4-3 shows the clear significance of the inner gas flow's velocity in the ensemble of models.

To accommodate the possibility of a different functional dependence of the film adhesion on the control parameters for light and dark films, the DOE statistical analysis treated each region independently. The process parameters varied in the DOE are the inner and outer gas flows, the substrate-target distance, the anode-target distance, and the negative substrate bias voltage. The plasma voltage and the current collected by the substrate were not directly controlled but were recorded. All depositions ran for five minutes at 2 mA plasma current while keeping static the printhead.

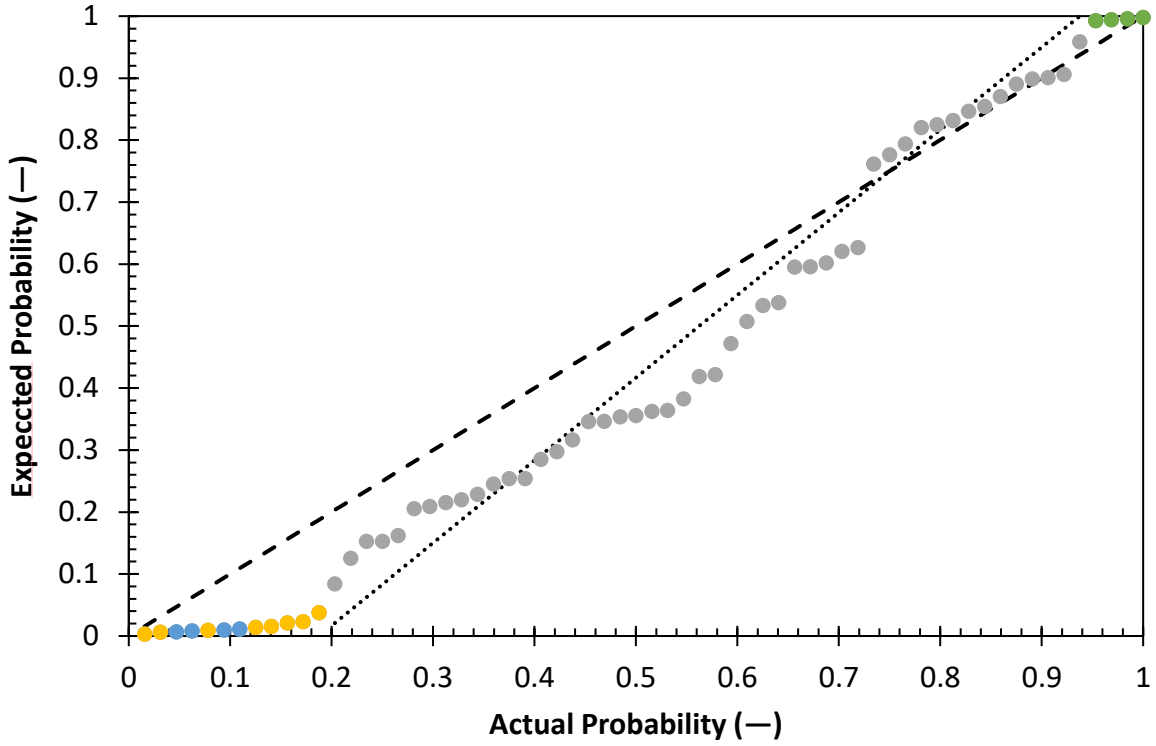

Figure 4-3. A q-q plot of various process parameters for the ensemble of reduced models for both sets of samples (dark, light). Most process parameters follow the distribution that would be expected from random data (dashed line); only the dots representing the inner gas flow for the dark region samples (orange), the outer flow (blue) and the plasma bias voltage (green) for the light region samples diverge from the dashed line. For the light region samples, only the four reduced models that include both substrate bias voltage and outer flow are colored; only with both parameters included the noise is reduced enough for the effect to be statistically significant. The dotted line represents the expected distribution for the remaining parameters that have no effect on the adhesion; as expected, the grey dots follow that distribution.

As described in Chapter 2, the gas flow fed to the plasma microreactor is controlled by varying the inlet pressure. The DOE varies the difference between the inner and outer inlet pressure, rather than the inner pressure alone to reflect the hypothesis that the relative velocities of the inner and outer gas flows govern the streamlines of the flow and the path of the sputtered material. Consequently, cases in which the inner and outer gas flows have either similar velocities or in which the inner flow is much stronger were considered in the DOE.

The dynamic range of the parameters used in the DOE and a reduced model, including p-values, for both the dark and light regions are given in Tables 4-1 through 4-3. A quantile-quantile plot is also produced, graphically showing the clear statistical significance of the models, despite the simultaneous testing of multiple hypotheses (Figure 4-3).

The q-q plot is a graphical method to determine if the apparent significance of one parameter is real or merely due to the vast multitude of hypotheses tested [4:13]. It arranges the parameters from all possible reduced models in order of significance, and plots the p-value, the chance that a random set of data could produce an effect of this significance, against a straight line. If the p-values approximately follow the straight line, it is reasonable to claim that there is no truly significant parameter, and the only reason some parameters appear to be significant is because the ensemble of reduced models includes so many possible parameters, that some will, by chance, appear to be significant. However, if the p-values do not follow a straight line, but instead several models are bunched, either under the line with very low p-values, or above the line with very large p-values, it is presumed that a given parameter (or parameters) are significant in several possible reduced models, and thus their effect cannot easily be attributed to chance. In this case, the reduced models are clearly significant.

The DOE has thus served its purpose; it has identified which parameters significantly impact the adhesion of the films, and the directions and rough magnitudes of those effects. Were we attempting to optimize the adhesion, it would be prudent to investigate these effects by testing the adhesion at several different gas flows, to find the ideal gas flow empirically. However, rather than merely conduct empirical studies, we instead take the found dependencies and use them to suggest a theory.

Based on the results of the DOE, the dark regions are strongly influenced by the inner gas flow (i.e., the sum of the outer flow and the difference between the outer and inner flow); a stronger gas flow is deleterious to the adhesion. Similarly, the light regions are strongly influenced by the outer gas flow (negatively affecting the film adhesion) and the plasma bias voltage (positively affecting film adhesion). Nonetheless, the experimental data from previous experiments in the low-flow regime suggest there is an optimal value for the gas flow rate: while gas flow that is too high is detrimental to film adhesion, low gas flow leads to even less adhesion.

The DOE also yields interesting insights regarding which process parameters do not affect the film adhesion. For example, if the improved adhesion were due to plasma cleaning of the substrate from contaminants [4:14], or the removal of the native oxide [4:8], film adhesion would heavily depend on the plasma current. Also, if the improved adhesion were due to substrate heating, the target-substrate distance would have significant influence in film adhesion. Moreover, if the gold were migrating into the silicon, forming a silicide, the adhesion improvement would not be visible when depositing gold on silicon dioxide. Conversely, if the plasma were modifying the oxide by breaking silicon-oxygen bonds, there would be minimal effect on silicon wafers. None of these is the case.

4.5. How Nanoparticles Affect the Adhesion of Gold Microsputtered Films

Based on the experimental results, it is hypothesized that the improved film adhesion, along with the actual formation of two deposition regions (dark and light), is due to the presence of nanoparticles formed in the plasma from the individual sputtered atoms. Furthermore, via

simulations and plasma theory, the role of gas flow on nanoparticle formation and film adhesion is elucidated.

The high-energy, high-density environment of an atmospheric plasma makes it likely for atoms to agglomerate into nanoparticles; this phenomenon has been observed and harnessed in the past [4:15]-[4:21]. However, not all atoms coalesce into nanoparticles, and not all nanoparticles are of equal size. When the mixture of nanoparticles of various sizes and individual atoms approaches the substrate, the fast jet stream (whether, as will be discussed later, the inner or the outer flow) that carries them acts like an impactor (i.e., a momentum-based particle sorter). Large nanoparticles, with high inertia, are minimally deflected and are thus adsorbed in a small region directly under the center of the jet stream, the dark region. In contrast, the smaller nanoparticles and lighter sputtered atoms are easily deflected and are only integrated into the film some distance from the center of the jet stream's impact, in the light region. Computational and experimental studies show this effect with fluid droplets [3:10]. The separation of large nanoparticles upon the impingement of a plasma onto a surface has been reported, with a slightly different explanation, in a study contemporaneous with our own [4:16]. A more comprehensive comparison of this thesis with this study will be discussed later in this chapter.

Consequently, two distinct deposition regimes appear. The inner region, directly under the jet stream, is primarily comprised of large nanoparticles (approximately 100 nm in diameter from SEMs). These nanoparticles are roughly of the same size, resulting in film packing with large voids. These voids, approximately the same size as the nanoparticles (100 nm), are optically dark. Even though the length scales of the porous nanostructure are 15%-30% that of light's wavelengths (300-700 nm), the films still absorb light, as has been reported with other gold films, due to the interactions between neighboring voids [4:23].The outer region, surrounding the inner region, is comprised of significantly smaller nanoparticles and individual atoms. These are smaller and more varied in size, and, as a result, they can arrange themselves into a denser, more continuous structure.

When a nanoparticle impacts the substrate, it deforms, increasing its contact area with the substrate [4:24]. This increased contact area, even with only Van der Walls forces acting and no chemical reaction, causes an adhesive force that resists delamination [4:25]. Given that the increased contact area is proportional to the original size of the nanoparticle and the deformation is related to the kinetic energy of the impinging particle, a large, energetic particle can form an adhesion layer between the gold and native oxide on the silicon, even without any other adhesion layers or chemical reactions. Specifically, the necessary force to delaminate nanoparticles scales as the cube of the contact radius [4:24]; in other words, nanoparticles, whether in the dark or light region, serve as anchors to prevent film delamination [4:26]. These nanoparticles, because of their small size and high impact energy, bond tightly to the substrate, despite the lack of chemical bonds. They act as an adhesion layer for the rest of the gold, as has been shown in a contemporaneous study [4:27]. Other particles and atoms that subsequently land can bond to these particles, which are then bound relatively tightly to the substrate. These effects apply equally to the dark region, with fewer but larger nanoparticles, and the light region, with more, smaller nanoparticles.

In order to rule out the possibility that the film adhesion is chemically enhanced, XPS measurements on the adhered films were conducted (Figure 4-4). The XPS detects the peaks of silicon, oxygen, and gold, but the characteristic 102 eV energy peak corresponding to gold silicide is missing [4:28], as is the 85.9 eV and 530 eV peaks that would suggest the presence of gold oxide [4:29]. Instead, the 100 eV peak for pure silicon and the 84 eV and 88 eV peaks for pure gold are present (See Table 4-4). Consequently, the XPS data show that the gold and substrate do not react chemically. Nonetheless the experimental data suggest that the physical interaction is sufficient to increase film adhesion.

Although the presence of the jet elongates the plasma, increasing the volume in which nanoparticles are produced, a fast jet flow also forces nanoparticles out of the plasma quickly (i.e., it reduces the residence time of the nanoparticle in the plasma). These opposite effects are each dominant in different flow regimes. The elongation of the plasma dominates at low flows. An increased flow enlarges the plasma, causing more nanoparticles to be created. However, once the flow is greater than approximately 4 m/s (determined by simulation), the plasma is at its largest volume. At that point, further gas flow is deleterious to nanoparticle production and adhesion because nanoparticles are pushed out of the plasma before they reach their maximum size. This dependence of nanoparticle size on gas flow has been reported in other studies [4:24].

For an electron to ionize an atom, as is crucial for a self-sustaining plasma process. The electron can strike the atom with sufficient energy to strip away an electron in its outer shell, in a single step. However, the electron can also strike the atom with enough energy to excite the atom, sending the electron bound to the atom to a higher energy state; the next electron to strike this excited atom needs less energy to ionize the atom [4:31]. Reported research has shown the dominance of the two-step process in high pressure (>2 Torr) plasmas [4:32]-[4:34].

To further understand these flow regimes, the elongation of the plasma was studied via theory and simulations. The elongation of the plasma is due to the gas flow pushing away excited, but not ionized, atoms. Since an excited atom has a lifespan of approximately 20 ns before it either falls to a lower energy state or is ionized [4:33], for the microplasma reactor studied in this thesis a gentle gas flow of 4 m/s pushes the excited atoms as much as 80 nm away before they could be ionized. This distance is approximately equal to the mean distance between collisions; the ion will collide, on average, once before it reaches the location where the original atom was before it was excited. Thus, if an atom is excited, it will be driven away from the cathode by the gas flow, and by the time it is ionized, it will be too far from the cathode to strike the cathode before collisions rob it of its charge. Thus, the only method to sustain the plasma is for electrons to directly ionize unexcited atoms; this requires a higher electron energy, and thus a stronger electric field and a longer plasma plume.

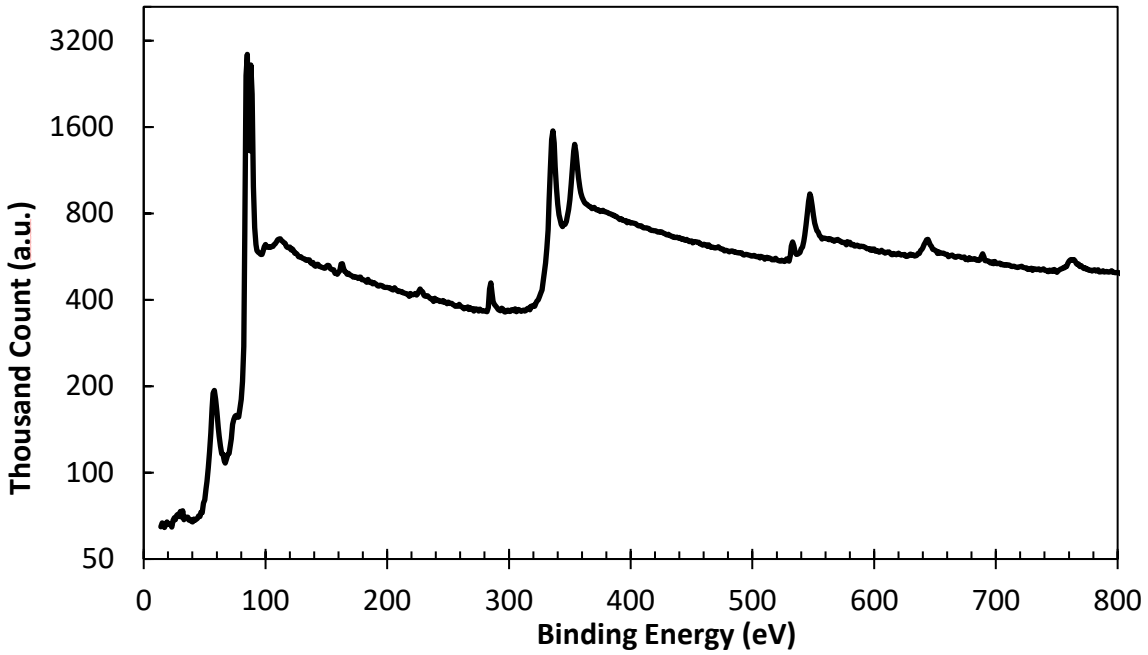

Figure 4-4. XPS data from a microsputtered gold film produced in the jet-assisted microsputtering regime. The peaks correspond to silicon, gold, and carbon contamination, but not to gold silicide or any oxide. Note the semilogarithmic scale.

Binding energy (eV)	Significance	Present?
763	Au 4s	YES
548	Au 4p3/2	YES
530	O in Au2O3	NO
355	Au 4d3/2 (353)	YES
336	Au 4d5/2	YES
285	C 1s	YES
155	SiO2 2s	NO
151	Si 2s	YES
103	SiO2 2p	NO
102	Si in Si/Au	NO
100	Si 2p	YES
88	Au 4f5/2	YES
86	Au in Au2O3	NO
84	Au 4f7/2	YES
58	Au 5p3/2	YES

Table 4-4. Binding energies detected and not detected in the XPS data shown in Figure 4-4. Note that the data is consistent with the presence of elemental silicon and gold, but no compounds including either substance. The binding energies are collected from the NIST database [29].

This was confirmed by simulations using COMSOL Multiphysics' Plasma Module to model a 1-D atmospheric pressure plasma (Figure 4-5). Because the model only uses one dimension, the simulation is not computationally expensive. Once a plasma is struck and stabilized, a gas flowing away from the anode is slowly introduced and accelerated at a rate of 13 km/s^2 (0 to 60 $m \cdot s^{-1}$ over the course of 4.5 ms). The rate of acceleration is shown, from other simulations, to be slow enough that we can treat the plasma as quasi-steady. As the gas flow increases in speed, the plasma plume becomes larger and the maximum electron energy increases, until, at 4 $m\ s^{-1}$, it increases no more (Figure 4-5). Similar trends, although given without explanation, are described in [4:35].

It is informative to compare the threshold speed of 4 $m \cdot s^{-1}$ to the drift velocity of the ions. Nitrogen molecules have an electrical mobility of approximately $1.85 \times 10^{-4}\ m^2\ V^{-1}\ s^{-1}$ [4:36], which means that, at the typical electric field near the anode of 3 $MV\ m^{-1}$, the ions have a drift velocity of 555 $m \cdot s^{-1}$—faster than any subsonic gas flow. Consequently, any gas field we introduce cannot have a meaningful effect on the ions.

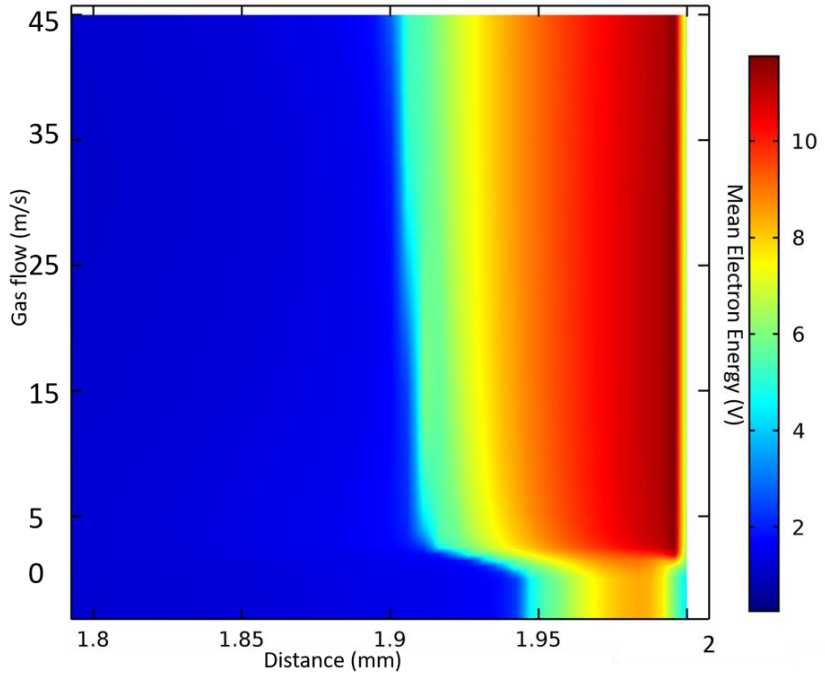

Figure 4-5. COMSOL simulation results of a plasma, as the gas flow is slowly increased. The parameter measured is the ion energy; any other plasma parameter gives similar results. Until the gas flow reaches 4 $m\ s^{-1}$, increased gas flow rate results in a larger plasma plume and a more energetic plasma; past that point, the increased gas flow has minimal effect in further increasing the plasma volume or its energy.

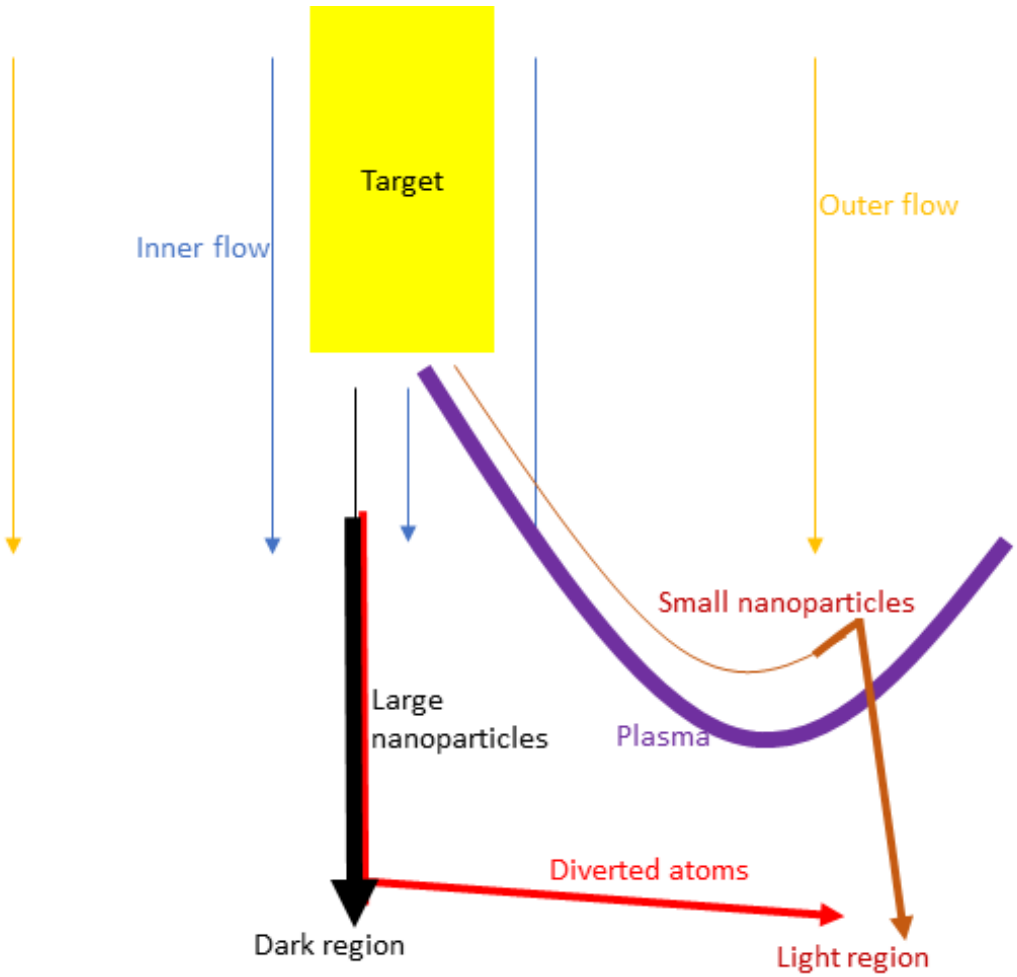

Figure 4-6. A schematic of the formation and transport of nanoparticles. The dark region is comprised of large nanoparticles, which form near the target and are carried by the inner flow to the dark region. The light region is comprised of both diverted atoms, which are formed near the target and diverted by the inner flow to the light region due to their low inertia, and small nanoparticles, which are formed in the plasma far from the target and carried by the outer flow. Thicker black, red, and brown lines represent nanoparticles after they are formed. The plasma pictured has a long path and is thus relatively large, allowing for more volume in which the small nanoparticles (brown) can form.

Thus, once the plasma reaches its maximum size, any further gas flow is deleterious to nanoparticle size and adhesion. This supports the results of the DOE study, in which a too-fast gas flow lead to lower adhesion. The dark region's adhesion, controlled by the largest nanoparticles formed near the target, is controlled by the inner gas flow, which runs near the target.

To understand the effect of the process parameters on the adhesion of the light regions, it is hypothesized that there are actually two volumes of nanoparticle formation. Some nanoparticles,

as previously described, are formed from atoms that agglomerate near the target wire and are pushed by the inner gas flow towards the substrate, where they spread out due to the fluid effects discussed in Chapter 3. These are responsible for the porous structures seen in the "dark" regions and affect the adhesion in the "dark" regions. Other nanoparticles are formed from atoms that are pushed towards the volume of the outer flow, where they form smaller nanoparticles in the plasma there [4:37], [4:38]. The process of nanoparticle formation is similar, but, because there is less sputtered material farther from the target wire, the nanoparticles are smaller [4:39]. These nanoparticles are then pushed towards the substrate by the outer flow (Figure 4-6).

Thus, by analogy, the light region's adhesion is controlled by nanoparticles formed slightly farther from the target, in the area whose convection is governed by the outer flow. A larger outer flow forces the nanoparticles from this outer volume into the light region before they grow, and thus the adhesion of the light region is negatively impacted.

The effect of the plasma voltage is similarly understood. A larger plasma bias voltage is due to the plasma taking a more circumlocutions path from the anode to the target wire; the larger the path, the more voltage is necessary to maintain the electric field that can sustain the plasma [4:40]. The path taken by the plasma is determined not only by many controllable factors, such as the gas flows, but also by uncontrollable factors, including the precise positioning of the target wire and the electrodes, the complex flow field of the air, and even some stochastic processes. Thus, while we cannot control the plasma's path directly, we can measure it indirectly through the voltage. This uncontrollable plasma size, no matter its cause, directly impacts nanoparticle formation near the outer flow. The larger the plasma, the larger the volume in which nanoparticles can grow.

The results reported in this section are in agreement with an excellent experimental paper exploring nanoparticle formation in atmospheric pressure, published a few weeks after our study was published. In [4:16], researchers struck a microplasma to sputter copper in a nitrogen atmosphere; a strong gas flow carried the formed nanoparticles to a nearby substrate, which included a very precise quartz balance, allowing the study of the sputtered mass flow rate. They varied the gas flow (100-10,000 sccm) and power (2.5-10 W). For comparison, we worked at gas flows of 1,000-24,000 sccm and power of 1.5-3 W. They found that there was a medium flow rate (~1 $m\ s^{-1}$) at which the film was porous; at higher and lower flow rates, the film was dense. They also found that the medium flow rate also led to the fastest film depositions (4 ng/J). They noted explicitly that the nanoparticles shrink in size as the gas flow increases, in agreement with our analysis. However, while the researchers of [4:16] surmise that the decreased porosity at high flow rates might be due to the decreased flow rate, according to our analysis, it would be due to the smaller nanoparticles. Specifically, according to our theory, the middle gas flow represents ideal conditions to produce large nanoparticles, leading to high porosity and improved transport properties. Larger gas flow rushes the nanoparticles out of the plasma before the nanoparticles are large. They, like we, they find that the majority of the charged sputtered material reaches the substrate, and they measure the current that reaches the substrate as several nA; we measure the substrate current as two orders of magnitude higher, due to differences in experimental setup. Their

study is an important experimental confirmation of our hypothesis and supports our observations, namely, that a medium flow is ideal for the formation of large nanoparticles and porous films, and shows that perhaps our conclusions can be extended to other sputtered metals.

4.6. High-Adhesion Gold Films via Layering of Large and Small Nanoparticles

Our research indicates that to improve film adhesion, nanoparticle production within the microplasma must be stimulated. Unfortunately, the presence of nanoparticles also causes the unwanted central porous region. However, the positive effects of nanoparticle formation can be harnessed, while avoiding the negative effects, by alternating the deposition of large nanoparticles with the deposition of smaller nanoparticle and atoms in a given spot. This can be readily accomplished by rastering the printhead. As long as the printhead moves sufficiently quickly (>10 $\mu m\ s^{-1}$), the spot under the printhead that collects large nanoparticles moves before a porous structure forms. Instead, a monolayer, or part of a monolayer, of large nanoparticles are deposited, followed by a collection of small nanoparticles and atoms that fill in the gaps. As long as the layer deposited in a single pass is less than or equal to a monolayer, large nanoparticles do not overshadow empty spaces, and voids do not form. When the printhead returns to the same spot, more large nanoparticles are deposited on top of the filled in layer, with the small nanoparticles and atoms acting as the mortar to fill in the gaps between the large nanoparticles. This leads to a dense film, shown both optically and microscopically (Figure 4-7). Additionally, this dense film is highly conductive (see Section 5.6).

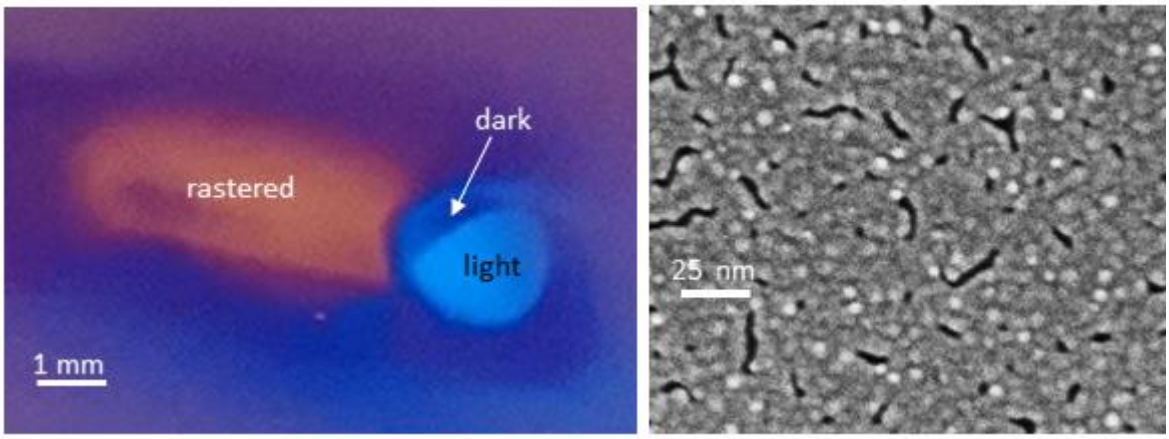

Figure 4-7. Photograph (left) and SEM micrograph (right) of a gold microsputtered deposit produced by rastering the printhead; the deposits attain high film adhesion and excellent electrical conductivity by packing dissimilar nanoparticles (large nanoparticles acting as anchor of the film, smaller nanoparticles filling-in the gaps between large nanoparticles). A dark spot and light spot, produced by not rastering the printhead, are visible at one of the ends of the rastered zone and is shown for comparison. The light region is dense, but is a pale blue due to its thinness; the dark region is porous and thus absorbs light. The rastered deposit is thick and dense, and is thus gold colored.

4.7. Conclusion

This chapter described the effects of nanoparticles on the adhesion of gold film. With proper plasma conditions, nanoparticles form in the high-density, high-energy environment of the plasma; maximization of the plasma plume volume while minimizing gas flow rate causes the nanoparticles to form optimally. Large nanoparticles deposit directly under the target wire due to their inertia, providing excellent adhesion but large porosity; in contrast, smaller particles deposit around the large nanoparticles due to hydrodynamic deflection. By rastering the printhead, films with excellent adhesion and electrical conductivity can be printed; the theory presented in this chapter is in agreement with recently published experimental work on microplasma sputtered copper films.

4.8. References

[4:1] Kornbluth Y, Mathews R, Parameswaran L, Racz LM, Velásquez-García LF. Nano-additively manufactured gold thin films with high adhesion and near-bulk electrical resistivity via jet-assisted, nanoparticle-dominated, room-temperature microsputtering. Additive Manufacturing. 2020 Dec 1;36:101679.

[4:2] Ohring M. *Materials Science of Thin Films*. Elsevier; 2001 Oct 20.

[4:3] Cai F, Gao Y, Fang W, Mao T, Zhang S, Wang Q. Improved adhesion and cutting performance of AlTiSiN coatings by tuning substrate bias voltage combined with Ar ion cleaning pre-treatment. Ceramics International. 2018 Oct 15;44(15):18894-902.

[4:4] Hoogvliet JC, Van Bennekom WP. Gold thin-film electrodes: an EQCM study of the influence of chromium and titanium adhesion layers on the response. Electrochimica Acta. 2001 Nov 1;47(4):599-611.

[4:5] Hegemann D, Brunner H, Oehr C. Plasma treatment of polymers for surface and adhesion improvement. Nuclear Instruments and Methods in Physics Research Section B: Beam Interactions with Materials and Atoms. 2003 Aug 1;208:281-6.

[4:6] Cłapa M, Batory D. Improving adhesion and wear resistance of carbon coatings using Ti: C gradient layers. Journal of Achievements in Materials and Manufacturing Engineering. 2007 Jan;20(1-2):415-8.

[4:7] Egitto FD, Matienzo LJ. Plasma modification of polymer surfaces for adhesion improvement. IBM Journal of Research and Development. 1994 Jul;38(4):423-39.

[4:8] Dallaporta H, Cros A. Influence of low-energy electron irradiation on the adhesion of gold films on a silicon substrate. Applied Physics Letters. 1986 May 19;48(20):1357-9.

[4:9] Valli J. A review of adhesion test methods for thin hard coatings. Journal of Vacuum Science & Technology A: Vacuum, Surfaces, and Films. 1986 Nov;4(6):3007-14.

[4:10] Beake BD, Harris AJ, Liskiewicz TW. Review of recent progress in nanoscratch testing. Tribology-Materials, Surfaces & Interfaces. 2013 Jun 1;7(2):87-96.

[4:11] Steinmann PA, Hintermann HE. A review of the mechanical tests for assessment of thin-film adhesion. Journal of Vacuum Science & Technology A: Vacuum, Surfaces, and Films. 1989 May;7(3):2267-72.
[4:12] Chang SY, Huang YC. Analyses of interface adhesion between porous SiO2 low-k film and SiC/SiN layers by nanoindentation and nanoscratch tests. Microelectronic Engineering. 2007 Feb 1;84(2):319-27.
[4:13] Schweder T, Spjøtvoll E. Plots of p-values to evaluate many tests simultaneously. Biometrika. 1982 Dec 1;69(3):493-502.
[4:14] Ohmi T, Ichikawa T, Shibata T, Matsudo K, Iwabuchi H. In-situ substrate-surface cleaning for very low temperature silicon epitaxy by low-kinetic-energy particle bombardment. Applied Physics Letters. 1988 Jul 4;53(1):45-7.
[4:15] Rao N, Girshick S, Heberlein J, McMurry P, Jones S, Hansen D, Micheel B. Nanoparticle formation using a plasma expansion process. Plasma Chemistry and Plasma Processing. 1995 Dec;15(4):581-606.
[4:16] Schlag L, Isaac NA, Nahrstedt H, Reiprich J, Ispas A, Stauden T, Pezoldt J, Bund A, Jacobs HO. Nanoparticle gas phase electrodeposition: Fundamentals, fluid dynamics, and deposition kinetics. Journal of Aerosol Science. 2021 Jan;151:105652.
[4:17] Bica I. Nanoparticle production by plasma. Materials Science and Engineering: B. 1999 Dec 20;68(1):5-9.
[4:18] Vons V, Creyghton Y, Schmidt-Ott A. Nanoparticle production using atmospheric pressure cold plasma. Journal of Nanoparticle Research. 2006 Oct;8(5):721-8.
[4:19] Jerby E, Golts A, Shamir Y, Wonde S, Mitchell JB, LeGarrec JL, Narayanan T, Sztucki M, Ashkenazi D, Barkay Z, Eliaz N. Nanoparticle plasma ejected directly from solid copper by localized microwaves. Applied Physics Letters. 2009 Nov 9;95(19):191501.
[4:20] Sylvestre JP, Kabashin AV, Sacher E, Meunier M. Femtosecond laser ablation of gold in water: influence of the laser-produced plasma on the nanoparticle size distribution. Applied Physics A. 2005 Feb;80(4):753-8.
[4:21] Chen X, Ghosh S, Buckley DT, Sankaran RM, Hogan Jr CJ. Characterization of the state of nanoparticle aggregation in non-equilibrium plasma synthesis systems. Journal of Physics D: Applied Physics. 2018 Jul 26;51(33):335203.
[4:22] Feng JQ. A Computational Study of Particle Deposition Patterns from a Circular Laminar Jet. Journal of Applied Fluid Mechanics. 2017;10(4):1001-12.
[4:23] Ng C, Yap LW, Roberts A, Cheng W, Gómez DE. Black gold: broadband, high absorption of visible light for photochemical systems. Advanced Functional Materials. 2017 Jan;27(2):1604080.
[4:24] Carrillo JM, Raphael E, Dobrynin AV. Adhesion of Nanoparticles. Langmuir. 2010 Aug 3;26(15):12973-9.
[4:25] Joo S, Baldwin DF. Adhesion mechanisms of nanoparticle silver to substrate materials: identification. Nanotechnology. 2009 Dec 21;21(5):055204.

[4:26] Böhme G, Hohn P, Krupp H, Rabenhorst H, Schnabel W, Walter G. Adhesion of gold particles to silicon and gold substrates in ultrahigh vacuum. Journal of Applied Physics. 1973 Sep;44(9):3914-8.
[4:27] Zheng M, Yang Y, Liu P, Duan H, Keathley PD, Berggren KK. Fabrication of gold nanostructures using wet lift-off without adhesion promotion. Microelectronic Engineering. 2020 Sep 15;233:111420.
[4:28] Sundaravel B, Sekar K, Kuri G, Satyam PV, Dev BN, Bera S, Narasimhan SV, Chakraborty P, Caccavale F. XPS and SIMS analysis of gold silicide grown on a bromine passivated Si (111) substrate. Applied Surface Science. 1999 Jan 1;137(1-4):103-12.
[4:29] Pireaux JJ, Chtaïb M, Delrue JP, Thiry PA, Liehr M, Caudano R. Electron spectroscopic characterization of oxygen adsorption on gold surfaces: I. Substrate impurity effects on molecular oxygen adsorption in ultra high vacuum. Surface Science. 1984 Jun 1;141(1):211-20.
[4:30] NIST X-ray Photoelectron Spectroscopy Database, NIST Standard Reference Database Number 20, National Institute of Standards and Technology, Gaithersburg MD, 20899 (2000), doi:10.18434/T4T88K, (retrieved 3/4/2021).
[4:31] Hyman HA. Electron-impact ionization cross sections for excited states of the rare gases (Ne, Ar, Kr, Xe), cadmium, and mercury. Physical Review A. 1979 Sep 1;20(3):855.
[4:32] Adams SF, Bogdanov EA, Demidov VI, Koepke ME, Kudryavtsev AA, Williamson JM. Metastable atom and electron density diagnostic in the initial stage of a pulsed discharge in Ar and other rare gases by emission spectroscopy. Physics of Plasmas. 2012 Feb 23;19(2):023510.
[4:33] Bogaerts A, Gijbels R. Modeling of metastable argon atoms in a direct-current glow discharge. Physical Review A. 1995 Nov 1;52(5):3743.
[4:34] Ferreira CM, Loureiro J, Ricard A. Populations in the metastable and the resonance levels of argon and stepwise ionization effects in a low-pressure argon positive column. Journal of Applied Physics. 1985 Jan 1;57(1):82-90.
[4:35] Li Q, Li JT, Zhu WC, Zhu XM, Pu YK. Effects of gas flow rate on the length of atmospheric pressure nonequilibrium plasma jets. Applied Physics Letters. 2009 Oct 5;95(14):141502.
[4:36] Shumate C, Louis RS, Hill Jr HH. Table of reduced mobility values from ambient pressure ion mobility spectrometry. Journal of Chromatography A. 1986 Jan 1;373:141-73.
[4:37] Rao N, Girshick S, Heberlein J, McMurry P, Jones S, Hansen D, Micheel B. Nanoparticle formation using a plasma expansion process. Plasma Chemistry and Plasma Processing. 1995 Dec;15(4):581-606.
[4:38] Lescoute E, Hallo L, Hébert D, Chimier B, Etchessahar B, Tikhonchuk VT, Chevalier JM, Combis P. Experimental observations and modeling of nanoparticle formation in laser-produced expanding plasma. Physics of Plasmas. 2008 Jun 20;15(6):063507.

[4:39] Hinz A, Von Wahl E, Faupel F, Strunskus T, Kersten H. Nanoparticle forming reactive plasmas: a multidiagnostic approach. The European Physical Journal D. 2018 May;72(5):1-9.
[4:40] Chapman BN. *Glow Discharge Processes: Sputtering and Plasma Etching*. Wiley; 1980.

Chapter 5 – Electrical Conductivity of Microsputtered Gold Thin Films

5.1. Introduction

The goal of atmospheric-pressure microsputtering is to produce thin films that are adequate to fabricate electrical components without involving a semiconductor cleanroom. Thus, it is essential that the films produced by the manufacturing technique act as their constituent materials do, e.g., microsputtering electrically conductive materials must produce electrically conductive films. However, the electrical properties of thin films depend not only on the materials that they are made of, but also on their structure. This chapter describes how by controlling the magnitude of the electrical fields, the film density and electrical conductivity of microsputtered gold films can be optimized without resorting to any of the post-processing methods employed with traditional sputtering, e.g. thermal annealing. These results were published in 2019 in the journal *Nanotechnology* [5:1].

Specifically, this chapter first describes how the presence of many small, separate grains detracts from the deposited film's electrical conductivity, reviews traditional methods of avoiding such a grain structure, and explains why these methods are incompatible with our thermal budget and atmospheric pressure operation. Then, the chapter presents a statistical study of the process parameters that affect film density and proposes a physical explanation of the influence of substrate bias, gas flow, and plasma voltage in such property. After that, the chapter shows that the chosen method to densify the films, i.e., substrate bias, imparts a similar energy to the impinging atoms as compared to traditional methods, pointing out disadvantages of using overly energetic atoms. Finally, the chapter describes the role of nanoparticles on film electrical conductivity, while reporting a rough model for the relationship between film density and electrical conductivity and comparing of our best results, i.e., thin gold films with 120% bulk electrical resistivity, to the state of the art in printable interconnects.

5.2. Background

Under ideal circumstances, sputtered material would land on the substrate and arrange itself into a single, dense film with the electrical properties of the target. However, two phenomena prevent this from happening, i.e., crystal structure of the sputtered film and the formation of voids. Any film that is deposited without extremely high energy will form an amorphous or polycrystalline film; where crystals meet, a mismatch in crystal structures will result in the creation of a small gap. Although that crystal mismatch can impact a semiconductor's performance, it is not, generally speaking, not deleterious to a metallic film's electrical conductivity.

More insidious is the formation of voids. If a film forms through Volmer-Weber (island) growth, individual atoms will nucleate larger regions of growth, each several nm thick [5:2]. As these regions expand towards each other, a chasm, several nm thick and several nm wide, will form between two mutually approaching regions. The deposited particles on either side of the

chasm prevent incoming particles from filling-in the chasm. Instead, the newly-arriving particles stick to the deposits on either side of the chasm. This produces grains that grow vertically, with narrow chasms remaining between adjacent grains. Shadowing effects prevent impinging particles, often arriving at an angle, from navigating the narrow chasm. Consequently, they join the top of an existing grain. Even as the deposit grows, the chasm remains, leading to a porous nanostructure with high electrical resistivity [5:3]. This chasm, a gap several nm wide, is wide enough to prevent charge from crossing the chasm, and, if there are enough of these chasms, their presence can cause a high level of electrical resistance.

In the case of vacuum sputtering, these chasms are small or nonexistent. This is due to the directionality of the sputtered material; the sputtered material flies ballistically towards the substrate, without collisions to redirect its direction. Thus, all particles arriving at a particular location will have similar angles of approach, and thus can navigate between the chasm walls, parallel to the angle of arrival, and thus shrink the chasms' width. This process can be used to deposit columnar microstructures, either at oblique or right angles, in order to create films with variable light transmissivity [5:4].

The vertical growth of grains, with narrow chasms between them, is well described by Thornton's zone model, first introduced in the 1980s [5:5]. The model identifies two central parameters that control the density of the film, i.e., background pressure and temperature. The first one, higher pressure, increases the number of collisions that a sputtered atom will undergo as it travels from the target to the substrate. Collisions rob the sputtered atom of its initial momentum, thermalizing it and diverting it from its original direction of motion, normal to the target (and often, substrate) surface. The increased chance of an oblique angle of motion makes it more likely that the atom will strike an existing grain, rather than navigating a narrow chasm. The second, and more relevant, parameter is the temperature of the substrate. Higher temperatures (i.e., 30-50% of the sputtered metal's melting temperature, or 128-395 °C for gold) impart thermal energy to the arriving atoms, allowing them to move into energetically favorable positions between grains and to rearrange the grain boundaries, leading to dense, monocrystalline films. Industrial sputterers take advantage of this zone model and use high temperatures and high vacuum [5:6]. Unfortunately, this solution is not viable for the purpose of creating high-quality thin films at atmospheric pressure and with a 100 °C thermal budget.

5.3. Design of Experiments

To find an alternative to the process suggested by Thorton's zone model, the effects of process parameters on the film density are methodically investigated using a design of experiments (DOE), with the goal of finding process parameters that produce highly electrically conductive and dense films. The DOE varied the target-substrate gap, anode-target gap, inner flow, outer flow, and negative focus voltage (Table 5-1). Both mass flow controllers (MFCs) control the flow of argon through their respective tubes; a large argon flow rate is important to maintain a practical plasma bias voltage. Specifically, higher argon content leads to a lower plasma voltage, which prevents wire overheating, while lower argon content leads to a higher voltage, increasing the ion energy and deposition rate. More details on this relationship can be found in Chapter 6.

Parameter	Minimum Value	Maximum Value
Printhead-Substrate Gap (μm)	380	635
Focus/Substrate Bias (V)	-300	0
Inner Gas Flow (sccm)	5	25
Outer Gas Flow (sccm)	28	139
Plasma Voltage	770	970

Table 5-1. Parameters varied in the DoE along with their minimum and maximum values. In the cases where the conductive stage was biased, it was done at the same bias voltage as that of the focus electrodes—this allowed the use of the same power supply.

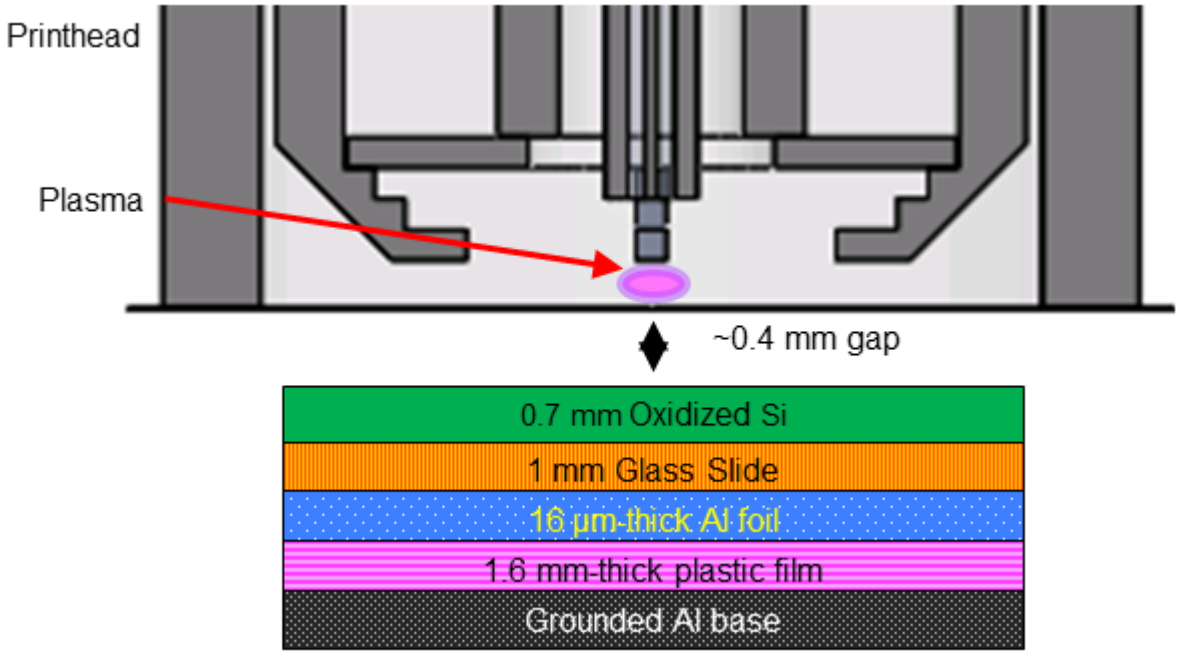

Figure 5-1. A schematic of the electrically biased plate under the substrate; the plate is charged, but the impinging ions cannot transmit charge through the air gap and glass plates. In later versions of the device, the substrate is directly charged.

In these experiments, a conductive plate beneath the substrate, electrically isolated from the substrate by two glass slides (VWR glass microscope slides, 1 mm thickness) was used (Figure 5-1). The plate can either be left floating (i.e., electrically isolated) or connected to the negative focus bias voltage; this was also varied as a process parameter. As a result of the varying process parameters, the plasma voltage changes; this is recorded, but is not controlled independently. The printer is run with a given set of process parameters for 10 minutes at 1 mA, using a 50 μm-diameter gold wire as target.

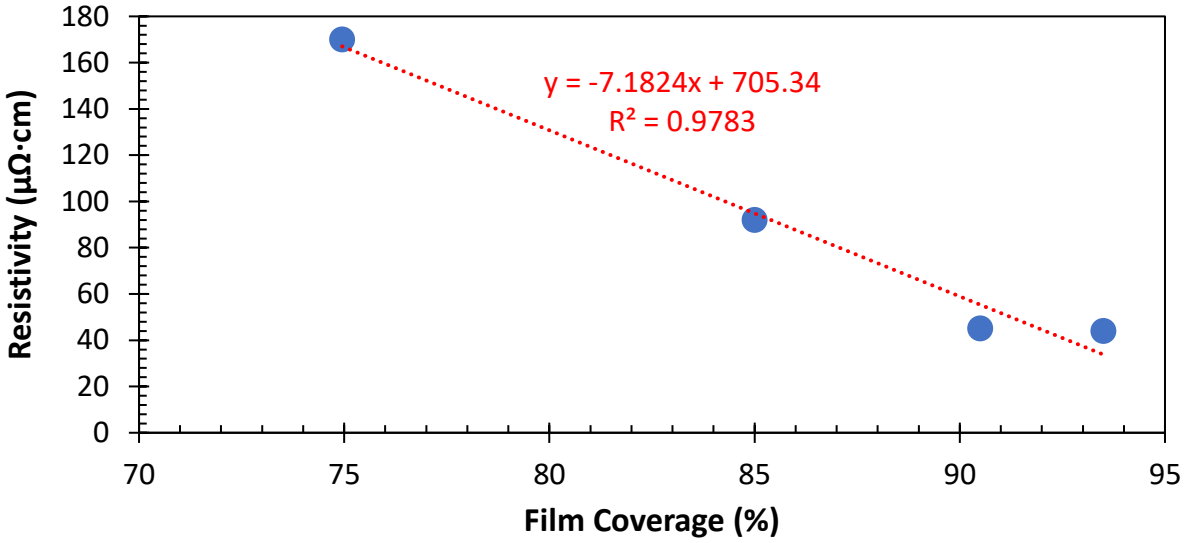

Figure 5-2. A graph of the electrical resistivity and calculated film coverage for several samples, showing a clear and strong correlation.

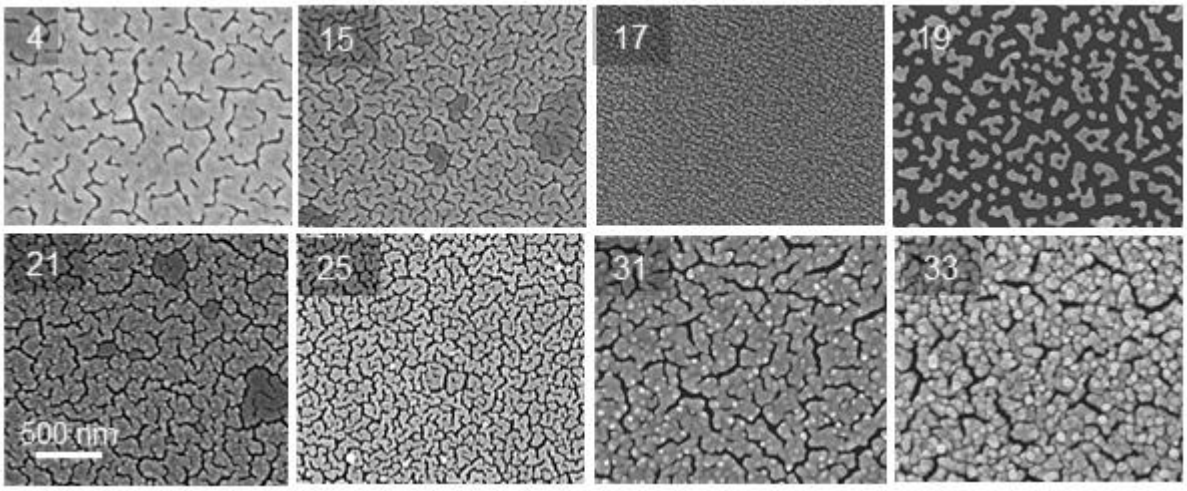

Figure 5-3. SEM micrograph of a variety of samples, with visible chasms between deposits. In some deposits (e.g., 15) the SEM charges electrically isolated portions of the deposit, imparting them with a darker color, while leaving the electrically conductive majority relatively light in color. Some samples (e.g., 19) present as isolated droplets, rather than deposits with narrow chasms; these will be discussed later in the text.

Using image processing, we determined the film coverage for each sample and used it as a measure of the electrical resistivity of the thin film. This dependence was confirmed experimentally, i.e., the data show a strong correlation between the fraction of the area coated with a film and the electrical resistivity of the microsputtered film (Figure 5-2). Clearly, the voids, visible to the microscope, drastically increase the electrical resistivity. A theoretical treatment of the relationship between coverage and resistance is provided in Section 5.7.

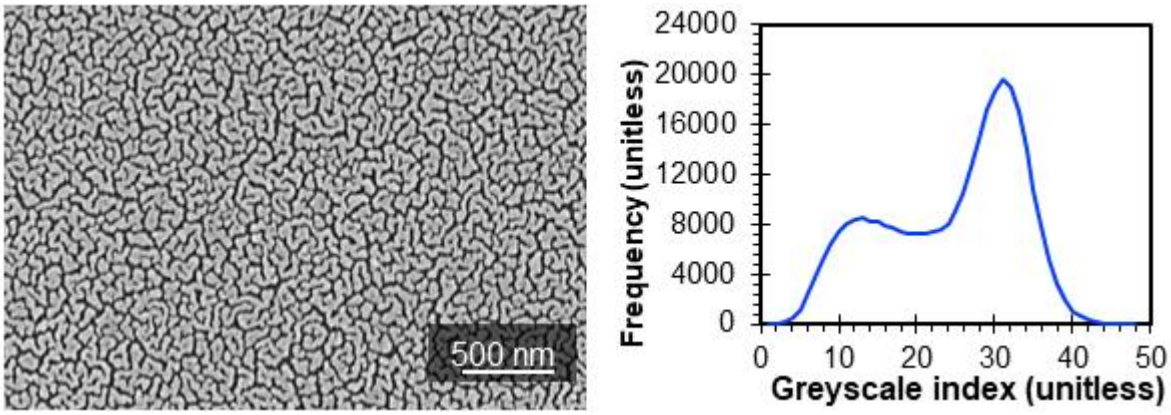

Figure 5-4. Color histogram of a typical deposit. The values represent the shade of greyscale, from 0 (black) to 255 (white). Two curves are clearly added together; the first, with low numbers, representing the bare silicon, which is not imaged by the SEM due to the limited depth of focus, and the second, with high numbers, representing the gold film. The relative size of the curves is used to determine the coverage percentage of the films.

SEM images (Zeiss 1525 SEM) were taken of each deposit (Figure 5-3); each image consists of a mixture of light (gold deposit) and dark (silicon chasm) pixels. Using image processing software (Wolfram Mathematica), the frequency of each shade of grey is logged and then automatically fit to a sum of two Gaussian curves (Figure 5-4). The relative area under each curve represents the fraction of the deposit that is covered (light, high number) with gold or remains a chasm (dark, low number). The fraction of the deposit that is covered with gold was used as the output measurement for our DOE methodology. This approach, fitting the pixel distribution to a sum of Gaussian curves, is more accurate than one that naively uses a simple cut-off point. Because the two Gaussian curves overlap, no single cut-off can accurately discriminate between the two regions. However, by measuring the relative size of the curves, we can still determine the coverage of a deposit. The coverage is determined to range from 34 to 96.5% (Table 5-2). Samples with less than 50% coverage are shown to consist primarily of isolated droplets, rather than meandering films with chasms. Because their coverage is not governed by the aforementioned principles (i.e., chasms between coalescing droplets), we exclude them from our statistical analysis. They will be discussed later in this chapter.

The results are reported below (Table 5-2), with a linear regression of our suggested model (Tables 5-3, 5-4) also reported. Applying a bias voltage to the plate under the substrate clearly has a very strong effect; to better measure other effects, we separate the data into two groups, i.e., those with a biased plate and those with a floating plate.

A quantile-quantile plot is also produced, graphically showing the clear statistical significance of our suggested models, despite the simultaneous testing of multiple hypotheses [5:7] (Figures 5-5, 5-6). It is clear that in the case of the biased plate, a stronger negative bias on the plate under the substrate greatly improves the substrate coverage. In the case of the floating plate,

Sample #	Foil floating / charged	Printhead-to-substrate gap (μm)	Focus voltage (also Foil voltage when biased) (V)	Inner flow rate (sccm)	Outer flow rate (sccm)	Anode voltage (V)	Film coverage (%)
1	Floating	635	100	25	139	970	51.1
2	Charged	760	300	15	139	850	87.7
3	Floating	635	300	25	139	690	62
4	Charged	255	100	15	28	796	85.6
5	Charged	635	100	15	83	800	88.9
6	Charged	510	100	25	42	830	79.4
7	Charged	510	300	15	42	810	95.4
8	Floating	380	300	5	42	830	77.0
9	Charged	380	300	5	56	840	85.1
10	Floating	380	300	25	56	850	81.6
11	Floating	380	100	15	70	860	79.8
12	Floating	510	100	5	70	790	75.4
13	Floating	380	100	5	111	765	49.3
14	Floating	380	300	15	111	770	87.4
15	Charged	380	300	5	111	910	52.1
16	Charged	510	300	25	111	910	93.3
17	Charged	510	100	15	111	900	74.9
18	Charged	510	100	25	139	920	69.9
19	Charged	510	300	15	83	980	82.8
20	Floating	380	0	5	83	800	90.4
21	Floating	380	300	5	83	790	93.5
22	Floating	510	0	15	111	910	65.9
23	Floating	510	100	15	139	970	89.3
24	Floating	510	100	25	28	940	45.3
25	Charged	510	0	15	56	850	63.0
26	Charged	510	0	15	83	970	78.1
27	Charged	255	0	15	61	910	56.0
28	Charged	635	0	15	56	880	74.3
29	Charged	760	300	15	83	820	44.0
30	Charged	760	300	15	83	770	34.0
31	Charged	760	300	15	83	780	90.0
32	Charged	760	400	15	83	820	91.9
33	Charged	760	500	15	83	965	96.5

Table 5-2. Printing parameters and estimated film coverage for the 33 samples analyzed in this study. The first four parameters (i.e., foil charged/floating status, printhead-to-substrate gap, focus/foil voltage (when biased), and inner gas flow rate) were determined in accordance with a DOE; the outer gas flow rate was chosen for each deposition to ensure that the anode voltage remain in an acceptable range. The anode voltage was a dependent parameter adjusted to maintain 1 mA current in the plasma.

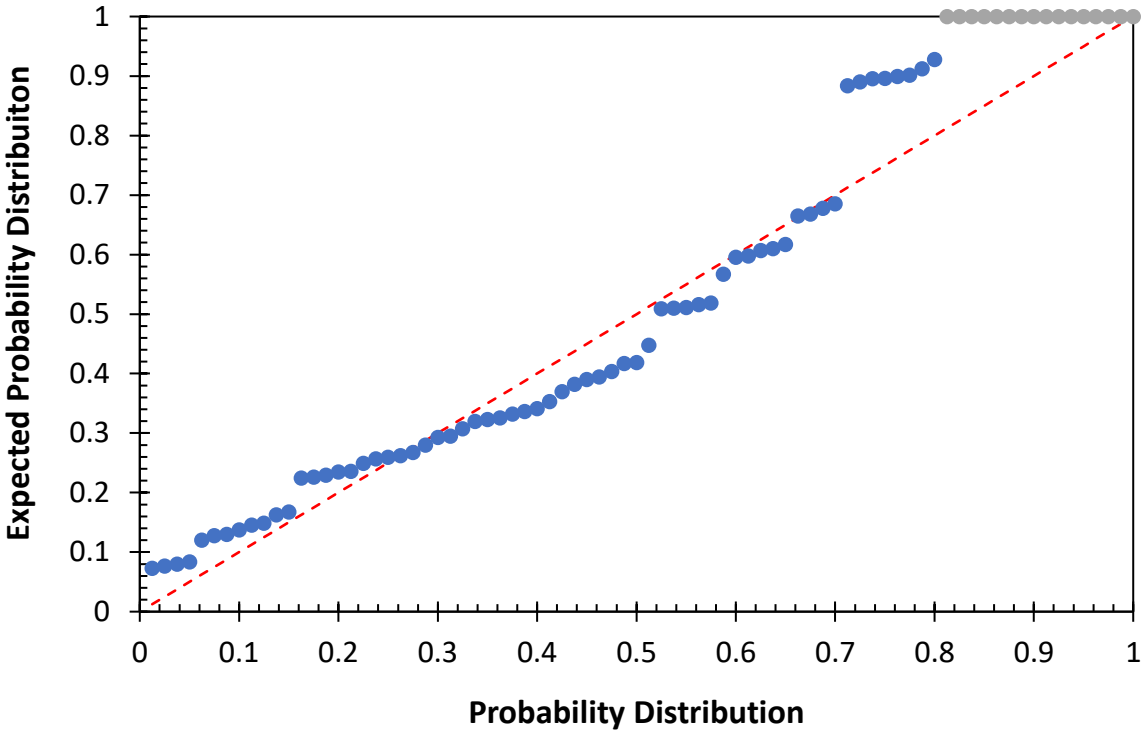

Figure 5-5. A quantile-quantile (q-q) plot of the various parameters of the ensemble of reduced models for the deposits produced with a negatively biased plate. The grey spots represent the p-value of the effect of the negative voltage on the focus electrodes and biased plate; they are far above the dashed line, which represents the expected results from random noise. Clearly, the grey spots' significance cannot be attributed to mere chance. The blue dots represent the p-values of all other parameters, which largely follow the dashed line, showing that they are not statistically significant. The set of points with a p-value near 0.9 is a statistical artifact; there is a slight unintended correlation (R^2<0.1) between the substrate bias voltage and the plasma-substrate gap; when the substrate bias voltage is excluded from a reduced model, the gap becomes significant. However, this is clearly a statistical artifact; when the voltage is included in a reduced model, the effect of the gap, an imperfect measure of the voltage, becomes insignificant.

Parameter (units)	**Effect (Coverage/unit)**	**t Statistic**	**p**
Constant	0.71		
Substrate/Focus bias voltages (V)	5.78×10^{-4}	5.09	1.31×10^{-4}

Table 5-3. Reduced-order model for film coverage, for films with biased foil. This model uses one statistically significant parameter and accounts for the majority of the samples' variance in film coverage (R^2=0.634).

a smaller printer-substrate gap and stronger outer flow are advantageous for a more complete coating.

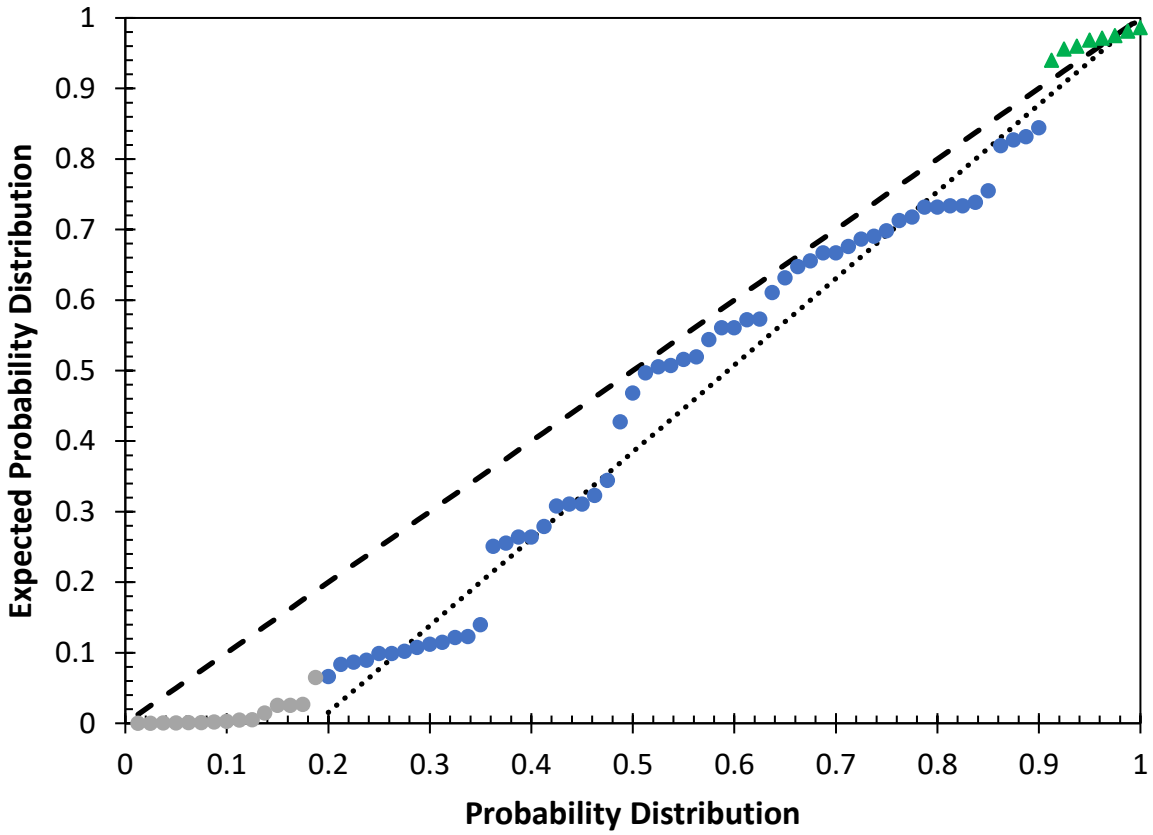

Figure 5-6. A quantile-quantile (q-q) plot of the various parameters of the ensemble of reduced models for the deposits produced with an electrically isolated plate. The grey dots represent the p-value of the effect of the substrate-printer gap; they are far below the dashed line, which represents the expected results from random noise. Clearly, the grey dots' significance cannot be attributed to mere chance. Once the grey dots are removed from the set of possibly random parameters, the dotted line represents the new expected distribution; the blue dots lie along that line. The green triangles represent the effect of the outer gas flow; they are slightly above the dotted line, which suggests, but does not show conclusively, that they have a statistically significant effect.

Parameter (units)	**Effect (Coverage/unit)**	**t Statistic**	**p**
Constant	1.21		
Printer-substrate gap (μm)	-1.27×10^{-3}	-3.64	8.26×10^{-3}
Outer gas flow (sccm)	1.80×10^{-3}	1.92	0.096

Table 5-4. Reduced-order model for film coverage, for films produced with electrically isolated foil. Because there is no focus bias voltage, other effects are significant, and we include two parameters with significant correlation to explain the majority of the samples' variance in film coverage (R^2=0.665). In the text, we discuss the dubious significance of the outer gas flow.

5.4. Ion Energy

In this section, a physical explanation of why the chosen parameters affect the electrical conductivity is presented. The case of the negatively biased plate is considered first. To understand the effect of the bias, we return to Thornton's model, in which the effects of process parameters on film growth are explored. Thornton claimed that there were two important process parameters, i.e., the chamber pressure and the substrate temperature. However, a later refinement of the model, by Mahieu [5:8] and Messier [5:3], claims that at an atomic level, the energy of the impinging atoms is the sole relevant parameter. As in Thornton's model, thermal energy is imparted to the sputtered atoms by heating the substrate, giving the atoms enough energy to rearrange into an energetically favorable position. Thornton's other process parameter, background pressure, is relevant due to its impact on the bombardment velocity. When an atom is sputtered from the target, it has an initial kinetic energy of several eV. High pressure causes the impinging atom to undergo many collisions; these collisions, in addition to changing the direction of motion, also drastically reduce the impinging atom's kinetic energy. Thus, in a low-pressure sputtering chamber, the original impulse of sputtering causes the impinging atom to have a high enough kinetic energy to enhance its mobility once it is adsorbed onto the substrate. Consequently, any method of imparting energy to the sputtered atoms will lead to a dense, conductive microstructure.

In the experiments of this chapter, the electric field due to the negative bias voltage under the substrate is sufficient to impart kinetic energy to the ionized material. Specifically, consider a typical set of parameters, and compare the energy imparted by the electric field to the energy imparted in traditional sputtering by heating the substrate. In this case, the stage under the substrate has a bias voltage of -300 V, and the stage is approximately 2 mm below the positively charged plasma. Near the target wire, this plasma has a voltage of approximately 400 V, for a total electric field E of approximately 350 kV/m. In the DOE experiments, the negative bias was directly applied to the substrate. However, in subsequent experiments (described in Chapters 4, 6, 7, and 8), a 1 MΩ resistor was placed between the substrate and power supply (Figure 5-7) to prevent the plasma from forming directly between the anode and substrate (see Section 2.5.).

The ion mobility, K_0, of gold is approximately 1.71×10^{-3} $m^2/V/s$ at standard temperature and pressure [5:9] in a helium background; i.e., an electric field of 1 V/m would lead to a drift velocity of 171 μm/s, the speed at which the electric field's acceleration would be cancelled by the drag caused by collisions . Due to the increased mass of molecular nitrogen, this implies an ion mobility of approximately 6.5×10^{-4} $m^2/V/s$ in an air background. This would imply a drift velocity of $v = K_0E$, 227 m/s, or an average energy of 53 meV per gold atom. This is equivalent to the thermal energy that is due to an increase of 610 K, which, combined with room temperature, is of the order necessary for dense, conductive nanostructures.

Other novel sputtering methods use similar techniques. High-Power Impulse Magnetron Sputtering (HiPIMS), which pulses (impulses) high currents at a low duty cycle to ionize a large fraction of the sputtered material, has been combined with a negative bias voltage to the substrate

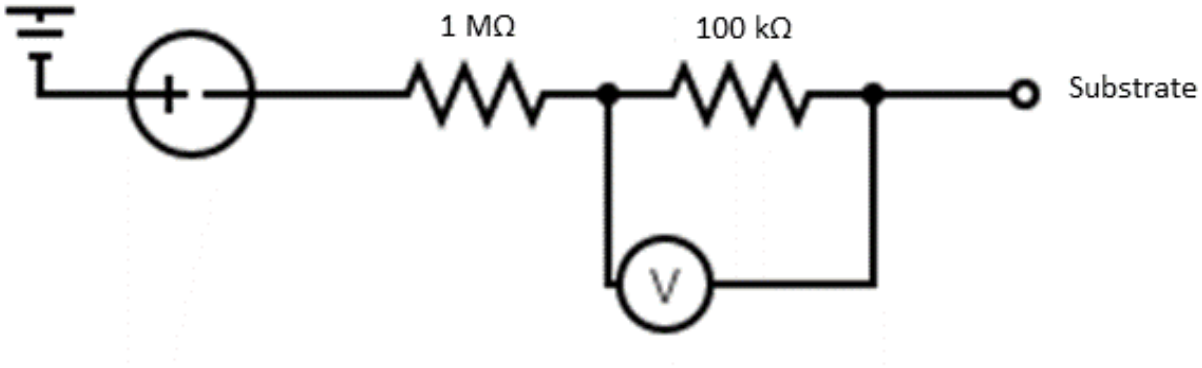

Figure 5-7. A typical schematic of the improved setup, in which the substrate itself is biased. The resistors prevent a plasma from forming directly between the anode and substrate. The voltmeter measures the voltage drop across a resistor; we use a voltmeter instead of an ammeter in order to protect the multimeter from high transient currents that might burn out an ammeter but not the voltmeter.

to ensure that the ionized material impacts the substrate with large velocity and forms a smooth and mechanically sound coating [5:10],[5:11].

Now, consider to the other set of results, in which there was no negatively biased plate. In this case, the relevant process parameters are also indicative. In the absence of energetic ions drawn to the substrate, the plasma itself imparts the necessary energy to the substrate to rearrange the atoms into a dense coating. For the plasma to reach the substrate, a smaller printer-substrate gap and stronger outer flow are advantageous for a more complete coating. The outer flow, which flows through a significantly larger nozzle, can drive the plasma away from the printhead and towards the substrate more than the inner flow, with a much smaller nozzle, can. If the target-substrate gap is small enough, the high-energy ions and electrons of the plasma impart the necessary energy to the substrate to allow for the dense coating. Post-deposition plasma processing has been reported before, with similar effects [5:12],[5:13]. Although the DOE demonstrates this phenomenon, it is not as easily controlled as the effect of the substrate bias, and thus the substrate bias, not the plasma voltage, is harnessed in future depositions to improve the film's conductivity.

5.5. Overly Energetic Atoms.

The reduced model explains over 70% of the variation for the majority of cases (Figure 5-8). However, there is a minority of cases in which very good film coverage is expected, but instead, the imprint has very poor film coverage; these imprints are composed of a series of isolated droplets. This is likely due to the impinging atoms having too much energy when they arrive at the substrate. These overly energetic atoms damage the already deposited film, preventing buildup of a strong film. Because the distance between the plasma and the substrate is so short, it is reasonable to unexpectedly have a distance that is slightly shorter than normal, and, as a result, have an electric

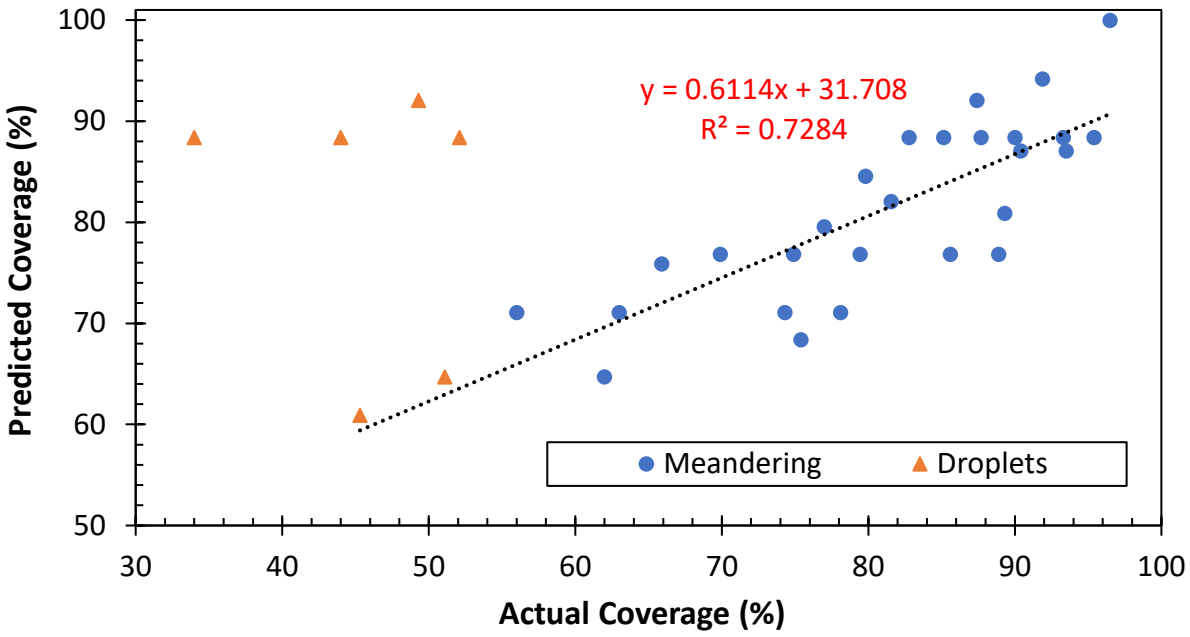

Figure 5-8. Comparison of predicted coverage and actual coverage. The best fit line, which includes all the meandering deposits but not the isolated droplets, explains the majority of the variance of the meandering deposits. However, there are four deposits that, based on the process parameters, should have very high coverage, and instead have very low coverage. We posit that the sputtered ions are too energetic for an effective deposition.

field that is so great that the ions are accelerated to the point where they damage the deposited film. This effect has been seen in other cases, albeit in vacuum [5:14].

The effect of overly energetic atoms can be seen when the microsputterer is passed over some traditionally sputtered traces. In the presence of a 500 V negative bias (applied directly to the substrate, as described earlier), the impinging atoms are so energetic that they ablate the preprinted traces (Figure 5-9). In contrast, when the bias is a mere 300 V, the traces are undamaged.

Here too, it is useful to examine the ion mobility and ion energy. The substrate is approximately 500 µm below the target wire and the plasma; the plasma has a voltage of 400 V, for a total voltage difference of 900 V between the negatively charged substrate and the positively charged plasma. Thus, the electric field between the plasma and substrate is 900 V/ 500 µm, or 1.8 $\mathrm{MV \cdot m^{-1}}$. The drift velocity, $v = K_0 E$, is 1170 m/s, and the average ion energy is 1.38 eV. This is comparable to 2 eV, the lowest energy at which ion etching has been reported [5:15].

The ablating ion energy is also approximately half of the heat of vaporization of gold, i.e., 3.1 eV. Given that the heat of vaporization is the energy necessary to break all of an atom's bonds, allowing an atom to become gaseous, half the heat of vaporization is approximately sufficient to break the bonds between a gold atom on the surface of a thin film and its neighbors. This is because

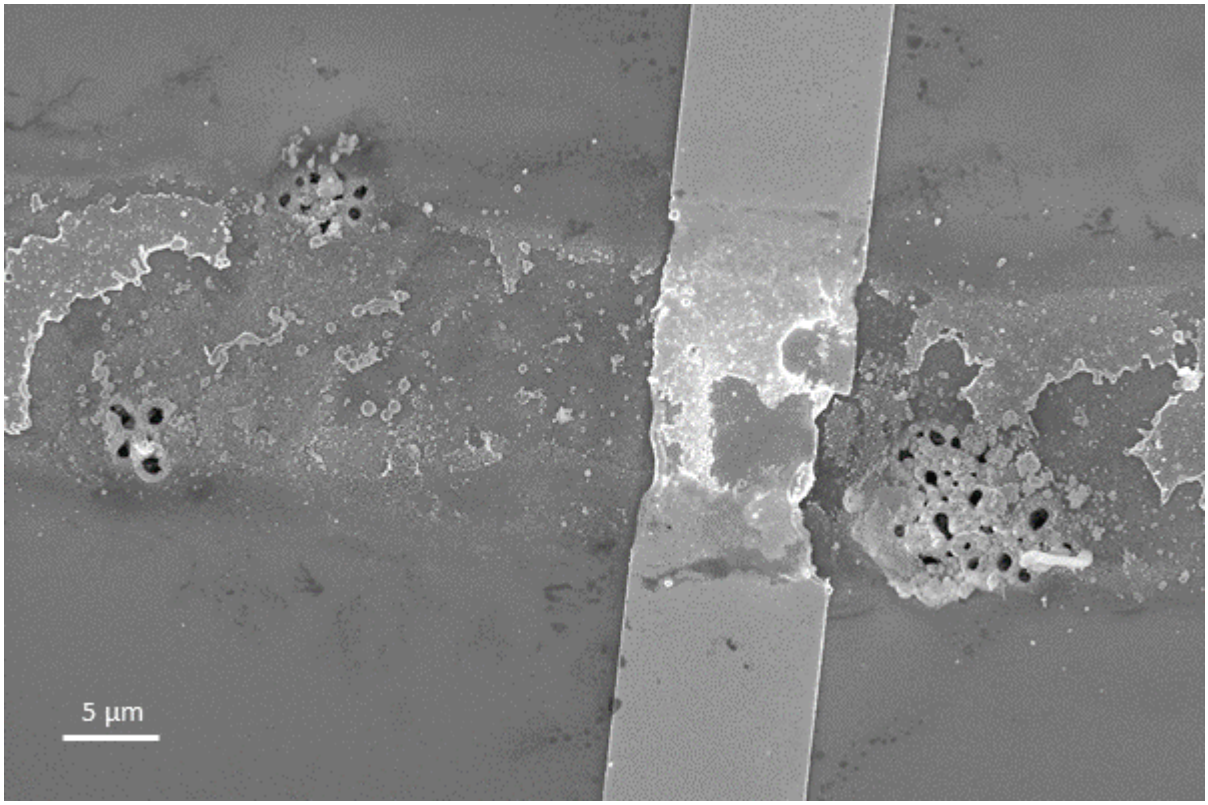

Figure 5-9. A micrograph from a SEM of a (vertical) traditionally sputtered gold film (100 nm thickness, 10 µm wide), damaged by an overlay (horizontal) printed from our sputterer.

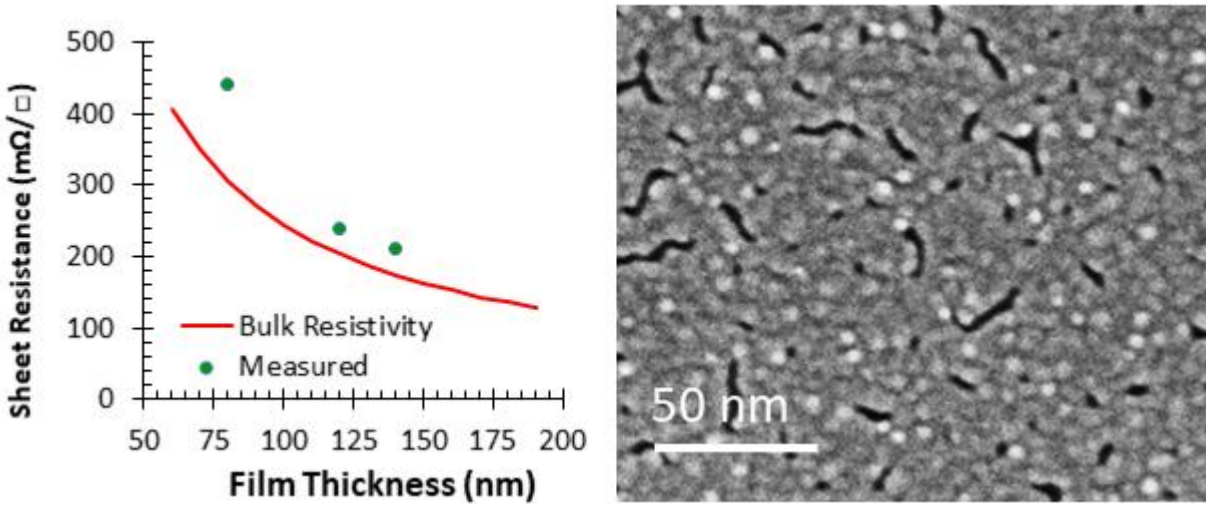

Figure 5-10. A graph (left) of the resistivity of the nanoparticle-enhanced deposit, as a function of film thickness, as compared to bulk conductivity, and an SEM micrograph of the deposit (right). Note the very high density. The micrograph was included as part of Figure 4-7.

an atom on the surface of the film has only half of its compliment of neighbors, and thus can be removed with half of the energy necessary to vaporize bulk gold. Specifically, each bond between gold atoms has an energy of 0.6 eV at a gold-air interface [5:16]; these high-energy ions have the energy necessary to break two bonds. The relationship between the heat of sublimation and the sputtering threshold has been noted previously [5:17]; however, because of the density of the metal in that study, higher sputtering thresholds were found. In the case of microsputtered deposits, because the film is thin and not dense, fewer bonds must be broken to sputter an atom.

5.6. Effect of Nanoparticle Size

If the film is created by combining large (~50 nm radius) and small nanoparticles, the production of which was described in Chapter 4, the conductivity of the microsputtered thin film is further improved. As Chapter 4 described, the nanoparticles form in a high-energy, high-density plasma. The energy of the plasma allows the atoms to pack together densely. When the resultant nanoparticles then reach the substrate, they allow the formation of a denser film. Due to the absence of voids within the nanoparticles and relatively small gaps between the nanoparticles, the conductivity is more than 80% that of bulk gold (Figure 5-10). Specifically, a minimum resistivity of 2.9 μΩ·cm was measured, compared to bulk gold's resistivity of 2.44 μΩ·cm.

This result can be examined more quantitatively by exploring how the energy of a nanoparticle scales as the nanoparticle grows. It can be shown that the energy changes drastically as the size of the nanoparticle changes, leading to a wide range of energies. The high-energy, long tail of the distribution ensures that some particles will have the energies necessary to rearrange grain boundaries, even while very few particles are energetic enough to damage the films.

Assume a nanoparticle with the density of bulk gold and a single charge. By Stokes' Law, the drag force on a Brownian particle, such as a nanoparticle, is $F = 6\pi\eta r v$, where η is the viscosity of the medium and r is the radius of the nanoparticle. This will be counteracted by the electrical force, $F = qE$. The drift velocity, the velocity at which these two forces are equal, is

$$v = \frac{qE}{6\pi\eta r}. \tag{5-1}$$

For a singly charged nanoparticle, the velocity is thus inversely proportional to the radius. The energy per nanoparticle is proportional to the mass multiplied by the square of the velocity, or equivalently, to the radius. This energy is distributed over the entire surface area of the nanoparticle as it impacts the substrate and rearranges at the boundaries, leading to an energy per unit area that is inversely proportional to the radius, a weak dependence.

However, larger nanoparticles are no longer limited to a single charge per nanoparticle. Instead, once a nanoparticle has a radius of tens of nanometers, it has multiple charges, and thus, assuming the charge per mass (and thus per volume) is constant, the charge is proportional to the radius cubed, the velocity is proportional to the radius squared (charge/radius), and the energy per unit area to the radius raised to the fifth power (velocity^2 · mass/radius^2). Thus, a small change in nanoparticle radius leads to an enormous change in energy.

To illustrate, let us assume that 2×10^{-7} of gold atoms are ionized, matching the ionization rate of the atmospheric plasma in our COMSOL simulations. A nanoparticle with a 50 nm radius will have a mass of 10 fg, or 3×10^{7} gold atoms. That nanoparticle will have a charge of +6. The substrate-plasma gap is 3 mm, while the substrate-plasma voltage difference is 800 V, yielding an electric field of 233 kV/m. The terminal velocity is thus 13.1 mm/s, and the kinetic energy is thus 5.36 eV, or 2.7 $\text{meV} \cdot \text{nm}^{-2}$ across its surface area. If the radius of the particle is increased to 55 nm (a 10% increase), the energy per unit area increases to 4.3 $\text{meV} \cdot \text{nm}^{-2}$. Consequently, because the film is being bombarded with ions of many different energies, the highest energy nanoparticles allow it to readily rearrange itself. However, the film does not undergo significant damage because the majority of the ions are not energetic enough to damage the film. This is similar to the effects of cluster beam deposition, in which nanoparticles are formed and, upon impact with the substrate, break apart with enough energy to form a dense film [5:18]. Similar to this work, cluster beam deposition uses nanoparticles because they are more energetic than single atoms. However, because microsputtering works at atmospheric pressure, the nanoparticles it produces are not energetic enough to break apart upon impact; nonetheless, they have sufficient energy to form dense, conductive films, albeit in a different method than the one harnessed by cluster beam deposition. If there are sufficient smaller particles to fill in the voids (as in Chapter 4), a dense, highly conductive film is formed.

5.7. Assessment of Electrical Resistivity Using a Network Model.

To help understand why the nanoparticle-enhanced film is much more conductive than the previous results, a network model is used to quantitatively examine the electrical resistivity of the film. From this model it can deduced that the chasms are imperfectly filled in the absence of nanoparticles, while the nanoparticles act as additional conductive bonds between crystal grains.

First, consider with a film **without** nanoparticles. One can quantify the effect of the chasms by modelling the conductive gold film as an infinite square resistor network (Figure 5-11), where the nodes are the individual grains and the resistors, joining the nodes, are the chasms between the grains. Each chasm can either be filled, and thus have a low resistance R_1, or a chasm, which is not filled, and have infinite resistance. In our case, R_1 represents the sum of the resistance of the gold grain itself and the filled-in chasm between one grain and the next. The probability that a given resistor has a low resistance (or, equivalently, that a chasm is filled-in) is denoted by C. Previous research [5:19] has shown that the electrical conductivity of such a network follows a scaling law,

$$\sigma = \sigma_1 (C - C^*)^p \tag{5-2}$$

where σ and σ_1 are the reciprocals of the total resistance per length and R_1, respectively, and C^* is the critical probability, i.e., the minimum fraction of resistors that must have R_1 resistance for the network to have finite resistance between two parts an arbitrary distance away. This critical probability is 0.5 (i.e., if every grain is, on average, connected to half of its neighbors, the film will be electrically conductive) and p is found to be 1. Thus, if the probability of a chasm being filled is C, the resistivity between two points a distance N away will be

$$R = \frac{N \cdot R_1}{C - 0.5} \tag{5-3}$$

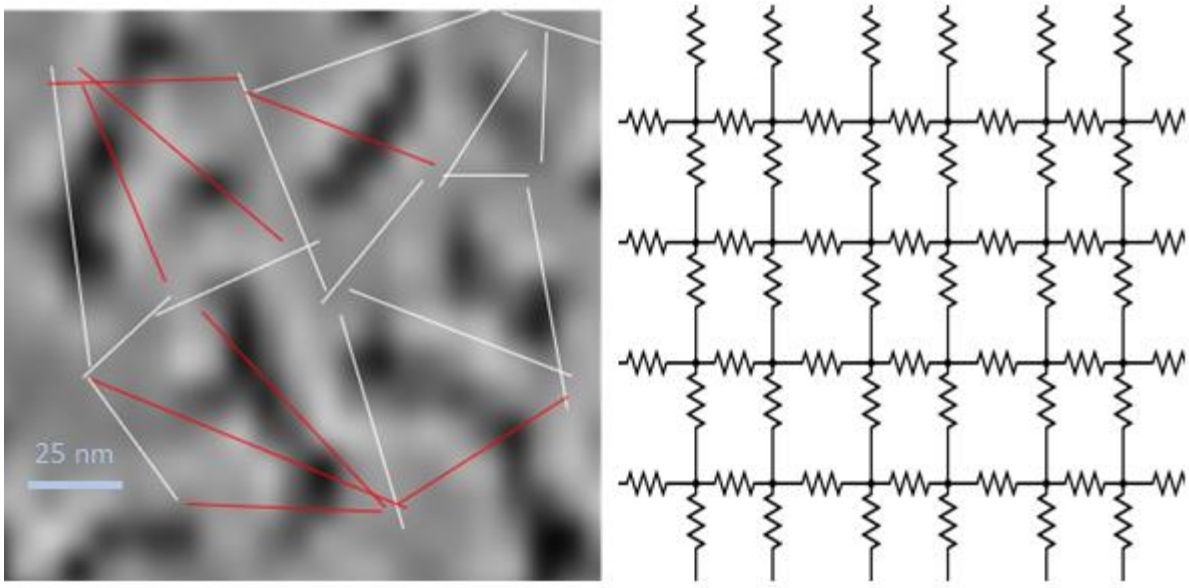

Figure 5-11. A section of the sputtered film (left), modelled as a resistor network. The center of each grain is connected to the center of each neighboring grain either with a finite resistor (white) or an infinite resistor (red). This is similar to the analytically solved problem of an infinite square resistor network (right). Each node (black circle) is connected to four other nodes through a resistor. In our model, these nodes represent the center of grains and the resistors represent the lumped resistance both within a grain and between joined grains.

C cannot be found directly; however, it can be estimated by examining the SEM micrograph of the deposit. Let us assume that an average grain size is a square A length per side, with a chasm width of B. Thus, the total coverage, T will equal the fraction of covered area (grains and filled-in chasms) divided by the total area (grains and all chasms):

$$T = \frac{A^2 + 2C \cdot A \cdot B}{A^2 + 2A \cdot B} \tag{5-4}$$

Or

$$C = \frac{\left((A^2 + 2A \cdot B)T - A^2\right)}{2A \cdot B} = T\left(1 + \frac{A}{2B}\right) - \frac{A}{2B}. \tag{5-5}$$

By inspection, $A \sim 20B$, and thus $C \sim 1.2T - 0.2$. Substituting into Equation (5-3), we find

$$R = \frac{N \cdot R_1}{1.2T - .7} \tag{5-6}$$

When Equation (5-6) is compared to experimental data, the relationship is accurate, with slight variances in the parameters (Figure 5-12) specifically, the conductivity is found to vary linearly with the total coverage, with a slope to intercept ratio of approximately 12:7. Extrapolating

to $T = 1$, we find that even with no chasms, the resistivity corresponding to the found value of R_1 would be approximately 34 μΩ·cm, or approximately twelvefold bulk. Thus, even if we could fill in every visible void, we still would not achieve bulk conductivity without the use of nanoparticles. The difference between microsputtered deposits and the true bulk resistivity of gold is likely due to imperfect filling of the grain boundaries; even the boundaries that are filled are not filled perfectly, and thus their conductivity does not match bulk gold.

However, the presence of nanoparticles improves on the filling of the chasms by bridging the chasms. A single nanoparticle is energetic enough (as described in the previous section) and large enough to bridge a chasm completely. As long as it has the energy to rearrange the atoms at the points of contact with the grains on either side of the chasm, it can serve as a bonding wire between two grains – a highly conductive, well-bonded metal that joins two contacts perfectly. Smaller nanoparticles and atoms can then serve as "cement" to ensure a dense, three-dimensional nanostructure. With the use of nanoparticles, we can achieve lower electrical resistivity; R_1 decreases by an order of magnitude.

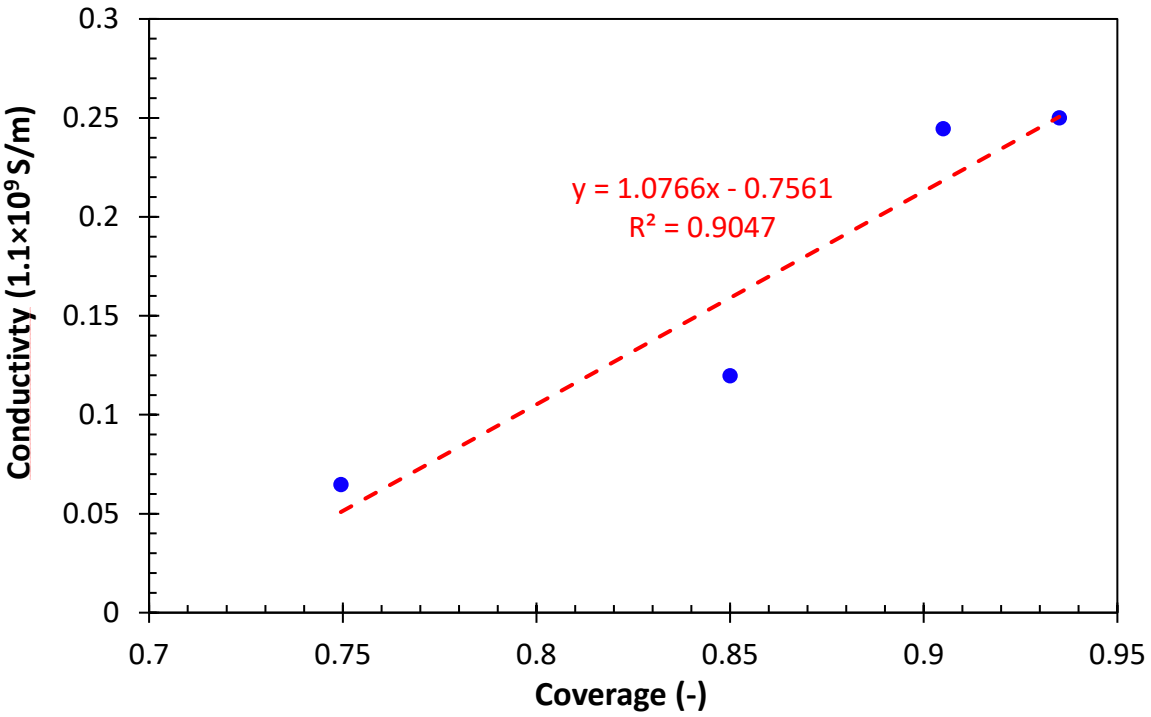

Figure 5-12. A graph comparing coverage and conductivity without the use of nanoparticles, with a best fit line. The units of conductivity are 1.1×10^9 S/m, representing σ_1 of Eq. 5-1. This yields an equation $\frac{\sigma}{\sigma_1} = 1.076\mathrm{T} - 0 - 756$. Eq. (5-3) suggests an equation of $\frac{\sigma}{\sigma_1} = 1.2 - 0.7$

Thus, we have three types of connections between grains: a void, with infinite resistance; a chasm imperfectly filled-in with small nanoparticles, with moderate resistance; and a nanoparticle bonded to both parts of the void, with near-bulk resistance. To achieve 1.2X bulk

resistance, Eq. (5-3) suggests that it would be necessary to bridge 90% of the grain-grain boundaries (C~0.9), if the nanoparticles bond grains perfectly. SEM micrographs suggest that this is achieved.

Additionally, with multiple layers of nanoparticles, this desired conductivity could be achieved with three-dimensional percolation, requiring an even lower fraction of coverage [19]. However, the exact solution for a 2.5-D infinite network (i.e., a network infinite in two dimensions but with few layers in the third dimension) with anisotropic bonds (i.e., the gap-filling mechanism differ from the nanoparticle-stacking mechanism) is not easily found. Thus, the addition of nanoparticles transforms this network of resistors from a two-dimensional network with resistors with moderate resistance to a network where the resistors have near-bulk resistance. Furthermore, the thicker the film, the more similar it is to a three-dimensional network, with even lower resistance for comparable coverage. However, the effect of the additional layers is smaller than the effect of the effective bond filling, and is thus not necessary for our calculations.

5.8. Comparison to Previous Work

The electrical conductivity achievable by thin films made of nanoparticle-structured, microsputtered gold is unmatched by any other additive manufacturing method that does not rely on high-temperature annealing. The most conductive room-temperature silver nanoparticle-based inks, without sintering, have a resistivity over an order of magnitude greater than our samples [5:20]. At "mild" sintering temperatures (140 °C), the resistivity is still almost double ours, i.e., 4.6 μΩ·cm [5:21]. This is despite the use of silver, whose bulk resistivity is less than two-thirds that of gold. Other microplasma sputtering methods, which include substrate heating, have an electrical resistivity 20% greater than our unheated films [5:22]. The high-energy, large nanoparticles bind neighboring grains together well, in a manner only matched by high mobility due to high thermal energy, which has the advantage of moving all atoms, rather than just the ionized ones.

5.9. Conclusion

This chapter describes the challenges and solutions of improving the nanostructure and electrical conductivity of atmospheric pressure sputtered gold thin films. Instead of heating the substrate as in traditional (vacuum) sputtering, our method uses a bias voltage applied to or beneath the substrate to achieve similar improvements in film density and electrical conductivity. We compared the energy of ions drawn to a negative bias voltage to the thermal energy imparted by a heated substrate, discussed the tendency of overly energetic particles to damage deposited films, and explained how near bulk (i.e., 1.2X bulk) electrical resistivity can be attained in nanoparticle-structured microsputtered films, modeling the film as a resistor network in which the nanoparticles bridge the chasms more effectively than individual atoms could.

5.10. References

[5:1] Kornbluth YS, Mathews RH, Parameswaran L, Racz LM, Velásquez-García LF. Room-temperature, atmospheric-pressure microsputtering of dense, electrically conductive, sub-100 nm gold films. Nanotechnology. 2019 Apr 24;30(28):285602.

[5:2] Hang ZY, Thompson CV. Grain growth and complex stress evolution during Volmer–Weber growth of polycrystalline thin films. Acta Materialia. 2014 Apr 1;67:189-98.

[5:3] Messier R, Giri AP, Roy RA. Revised structure zone model for thin film physical structure. Journal of Vacuum Science & Technology A: Vacuum, Surfaces, and Films. 1984 Apr;2(2):500-3.

[5:4] Granqvist CG. Transparent conductors as solar energy materials: A panoramic review. Solar energy materials and solar cells. 2007 Oct 15;91(17):1529-98.

[5:5] Thornton JA. Structure-zone models of thin films. In Proc SPIE 0821, *Modeling of Optical Thin Films*, 1988 Feb 2 (Vol. 821, pp. 95-105). International Society for Optics and Photonics.

[5:6] Chapman BN. *Glow discharge processes: sputtering and plasma etching*. Wiley; 1980.

[5:7] Schweder T, Spjøtvoll E. Plots of p-values to evaluate many tests simultaneously. Biometrika. 1982 Dec 1;69(3):493-502.

[5:8] Mahieu S, Ghekiere P, Depla D, De Gryse R. Biaxial alignment in sputter deposited thin films. Thin Solid Films. 2006 Dec 5;515(4):1229-49.

[5:9] Gilb S, Weis P, Furche F, Ahlrichs R, Kappes MM. Structures of small gold cluster cations (Au n+, n< 14): Ion mobility measurements versus density functional calculations. The Journal of Chemical Physics. 2002 Mar 8;116(10):4094-101.

[5:10] Brenning N, Axnäs I, Raadu MA, Lundin D, Helmerson U. A bulk plasma model for dc and HiPIMS magnetrons. Plasma Sources Science and Technology. 2008 Aug 26;17(4):045009.

[5:11] Anders A. A review comparing cathodic arcs and high power impulse magnetron sputtering (HiPIMS). Surface and Coatings Technology. 2014 Oct 25;257:308-25.

[5:12] Park JS, Jeong JK, Mo YG, Kim HD, Kim SI. Improvements in the device characteristics of amorphous indium gallium zinc oxide thin-film transistors by Ar plasma treatment. Applied Physics Letters. 2007 Jun 25;90(26):262106.

[5:13] Neumüller A, Sergeev O, Vehse M, Agert C. Structural characterization of the interface structure of amorphous silicon thin films after post-deposition argon or hydrogen plasma treatment. Applied Surface Science. 2017 May 1;403:200-5.

[5:14] Anders A. Observation of self-sputtering in energetic condensation of metal ions. Applied Physics Letters. 2004 Dec 20;85(25):6137-9.

[5:15] Fujiwara N, Shibano T, Nishioka K, Kato T. Cold and low-energy ion etching (COLLIE). Japanese Journal of Applied Physics. 1989 Oct;28(10R):2147.

[5:16] Qi W, Huang B, Wang M. Bond-length and-energy variation of small gold nanoparticles. Journal of Computational and Theoretical Nanoscience. 2009 Mar 1;6(3):635-9.

[5:17] Stuart RV, Wehner GK. Sputtering yields at very low bombarding ion energies. Journal of Applied Physics. 1962 Jul;33(7):2345-52.

[5:18] Takagi, T. Ionized cluster beam technique for thin film deposition. *Zeitschrift für Physik D Atoms, Molecules and Clusters* 3.2 (1986): 271-278.
[5:19] Webman I, Jortner J, Cohen MH. Critical exponents for percolation conductivity in resistor networks. Physical Review B. 1977 Sep 15;16(6):2593.
[5:20] Walker SB, Lewis JA. Reactive silver inks for patterning high-conductivity features at mild temperatures. Journal of the American Chemical Society. 2012 Jan 25;134(3):1419-21.
[5:21] Mo L, Guo Z, Wang Z, Yang L, Fang Y, Xin Z, Li X, Chen Y, Cao M, Zhang Q, Li L. Nano-silver ink of high conductivity and low sintering temperature for paper electronics. Nanoscale Research Letters. 2019 Dec;14(1):1-1.
[5:22] Burwell IV ED. *A microplasma-based sputtering system for direct-write, microscale fabrication of thin-film metal structures* (Masters dissertation, Case Western Reserve University, 2016).

Chapter 6 —Ion Energy in the Microplasma

6.1. Introduction

This chapter discusses what is arguably the project's greatest hurdle: the low sputtering rate associated with microplasmas. Specifically, the chapter explains why the high collisionality of the microplasma forces the ion energy to remain low, causing a low deposition rate. The chapter then explores several approaches to increase sputtering rate, such as optimization of the target shape, increased current, and stronger gas flow. However, these methods offer only a modest improvement. After that, the chapter describes the dependence of ion and electron energy on the gas composition of the plasma and proposes a mixture of monoatomic and diatomic gases to increase the ion energy and sputter yield. Finally, the chapter reports the experimental results of using such a gas blend when microsputtering gold and aluminum.

6.2. Microsputtering vs. Traditional Sputtering Deposition Rate

Sputtering is an inherently slow process, as each ion only removes one to a few atoms of material from the target's surface. However, the microsputterer reported in this thesis coats surfaces at 50 times the rate of a traditional sputterer *per unit area of target*. Specifically, while an industrial sputter uses a 2-inch disk or larger target to coat an 8-inch wafer at a deposition rate of ~$1\ \mathrm{nm}\ s^{-1}$, equal to a volumetric removal rate of target material of $3.2 \times 10^{-2}\ \mathrm{mm^3 s^{-1}}$. the microplasma sputterer uses a 100-µm diameter wire target to coat a 5 $\mathrm{mm^2}$ area at the same deposition rate ($1\ \mathrm{nm}\ s^{-1}$), equal to a volumetric removal rate of target material of $3.9 \times 10^{-6}\ \mathrm{mm^3\ s^{-1}}$.

A large portion of the answer is due to the size of the sputtering target and the power used. An industrial sputterer uses (at least one) 2-inch sputtering target (2025 $\mathrm{mm^3}$). The microplasma printer uses, typically, a 100 µm diameter wire (7850 $\mu\mathrm{m^2}$). With an area over five orders of magnitude lower, it is an achievement to sputter at a rate "only" four orders of magnitude lower. Put differently, the microsputterer coats surfaces at 39 times the rate of a traditional sputterer, *per unit area of target*.

The reason for the enhanced rate is that the sputtering rate is proportional to the current density: a traditional sputterer has a current density of 0.3 $\mathrm{mA/mm^2}$ (6 A spread across the two-inch target), while the microsputterer has a current density of 380 $\mathrm{mA/mm^2}$ (3 mA spread across the target wire area).

Such a high current density is only possible due to convective cooling. If it is assumed that a typical ion strikes the target with 50 eV of energy, the traditional sputterer absorbs $15\ \mathrm{mW \cdot mm^{-2}}$ of energy, or 300 W for the whole 2-inch target. Given that the sputtering target in a traditional system is in vacuum, heat transfer due to convection can be neglected. In addition, if the temperature of the target is not high (< 600 °C), radiation heat transfer can also be ignored. Gold, a typical sputtering material, has a thermal conductivity of $310\ \mathrm{W/(m \cdot K)}$; consequently, it can dissipate the heat with a temperature gradient of $480\ \mathrm{K \cdot m^{-1}}$—extremely low. However, if

the traditional sputtering head had a power density on par with the microplasma head (i.e., 19 W · mm^{-2}), it would need to dissipate 380 kW of heat. Leaving aside the tremendous power consumption, the temperature gradient would need to be 608 K · mm^{-1}; consequently, if the target was more than 2 mm from a cooling source, it would melt (the melting temperature of gold is 1064 °C). However, the microsputtering target wire is surrounded by a cooling flow that convects away the heat. If the sputtering target is modeled as the end of an infinite fin, the heat removed Q by the flow is

$$Q = \Delta T\sqrt{pAkh} = \Delta T\sqrt{2\pi^3 \cdot r^3 \cdot 310 \cdot 200} = \Delta T \cdot 4.9 \times 10^{-4}\ W \tag{6-1}$$

where p is the perimeter of the wire target, A is the cross-sectional area of the target, and k and h the conduction and convection heat transfer coefficients, respectively (for gold $k = 310\ W\ m^{-1}K^{-1}$ and $h = 200\ W\ m^{-2}K^{-1}$ for fast flow of forced convection). The energy dissipated is equal to the ion energy E_i times the current I, i.e.,

$$\mathrm{Q} = I \cdot E_i \tag{6-2}$$

Combining equations 6-1 and 6-2 results in $\Delta T = 306\ K$. In other words, the total heat load of 150 mW can be dissipated with a temperature gradient of 306 K, causing no phase change in the target or collapse of the reactor.

As technically impressive as this result may be, it is of small comfort. In practical terms a certain throughput is required (a particular deposition thickness across a given area per unit of time), not a given throughput per unit area. Additionally, per unit of current, following the calculations above, the microsputterer only has 5% of the sputter yield *per unit of current* of a traditional sputterer. This is due to the decreased ion energy in the microplasma. Accordingly, this chapter will explore methods to improve the sputter yield per unit of current.

6.3. Influence of Ion Energy in Sputtering Yield

Sputtering requires that energetic ions impact the target, dislodging atoms from the target by freeing the atoms from their bonds. The ions, clearly, must be energetic. The energy of the ions can be derived from the electrical mobility of the ions μ—a measure of how the drift velocity of an ion depends on the local electric field. Specifically, a charged particle under the influence of an electric field E will have an average drift velocity v of

$$v = \mu E. \tag{6-3}$$

The ion mobility is inversely proportional to the density of the background gas and is often given in terms of μ_o—the mobility at standard temperature and pressure.

Similarly, electrons also have an electrical mobility, representing a near-linear relationship between the electric field and the electron velocity. This relationship is important in determining the electron energy, which in turn determines the collisional cross-section of various plasma

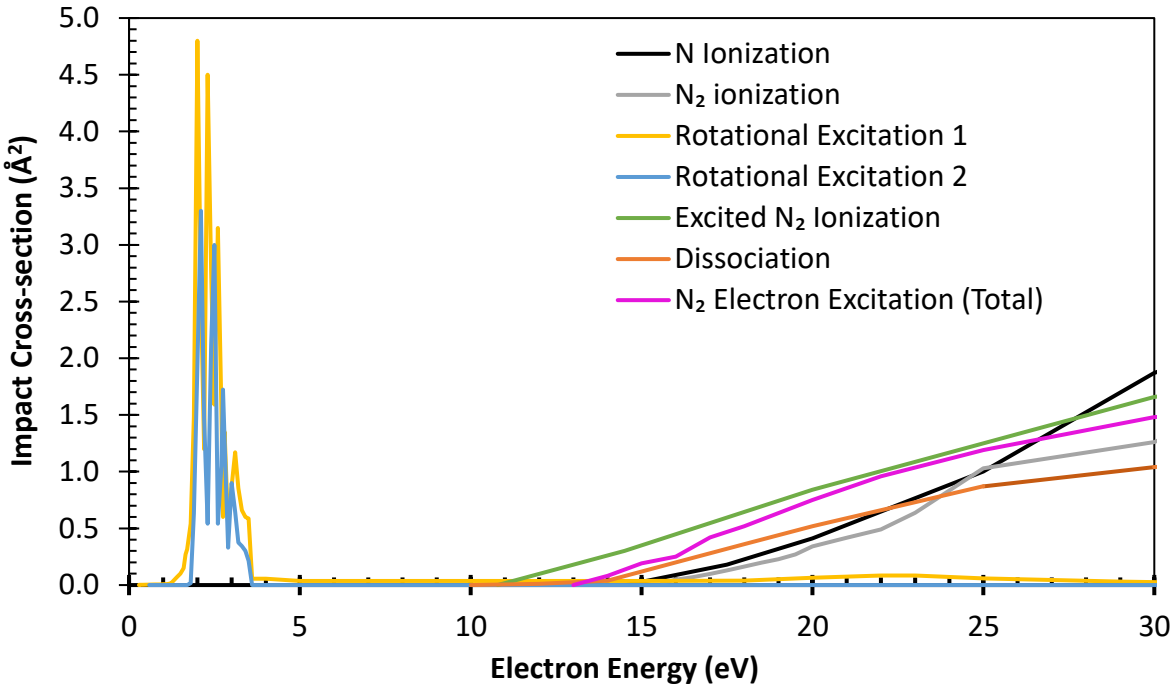

Figure 6-1. A chart of selected electron impact cross-sections for molecular nitrogen for a range of relevant electron energies. Note that excitation of the molecular bond at various modes dominates at low (<5 eV) energies, while ionization becomes relevant at energies greater than 15 eV. Also note, as described in Section 3.4, that excited N_2 molecules ionize more readily than molecules in the ground state. Dissociation data is drawn from [6:1]; all other data is from [6:2]. These values are typical for diatomic molecules; monoatomic atoms do not have rotational excitation, dissociation, or diatomic ionization, but do have monatomic ionization, electronic excitation, and excitation of excited species.

processes. Every interaction between an electron and a larger particle, whether ion, atom, or molecule, can ionize the particle, excite its electrons or bonds, split a molecule (dissociation), or none of the above. The relative likelihood of each of these is expressed by the collisional cross-section of these interactions, which is a function of the electron energy. Specifically, non-elastic collisions (i.e., excitation, dissociation, and ionization) are each most likely at a given electron energy, with ionization requiring the highest energies (Figure 6-1).

Thus, if the electric field increases, the electron energy would increase, leading to more ionization. The electrons freed by the ionization events could in turn accelerate and ionize more atoms, which could cause a higher current that grows exponentially, known as runaway ionization. To prevent runaway ionization, the electric field must be carefully controlled so that each electron causes, on average, one ionization before it recombines with an ion or exits the highest energy part of the plasma. The microplasma printer reported in this thesis achieves this with a current-controlled power source; other plasmas use a ballast resistor, a less expensive solution, but one that requires slightly more attention to maintain a constant current.

On the one hand, the electron energy must not get too high, lest runaway ionization occur. Therefore, neither the electron electrical mobility nor the electric field can be too high. On the other hand, in order to increase the sputter yield the ion energy must be increased. Consequently, given a certain electric field and ion electrical mobility, how can the ion energy be increased to increase the sputter yield without causing runoff ionization? This problem does not exist in traditional sputtering. Traditional sputtering occurs in a vacuum; as a result, an electron, no matter how energetic, has a high likelihood of escaping the plasma without ionizing a single atom because the gas density is low. Thus, even at very high electric fields and very high electric mobilities, runaway ionization does not occur.

This can be understood better by examining the Paschen curve, discussed in Chapter 1 (Figure 1-1). The Paschen curve describes the behavior of a plasma by examining the breakdown voltage as a function of the product of the pressure and interelectrode distance, which is directly proportional to the number of collisions that an average electron would undergo while traveling from one electrode to the other. When the pressure-interelectrode distance product is very low, the electron will collide with very few atoms, regardless of the electron energy. Thus, to maximize the impact of each collision, a very high voltage is necessary to ensure that each collision will lead to an ionization. Conversely, when that product is very high, the electron collides very frequently, and a high voltage is necessary to accelerate the atom sufficiently between collisions. In the intermediate area (near 1 $Torr \cdot cm$), the atom will have enough collisions to ionize efficiently, yet a high enough inter-collision distance to accelerate using a moderate electric field.

A traditional sputtering plasma operates at the left-hand side of the curve; the product of the pressure and the interelectrode distance is approximately $0.1\ \mathrm{Torr \cdot cm}$ [1:27]. Thus, the probability that a given electron would strike an atom while traveling from the cathode to anode, is approximately 0.1, as found by multiplying the number density ($\sim 10^{14}\ \mathrm{cm^{-3}}$) by the interelectrode distance (~ 10 cm) by a typical collisional cross section ($\sim 10^{-16}\ \mathrm{cm^2}$). Given that the number density is proportional to the pressure, the striking probability is proportional to the product of the pressure and the interelectrode distance. Thus, no matter how energetic the electron is, the chance that it will ionize an atom and produce another electron is low. (In fact, this low probability is the motivation for magnetron sputtering; by applying a magnetic field, the electron's traveling path can be greatly enlarged, increasing the chance of a collision.) However, increasing the voltage will not destabilize the plasma or even increase its current drastically; the electrons are all energetic enough; they are merely not colliding with the atoms that they need to ionize.

However, microplasma sputtering works at the right-hand side of the Paschen curve. The product of the interelectrode distance and the pressure is very high, approximately $100\ \mathrm{Torr \cdot cm}$. Thus, each electron, were it to travel from cathode to anode, would strike approximately 100 atoms on its path. Thus, if the electron ever gets the energy necessary to ionize an atom, it is highly likely that it will ionize an atom before it reaches the electrode. Energy, rather than collisionality, is the limiting factor in the ionization process. The breakdown voltage is so high because an electron will likely strike an atom before it builds up sufficient energy to ionize that atom, and that collision

will rob it of its energy. As a result, a high breakdown voltage is necessary, so that the electron has a chance of building up enough energy to ionize an atom in its inevitable collision.

As a result, at a high pressure-interelectrode distance product, higher voltages lead to a runaway effect, where each electron will ionize multiple electrons, leading to exponential current growth. The next two sections will describe a way around this problem, and outline methods to increase the ion energy without increasing the electron energy.

6.4. Simulation-Vetted Approaches to Increase Ion Energy in a Microplasma

COMSOL Multiphysics's Plasma Module was used to simulate a two-dimensional, axisymmetric atmospheric pressure argon plasma (Figure 6-2). Argon is used in these simulations because of its simpler plasma chemistry; unlike nitrogen, which is a mixture of molecular nitrogen and atomic nitrogen, with the possibility of excited molecular bonds or excited electrons, argon is a relatively simple monoatomic gas with fewer modes of excitation and no chemical bonds. This decreases the computational complexity of the simulation.

Three possible approaches to increase the ion energy were explored via simulations and experiments: (i) increase the current, (ii) increase the gas flow, and (iii) shape the electric field. The first solution explored was to increase the current; in the regime in which the microsputterer works (1-10 mA plasma current), the ion energy follows a power law in relation to the current, with an exponent equal to 0.40 (Figure 6-3). This can be understood by studying the number of ions per unit time that strike the cathode (current): the number of ions per unit of time that strike the cathode is proportional to the product of the ion velocity and the plasma density (ions per unit volume) near the cathode. Thus, to increase the current, either the ion velocity needs to increase, thereby increasing the ions' kinetic energy, or the plasma density needs to increase. However, merely increasing the plasma density, by Gauss's Law, also increases the electric field, making more energetic ions and electrons, and ultimately increasing the ion velocity. Thus, increasing the current of a current-controlled plasma requires an increase in the ion velocity (and energy), either directly or indirectly. In the regime in which we work, both factors (i.e., directly increasing the velocity and indirectly increasing the velocity by increasing the plasma density) are involved; simulations show that the exponent of the velocity's power law is 0.2, while the plasma density's power law's exponent is 0.92. Because the ion velocity has a power law relationship with the plasma density (found emperically), and the product of those two is proportional to the current, both velocity and plasma density have a power law dependancy on the current.

However, in practice, this effect is of limited value. The current cannot be drastically increased without melting the target wire; an increase from 2 mA to 3 or 4 mA is possible, but no more. Thus, the ion energy can be increased by 30%, but not doubled, as efficient microsputtering would require.

The second approach (increasing the gas flow) is a corollary of the plasma jet phenomena described in Section 4.5. A gentle gas flow drives the excited neutral atoms away, forcing the electrons to ionize atoms in one step, rather than first exciting them, to then ionize the excited

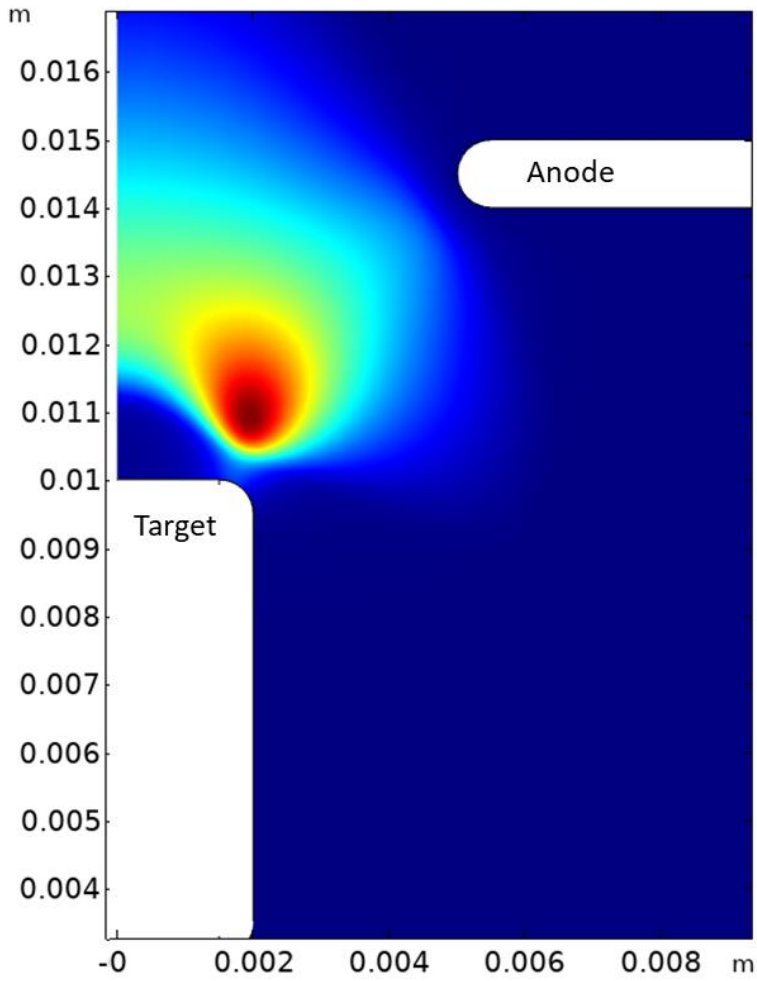

Figure 6-2. Cross-section of axisymmetric plasma. The ion density is shown in color, with the red area signifying the most ionized part of the of plasma. The model is rotated about the axis on the left.

atoms. Thus, in the presence of a gentle gas flow, a higher electric field is necessary to sustain the plasma, and thus, the higher electric field leads to higher ion velocity. This too is shown experimentally to be useful, but only to a small degree.

The third possibility explored in order to increase the ion energy in the plasma is to drastically increase the electric field, but in a very small region. This is done with "fringing", exploiting the extremely high electric fields near a sharp corner. Simulations show that extremely high electric fields and ion velocities are present very close to these sharp edges (Figure 6-4); however, the regions in which these high electric fields exist are so small that they do not lead to

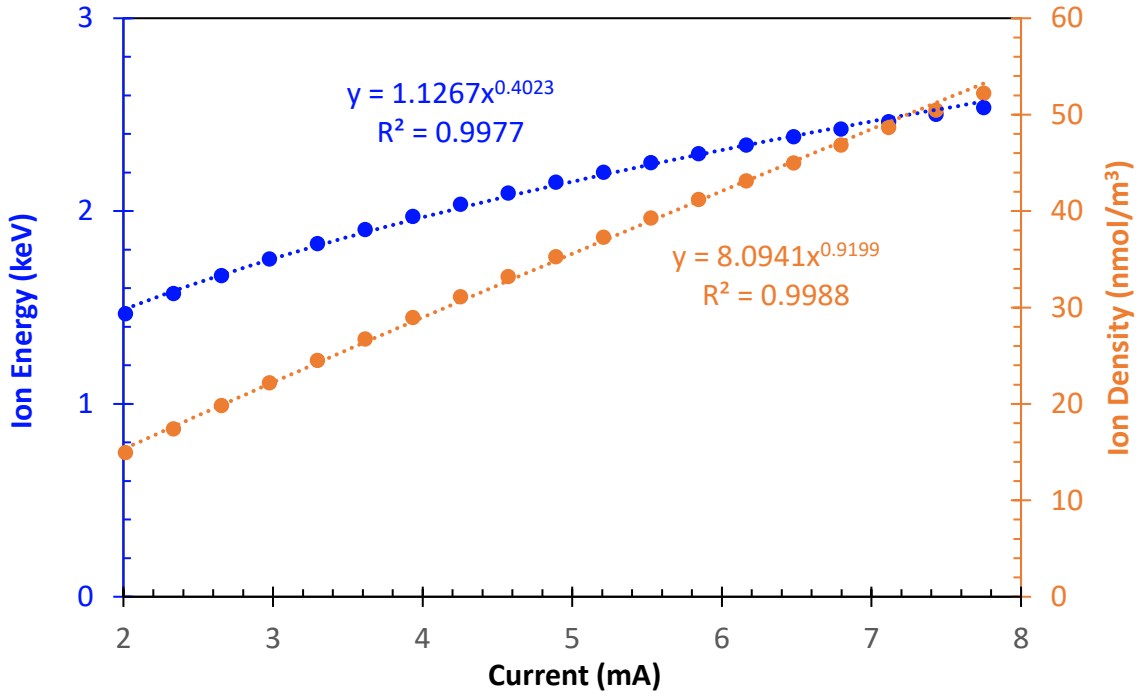

Figure 6-3. Density and average energy of ions very close to the target wire as a function of the total current. As the current increases, both ion density and ion energy increase, following a power law. However, because the ion energy only depends weakly on the current, a higher current cannot increase the ion energy of our microplasma sufficiently. The product of ion velocity and ion density is nearly proportional to the current.

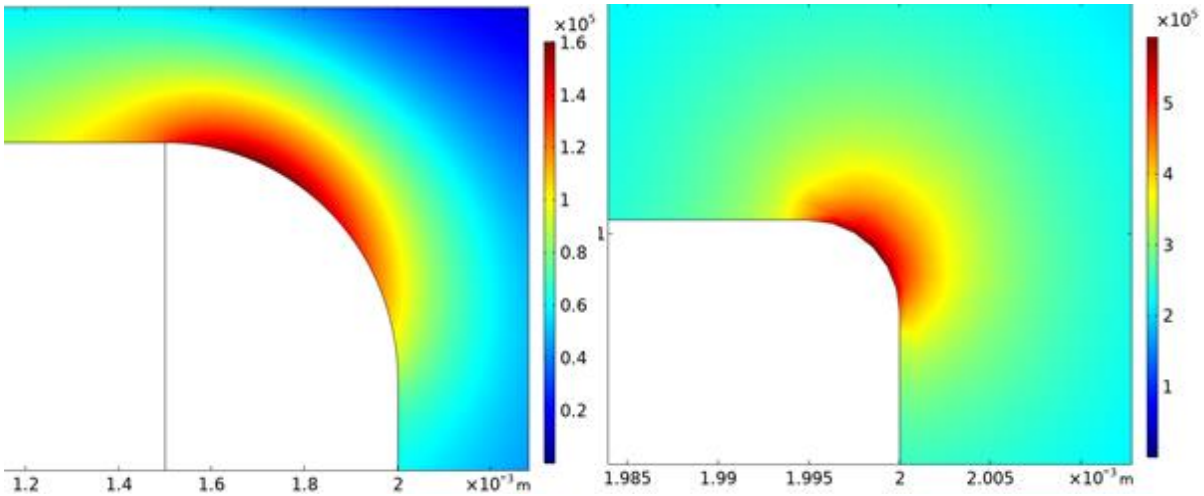

Figure 6-4. Ion velocity (in m/s), using a target with a 500 µm (left) and 5 µm (right) radius corner. Due to fringing, the sharp corner (right) produces a plasma that has an ion energy a threefold compared to the less sharpened corner's plasma. Unfortunately, sputtering quickly depletes such sharp features. Note the scale; the right image is of a much smaller area.

runaway ionization. Nonetheless, in practice, sharp corners are worn away by ion bombardment, hence any effects are not sustained.

6.5. Using a Mixture of Gases to Increase Ion energy in the Plasma

The argon plasma simulations discussed in Section 6.4 do not suggest an approach that drastically increases the ion energy. However, a mixture of gases, namely a gas comprised mostly of nitrogen mixed with a small fraction of argon, provides such possibility. This section will describe the different properties of monatomic and diatomic gases and the advantages and disadvantages of each. First, it will be demonstrated that diatomic gases support a higher electric field through examining collision cross-sections, the Townsend constants, and the ionization rate coefficient. Then, it will be demonstrated how monatomic gases sputter more efficiently.

Diatomic gases require a strong electric field to maintain an appreciable rate of ionization. In a diatomic gas, electron energy is dominated by the molecular bond within the gas. This bond can easily be excited (either vibrationally or rotationally) or broken, upon electron impact, with relatively low electron energies (Figure 6-1). Thus, for low energy electrons, most collisions will lead to excitation or dissociation. Furthermore, because excitation and dissociation are inelastic collisions (i.e., the electron and particle are left with less kinetic energy than they began), they are effective methods for preventing the electrons from gaining energy, even with a high electric field.

Consider the following calculations that will illustrate the energy-robbing effects of dissociation and the impact on ionization rates. An electron with 20 eV of energy has an ionization cross section with regard to molecular nitrogen of 32.7 Mb (0.327 $Å^2$) [6:4]. However, its dissociation cross section is 52 Mb [6:5]. Thus, it has over 150% the probability to dissociate a molecule than to ionize it. At lower energies, such as 16 eV, the difference between ionization and dissociation is more pronounced: at such energy, the ionization cross section is 1.3 Mb, while the dissociation cross section is 20 Mb. Thus, at low electron energies, electrons are more likely to dissociate a nitrogen atom than to ionize one, and the dissociation—an inelastic collision, robs the electron of energy. This is particularly effective in dense plasmas, where an electron will collide with atoms several times as its energy increases [6:6]; a collision is likely between the time that the electron has enough energy to effectively dissociate a nitrogen molecule and the time that the electron has enough energy to ionize a molecule.

The cross-section of excitation of the molecular bonds is even higher (Figure 6-1) at low energies. These collisions will rob electrons of energy before they reach the higher energies at which ionization is possible, unless the electric fields are very strong. Thus, the presence of molecular nitrogen keeps the rate of ionization low, even in strong electric fields.

In contrast, monatomic gases only have two inelastic electron impact reactions: electron excitation (i.e., raising an electron to a higher energy level) and ionization. Thus, in a purely monatomic plasma, electrons can (relatively) easily gain several eV of energy before they risk losing it to an inelastic collision. Thus, for a given electric field, electrons in a diatomic plasma will have much lower energies and much lower ionization rates than electrons in a monatomic

plasma. Equivalently, for a given ionization rate, a diatomic plasma will have a much higher electric field than a monatomic plasma.

The difference between nitrogen and argon is evident while examining the Townsend coefficients of the gases. As described in Chapter 1, the breakdown voltage (i.e., the bias voltage necessary to spark a plasma) is a function of the product of the pressure and interelectrode distance (pd), following the formula

$$V = \frac{Bpd}{ln(Apd) - ln\left(ln\left(1+\frac{1}{\gamma_0}\right)\right)}, \tag{6-4}$$

where pd is the aforementioned product, γ_0 is the secondary electron emission coefficient (which can be neglected for large pd, as in our case), and A and B are constants of the gas, known as the Townsend coefficients. It has been shown that both of these constants depends on the inelastic cross-sections for electron impact [6:7]-[6:11]; the higher the inelastic cross-sections, the higher B, and the higher the electric field needed to accelerate the electrons before they lose energy to inelastic collisions. Nitrogen has a very high breakdown voltage as compared to argon (Figure 1-1), further supporting that claim that nitrogen, overall, has higher inelastic cross-sections.

Gases with a high breakdown voltage are referred to as dielectric gases; other choices are highly toxic or have toxic byproducts (e.g., CO_2, SF_6, and many fluorocarbons) and are thus unsuitable for a sputterer open to the environment. Thus, in our microplasma sputterer air is used as dielectric gas. Although certain hydrocarbons may work better [6:7], they too are not suitable for an open-air environment.

The difference between monatomic and diatomic gases can also be seen by examining the ionization rate coefficient (a measure of the rate of ionization for a given electron and neutral atom density) for a given reduced electric field. For argon, the ionization rate coefficient becomes meaningful ($>10^{-19}$ m^{-3} s^{-1}) at 30 Td (800 kV m^{-1} at atmospheric pressure), while for nitrogen, a reduced electric field of 120 Td (3.2 MV m^{-1} at atmospheric pressure) is necessary [6:8].

Thus, it is clear that molecular nitrogen requires (and can maintain) a much higher electric field for a given rate of ionization, as compared to argon. However, although molecular nitrogen is valuable in keeping the electric field high and the rate of ionization low, it is not suitable for sputtering. Monatomic gases are far more effective at sputtering.

Let us imagine, by way of illustration, that the electric field near the cathode is 200 Td (26.8 MV m^{-1} at atmospheric pressure). Let us furthermore assume that sputtering is driven by the most energetic atoms, with an energy five times the average [6:8],[6:9],[6:12]. At those energies, an ion (whether nitrogen or argon) will have an energy of approximately 70 eV [6:9]. Even so, the nitrogen will dissociate before it reaches the surface of the target, losing 9.75 eV in the dissociation and splitting the remainder of its kinetic energy between the two nitrogen atoms [6:13]. Thus, each nitrogen atom will strike the surface with a paltry 30 eV. At these energies, the nitrogen atoms each have a sputter yield of 0.002 when sputtering gold (leading to a total sputter yield of 0.004

gold atoms per nitrogen molecule), while the argon, with the full energy of 70 eV, has a sputter yield of 0.226, almost two orders of magnitude higher [6:14]. Thus, for a given electric field, argon is much more effective sputterer than argon.

We can combine the advantages of these two kinds of gases (i.e., nitrogen, a diatomic gas, and argon, a monatomic gas) by combining the two gases. As long as the fraction of nitrogen in the sputtering plasma is high enough to drain energetic electrons of their energy through the excitation of molecular bonds and dissociation of molecules, a high electric field can be maintained without achieving runaway ionization. The small fraction of argon in that mixture, meanwhile, will be energetic enough to sputter effectively. Thus, the nitrogen preserves the electric field, while the argon is used for the actual sputtering. In other words, one can sputter effectively at energy levels typical for a **nitrogen** plasma, provided we sputter with **argon** in that nitrogen plasma.

A similar effect was previously reported for a Cu microplasma sputterer, although without explanation [6:15]. Researchers found that adding a small amount of (diatomic) hydrogen to an argon plasma increased the plasma voltage and improved the electrical conductivity (to 50X bulk resistivity). According to the conclusions of this thesis, these phenomena can be explained. The diatomic gas forced a higher plasma voltage due to the excitation of the diatomic bond; the higher voltage lead to higher ion energy and a larger nanoparticle-producing plasma, which according to the conclusions of Chapter 5, improved the electrical conductivity.

6.6. Experimental Validation of Increasing Ion Energy using a Gas Mix

Using a mix of molecular nitrogen and argon, the yield of gold sputtering can significantly be improved. The microsputterer at MIT Lincoln Laboratory uses a calibrated MFC (MKS MF1C, 500 sccm Ar) to control the flow of argon. A set amount of argon is mixed with air (4.5 slm) and flowed through the outer tube (see Chapter 2). A plasma is struck; the plasma voltage and gold deposition rate are recorded. As the theory explained in Section 6.5 suggest, a mixture of argon and air, with as little as 5% argon, maintains a high plasma voltage (due to the high air content), while also sputtering at twice the rate of air alone (due to the argon content) (Figure 6-5). Further investigation into the exact ideal mixture might yield even better results.

More importantly, using this approach, new materials can be sputtered. In an air-only plasma, it is very difficult to sputter aluminum; it is only possible at high powers (>4 mA), with long deposition times (>10 minutes), and for very thin films (< 10 nm). However, by adding 5% argon to the plasma gas mixture, it is possible to reliably sputter aluminum at a deposition rate of 1 Å/s. This is significant because the aluminum readily reacts with the oxygen in the high-energy, high collisionality plasma to become alumina (Al_2O_3)—a high-k dielectric (Figure 6-6). SEM microscopy (Zeiss 1525 SEM) shows a collection of very small (~10 nm) nanoparticles coalescing into a single film (Figure 6-6). These nanoparticles are significantly smaller than those described in Chapter 4 due to the relatively slow rate of aluminum sputtering; there are not enough aluminum atoms in the plasma to form 100 nm nanoparticles.

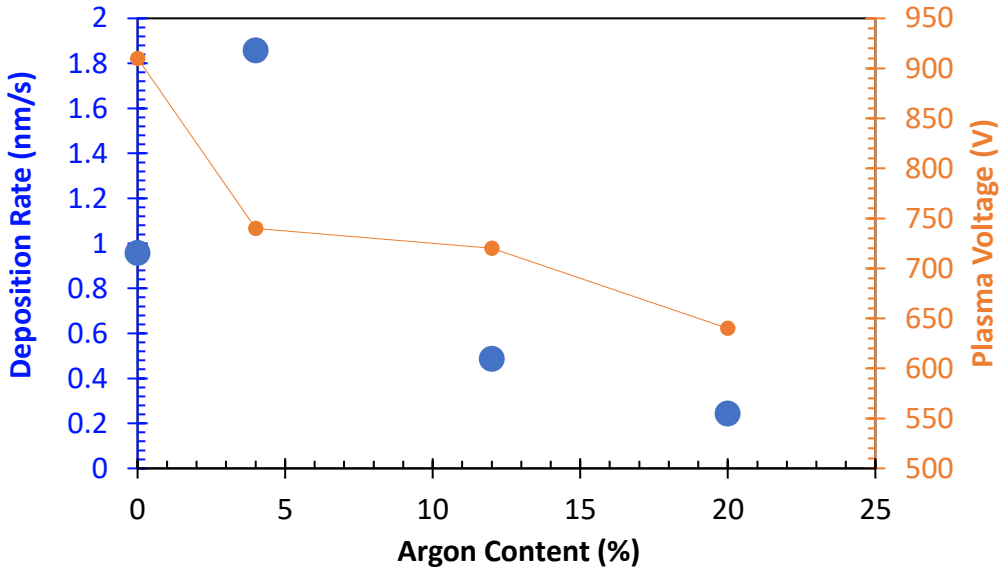

Figure 6-5. Deposition rate and plasma voltage versus argon content.As expected, the increase in argon decreases the plasma voltage. Despite this, a small amount of argon is helpful in increasing the deposition rate, dude to argon's ability to sputter more effectively than the diatomic species of air.

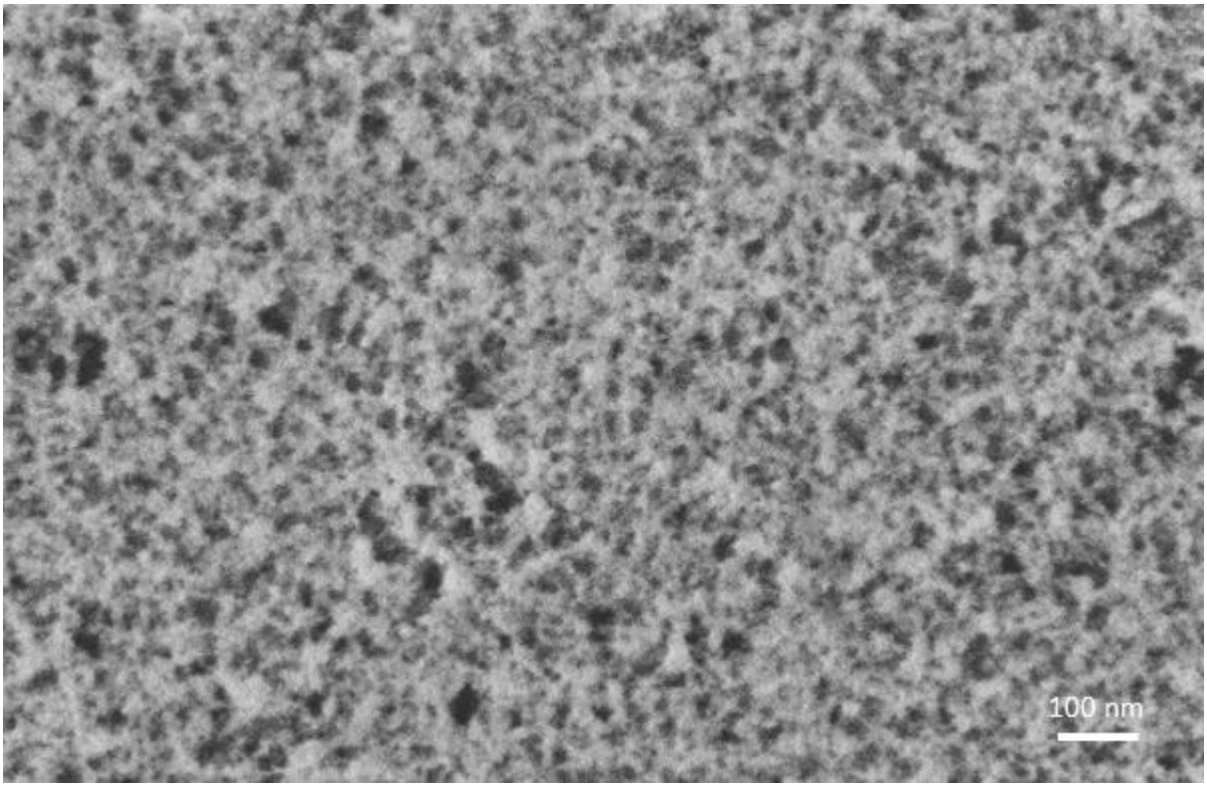

Figure 6-6. An SEM micrograph of the alumina. The alumina is clearly porous on the nanoscale, but the film is continuous. The pores are approximately 5 nm in diameter.

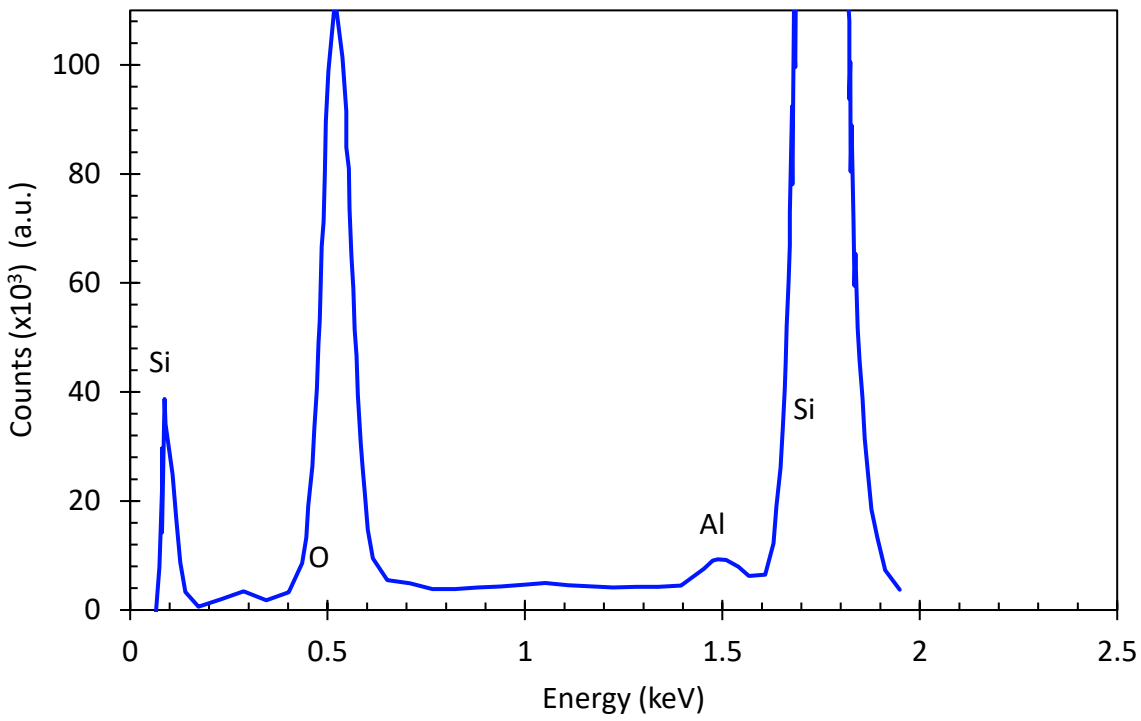

Figure 6-7. EDX results from an alumina deposit on a SiO_2-coated silicon wafer. The silicon, oxygen, and aluminum peaks are all clearly visible. Because of the thinness of the alumina, the aluminum peak is shorter, but nonetheless clearly present.

The alumina film is shown through EDX (JEOL JSM-6010LA) to clearly contain aluminum (Figure 6-7). Additionally, the aluminum to oxygen ratio of the sputtered material is found to be 1:2.05. This was calculated by comparing the oxygen content of oxide-coated silicon to a nearby spot with an alumina film above the oxide. Similarly oxygen-rich alumina (1:1.95 ratio) has been found when sputtering in an oxygen rich (10% oxygen) atmosphere at low pressure [6:16]. The electrical properties of the film are nearly identical with traditionally manufactured alumina, as Chapter 8 will describe. The proof-of-concept demonstration of devices fully microsputtered in gold and alumina (a capacitor) is reported in Chapter 8.

6.7. Conclusion

This chapter reports various approaches for increasing the ion energy in a microplasma, with the intention to significantly increase the yield and volumetric deposition rate. The high collisionality of a microplasma precludes strong electric fields, and, as a result, the sputtering ion energy is too low to sputter as effectively as in the standard (vacuum) case. Approaches such as increasing the current, flow, or shaping the target to serve as a field enhancer only provide modest/temporary improvements. Instead, the chapter demonstrates that an argon-nitrogen mixture greatly boosts the ionization and sputtering processes: the diatomic nitrogen allows for a high electric field, while the argon is stable enough to sputter effectively. The efficacy of the

proposed solution is demonstrated in the deposition of gold at twice the deposition rates previously obtained, and in the deposition of alumina using an aluminum target—yielding a dielectric material of great interest for printable electronics.

To the best of our knowledge, this is the first study that proposes an explains an appropriate gas mix for atmospheric pressure plasmas to obtain high sputtering yield. Traditionally, sputtering has been done in vacuum, while atmospheric pressure plasmas have had low ion energy. Now that a method for efficient atmospheric pressure sputtering has been found, more work, both theoretical and experimental, can be done on the ideal mixture of gases for each set of sputtering conditions, (i.e., sputtered material, current, and voltage), leveraging the discoveries of this chapter to not only add to our understanding of plasmas, but to further allow atmospheric pressure microsputtering to become a viable manufacturing technique for agile electronics and other low-temperature devices.

6.8. References

[6:1] Cosby PC. Electron-impact dissociation of nitrogen. The Journal of Chemical Physics. 1993 Jun 15;98(12):9544-53.

[6:2] Phelps database, www.lxcat.net, retrieved on May 30, 2021. Based on Phelps AV, Pitchford LC. Anisotropic scattering of electrons by N_2 and its effect on electron transport. Physical Review A. 1985 May 1;31(5):2932.

[6:3] Seshan K, editor. Handbook of thin film deposition processes and techniques. William Andrew; 2001 Feb 1.

[6:4] https://physics.nist.gov/cgi-bin/Ionization/table.pl?ionization=N2, retrieved on March 10, 2021

[6:5] Cosby PC. Electron-impact dissociation of nitrogen. The Journal of Chemical Physics. 1993 Jun 15;98(12):9544-53.

[6:6] Seaver AE. Ionization through a sequence of collisions. Journal of Electrostatics. 1995 Jul 1;35(1):113-24.

[6:7] Heylen AE. The relationship between electron—molecule collision cross-sections, experimental Townsend primary and secondary ionization coefficients and constants, electric strength and molecular structure of gaseous hydrocarbons. Proceedings of the Royal Society of London. Series A: Mathematical, Physical and Engineering Sciences. 2000 Dec 8;456(2004):3005-40.

[6:8] Haefliger P, Franck CM. Detailed precision and accuracy analysis of swarm parameters from a pulsed Townsend experiment. Review of Scientific instruments. 2018 Feb 23;89(2):023114.

[6:9] Maiorov SA. Ion drift in a gas in an external electric field. Plasma Physics Reports. 2009 Sep;35(9):802-12.

[6:10] Lewis TJ. Electron energy distributions in uniform electric fields and the Townsend ionization coefficient. Proceedings of the Royal Society of London. Series A. Mathematical and Physical Sciences. 1958 Mar 11;244(1237):166-85.

[6:11] Crowe RW, Bragg JK, Devins JC. A Semiempirical Expression for the First Townsend Coefficient of Molecular Gases. Journal of Applied Physics. 1955 Sep;26(9):1121-4.

[6:12] Lisovskiy V, Booth JP, Landry K, Douai D, Cassagne V, Yegorenkov V. Electron drift velocity in argon, nitrogen, hydrogen, oxygen and ammonia in strong electric fields determined from rf breakdown curves. Journal of Physics D: Applied Physics. 2006 Feb 3;39(4):660.

[6:13] Steinbrüchel C. On the sputtering yield of molecular ions. Journal of Vacuum Science & Technology A: Vacuum, Surfaces, and Films. 1985 Sep;3(5):1913-5.

[6:14] Matsunami N, Yamamura Y, Itikawa Y, Itoh N, Kazumata Y, Miyagawa S, Morita K, Shimizu R, Tawara H. Energy dependence of the yields of ion-induced sputtering of monatomic solids. Institute of Plasma Physics. 1983 Sep. Nagoya University, Japan.

[6:15] Zhao P, Zheng W, Watanabe J, Meng YD, Nagatsu M. Highly Conductive Cu Thin Film Deposition on Polyimide by RF-Driven Atmospheric Pressure Plasma Jets under Nitrogen Atmosphere. Plasma Processes and Polymers. 2015 May;12(5):431-8.

[6:16] Segda BG, Jacquet M, Besse JP. Elaboration, characterization and dielectric properties study of amorphous alumina thin films deposited by rf magnetron sputtering. Vacuum. 2001 May 25;62(1):27-38.

Chapter 7 – **Gold Coated Nanowires for RF Interconnects**

7.1. Introduction

Until now, the microsputterer hardware was introduced and improvement in the material properties of the sputtered films have been reported. The remainder of this thesis will be devoted to demonstrations of the technology. This chapter describes the coating of nanowires for RF interconnects. This work was part of a collaboration with Charles Draper Laboratory and is published in the proceedings of IVNC 2020 [7:1]. The chapter motivates the research by explaining the need for conductive nanowires, describes a method of coating nanowires with gold without needing a vacuum, and characterize the films' relevant properties (i.e., mechanical and electrical).

7.2. Motivation

Wires transmit electrical signals. These signals could be DC, low-frequency AC, or high-frequency AC. For DC and low-frequency AC signals, the choice of wire is simple. Every wire has a resistance, which varies inversely with its cross-sectional area. The longer the distance that must be travelled and the lower the necessary resistance, the thicker the wire must be. However, high frequency signals cannot be transmitted with minimal loss simply by using thicker wire. This is due to the skin effect. If an alternating current flows along a wire, the induced magnetic field drives the current out of the center of the wire, concentrating it in the outermost "skin" of the wire. Since the current only flows through a small fraction of the wire, only that small fraction contributes to the conductance, and the resistivity can be unacceptably high, even for thick wires. Specifically, the skin depth of the wire is calculated as

$$\sqrt{\frac{\rho}{\pi f_0 \mu}} \tag{7-1}$$

where ρ is the resistivity, f_0 is the signal frequency, and μ is the magnetic permittivity. As Figure 7-1 shows, for frequencies greater than 4 MHz the skin depth can be less than a 40-gauge gold wire's radius (39 μm; 48 Ω/m). As a result, for high-frequency signals, the majority of a wire is useless and the resistivity is high. One common solution is to use Litz wire, a bundle of narrow wires, each insulated from the others, to carry the signal. The strands pass from the center of the bundle to the perimeter and back again, so that no single strand is the outermost wire that carries the entire current. The insulation prevents the current from migrating to the perimeter. Instead, the current is evenly distributed among all the wires. Within each strand, the current is pushed to the outermost skin depth.

However, this technique is only useful if each strand that comprises the Litz wire is smaller than the skin depth. For higher and higher frequencies, the strands must be made smaller and smaller, and, consequently, more and more strands must be included to have the desired total thickness.

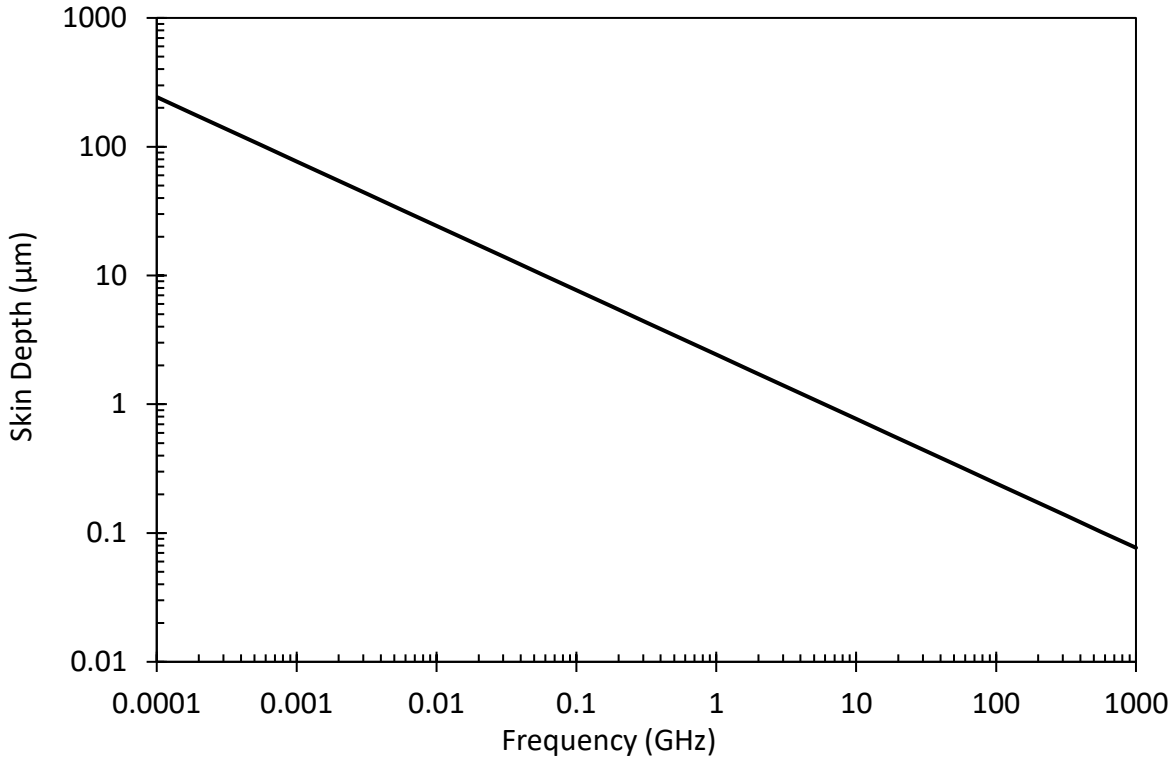

Figure 7-1. Skin depth of gold as a function of frequency. For frequencies greater that 10 GHz, the skin depth is submicron.

Manufacturing conductive wires is feasible for individual strands with a diameter larger than 2 µm, which can be easily manufactured by drawing. Traditionally, wires are drawn to their desired thickness by forcing thicker wires through a mold; the ductile nature of metal allows the wire to reshape itself to fit the narrower mold, and a uniform, narrow wire is formed. However, for narrower wires, suitable for > 6 GHz signals, metal is no longer ductile at such dimensions, and an alternative must be found.

Past research has explored the possibility of using electrospinning to produce fibers, which could then be coated to make wires. Electrospinning uses strong electric fields to create narrow strands of polymers; via whipping and stretching, the polymers cure into an extremely narrow and uniform nanofiber—sometimes as small as 50 nm diameter [7:2].

Unfortunately, electrospun nanofibers are not highly electrically conductive. Instead, they must be coated with a conductive shell, before being encased in a dielectric and twisted into a Litz wire. One method of coating the fibers involves traditional sputtering in a vacuum chamber. However, this is time- and labor-intensive; each batch of electrospun nanofiber must be brought to vacuum, sputtered, turned over, and then the underside must be coated again. This coating is then used as a seed layer for electroless coating.

7.3. Results

We demonstrate a room-temperature sputter coating method that is compatible with atmospheric pressure. Due to the scarcity of the electrospun nanofibers that our collaborators were using for the packaging of the Litz wires, this method is demonstrated on Kevlar fibers (5 μm diameter). A bundle of Kevlar fibers is attached to a metal frame (Figure 7-2). A gas jet (50 m/s) in each inner and outer gas channel carries microsputtered material (2 mA) to the bundle of wires; the printhead is rastered over the bundle of fibers for 10 minutes, coating the 10 mm-long fibers.

The coated fibers were characterized using an SEM microscope (JEOL JSM-6010LA). EDX measurements confirm that the wires are coated with gold; SEM confirms that the gold is a nearly uniform coating, coating both top and underside of the wire with an approximately 300 nm thick film—even though the deposition was conducted on one direction (Figure 7-3). This is in stark contrast to traditional sputtering, in which sidewall and underside coating is severely lacking. We can study this by investigating the path that a jet flow takes around a cylinder, such as a Kevlar fiber. The Reynolds number of the flow, assuming a Kevlar wire of 5 μm diameter and a gas flow of 50 m/s, is 13 [7:3]; this is low enough that the viscous effects dominate the fluid flow, and the plasma surrounds the underside of the wires as well as it does the upper side of the wires; diffusion then carries the sputtered material onto the underside of the wire, just as it carries the sputtered material onto the upper surface. A smaller wire would have an even lower Reynolds number, and thus also have underside coating. In other words, material transport across the entire surface is attained.

Additionally, this coating is mechanically sound. When the fiber is cut with a pair of scissors, the coating deforms due to the shear stress, but remains intact as it separates from the film (Figure 7-4). This indicates high density and good coverage, which are useful if the film is to be used as a seed layer for an electroless process.

Suspending wires and then coating them, rather than printing on a flat substrate, also gives information with regard to the speed of the printer. Although typical speeds when printing on a flat substrate do not exceed 1 nm/s (Chapter 6), the wires' films grow at 3 nm/s. This is due to the relatively free flow of the fluid; as we discussed in Chapter 3, when the fluid impinges on a flat substrate, it spreads out and some of the sputtered material does not reach the substrate, or minimally, does not reach the part of the substrate directly under the flowing gas. However, in this case, because the fibers minimally interrupt the flowing gas, the flow is still in the "free flow" stage, and more of the sputtered material is deposited on the wires.

The coating is electrically conductive. Because the fibers are so small, it is not trivial to attach a lead to a single fiber and measure the conductance directly. Instead, conductive tape is attached to two ends of a bundle of fibers and fibers are cut by one. As each fiber is cut, the conductance of the bundle decreases, and, assuming that each cut fiber had identical conductance, the conductance per fiber can be calculated by noting how much the conductance decreases with each cut. This also allows us to estimate the number of fibers in the bundle (Figure 7-5). It is found

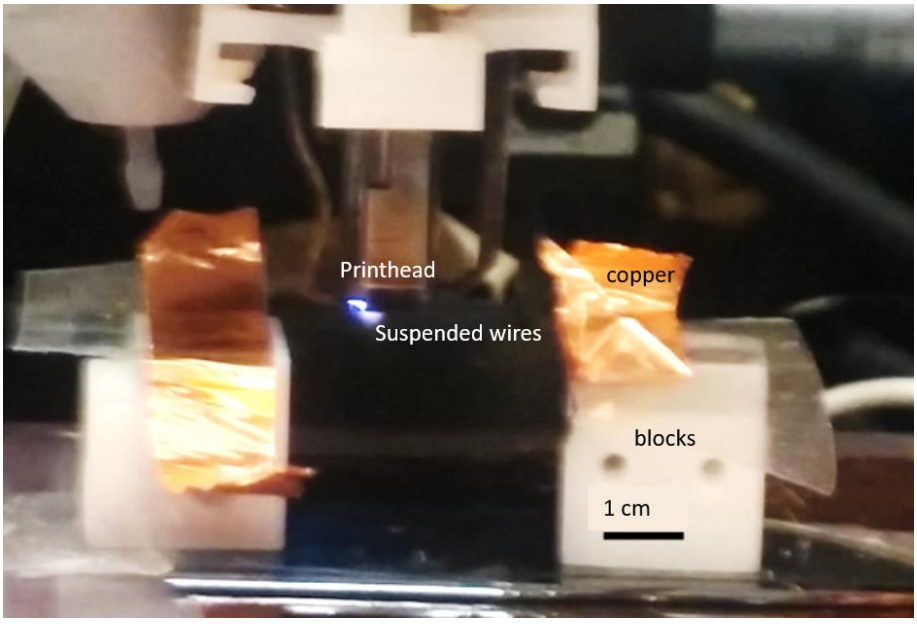

Figure 7-2. Photograph of setup. The microplasma printer is depositing a film on thin (invisible) wires, suspended between the two plastic blocks.

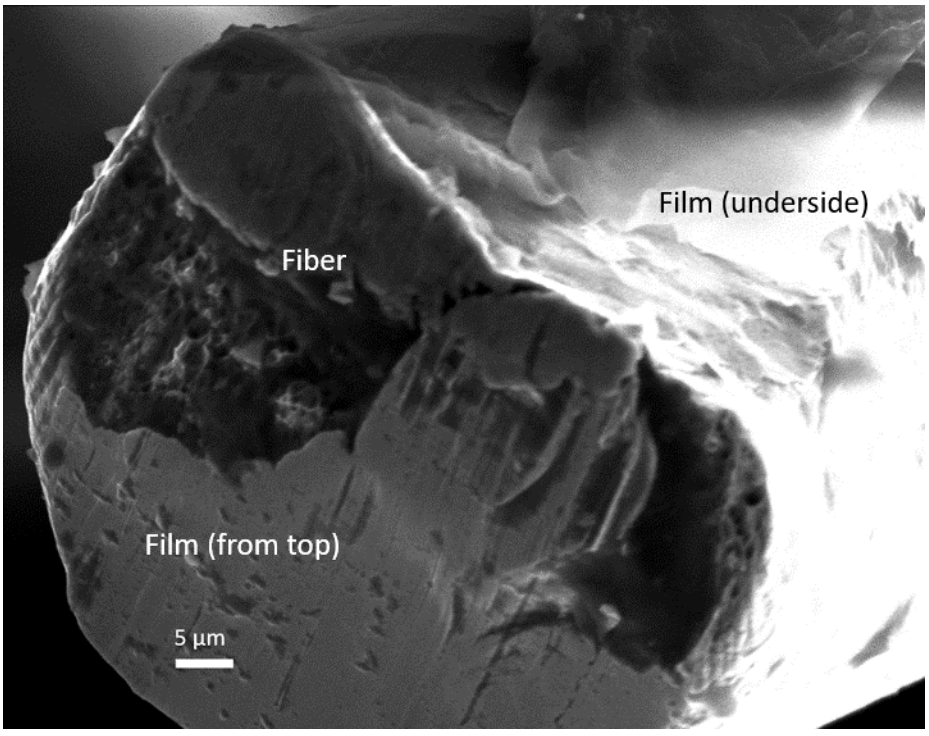

Figure 7-3. Micrograph of a cross-section of an 80 µm diameter steel wire, coated with gold. The underside of the wire (top of image) clearly has a continuous coating. The coating has deformed onto the cut side of the wire due to shear stress. The thicker steel wire is easier to image than Kevlar, but the same results are seen in Kevlar.

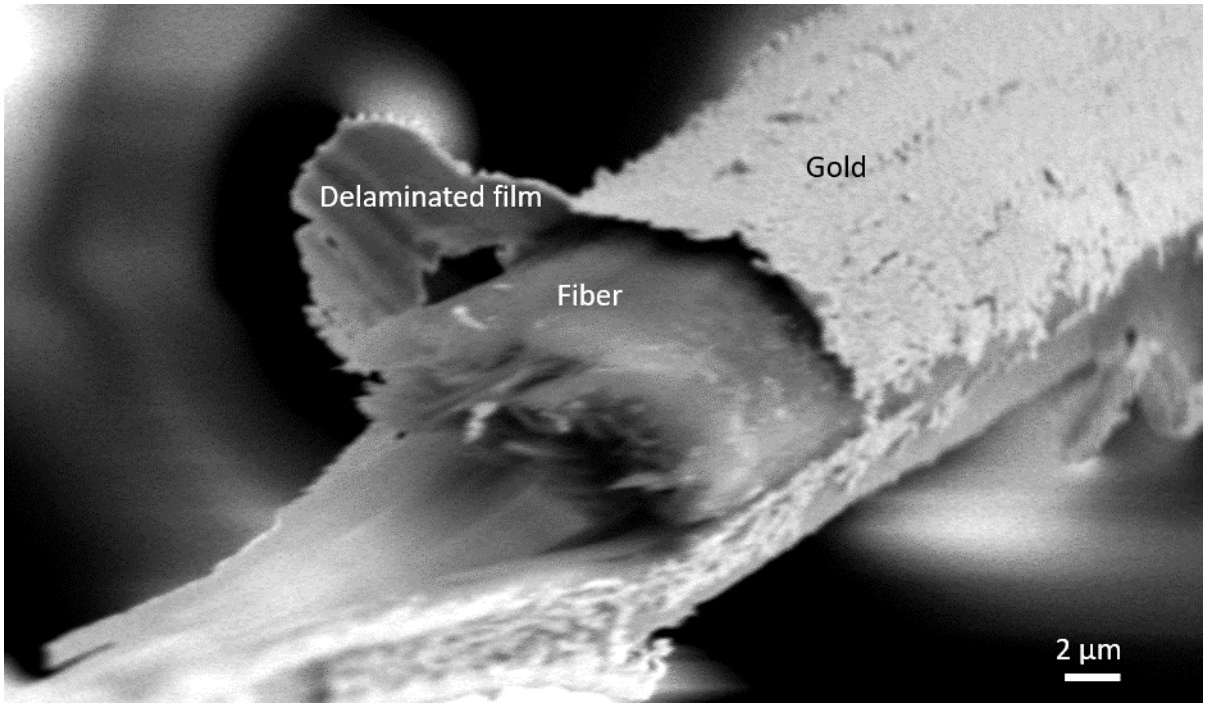

Figure 7-4. A micrograph of a Kevlar fiber. The shear stress of cutting the fiber peeled the gold coating off (above the fiber), but the coating remains intact, showing its mechanical strength. This micrograph also shows the thickness of the coating as 300 nm.

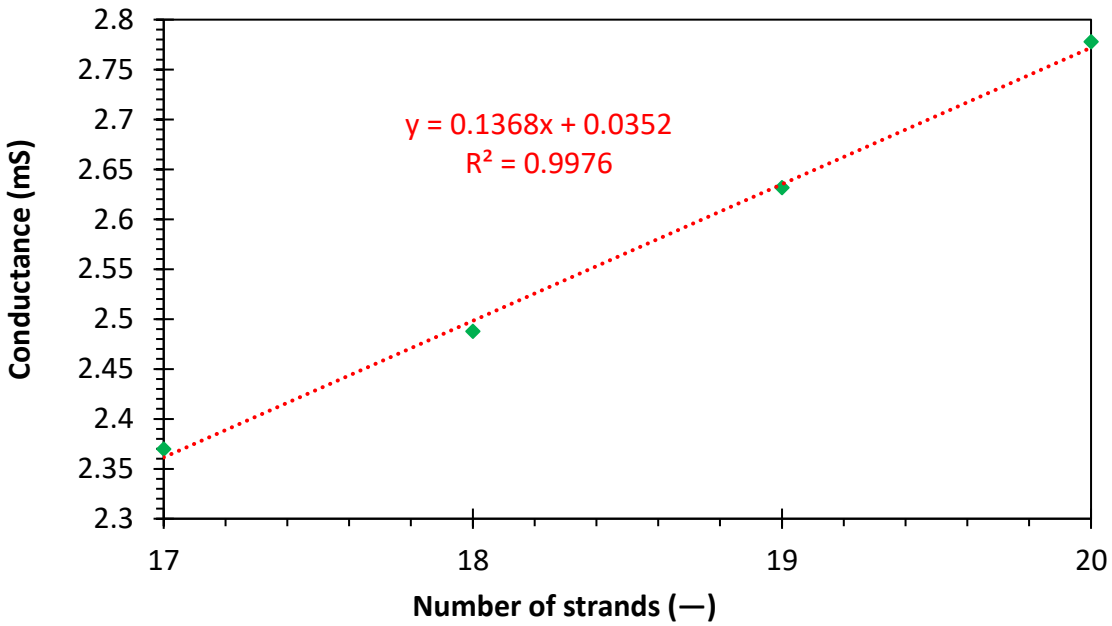

Figure 7-5. Dependence of conductance of Kevlar bundle on number of fibers in the bundle. By cutting the fibers one-by-one and fitting a best-fit line to the resultant conductance, the conductance of each individual fiber can be extracted without knowing directly how many fibers were in the bundle.

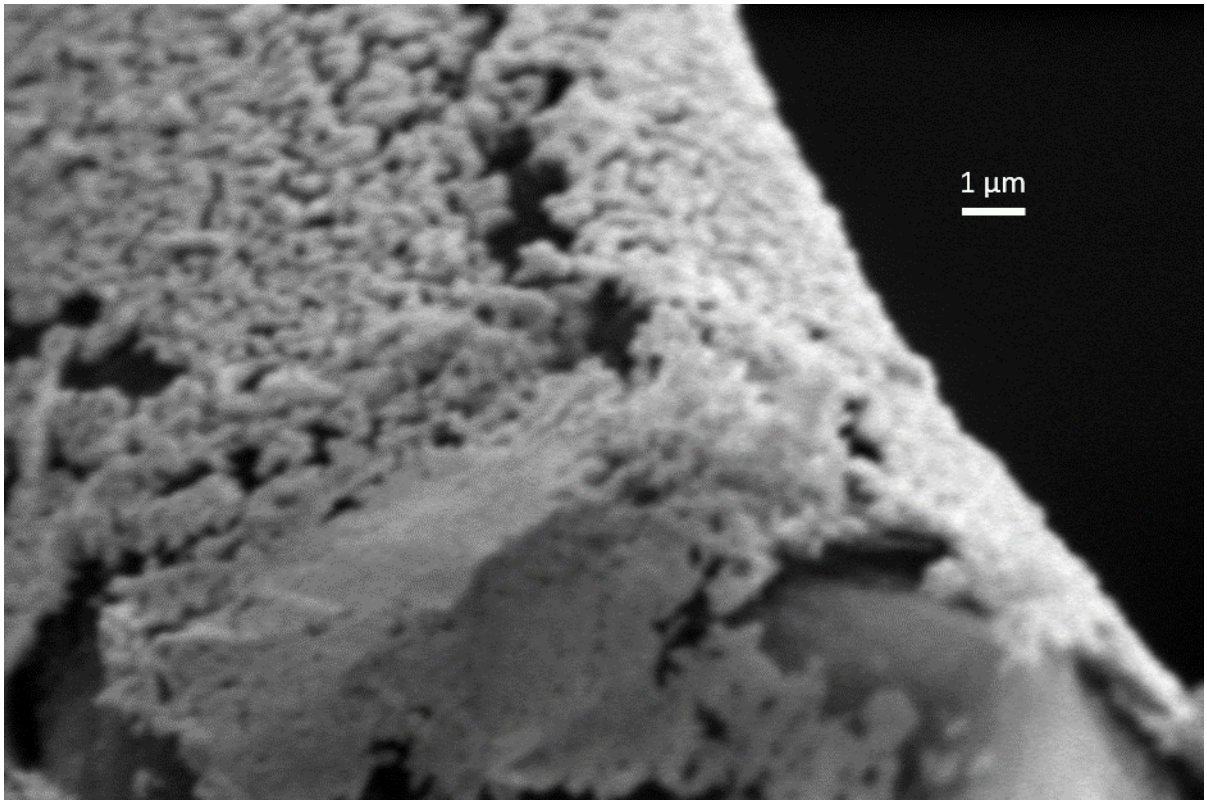

Figure 7-6. A micrograph of a gold-coated Kevlar fiber. The porous nanostructure of the wire, along with larger cracks due to the stress of cutting the wire, are visible. Although the fibers are conductive, they are much more resistive than bulk gold, due to the porous nanostructure.

that each fiber has a conductance of 137 µS, which means that the 500 nm thick film has a conductivity of 14 µΩ·m This would mean that the films are 600 times more resistive than bulk gold; because a bias could not be applied directly to the nonconductive Kevlar wire, the films are somewhat porous (Figure 7-6), as described in Chapter 4. Nevertheless, the minimal conductivity of the wires allows for the use of electroplating to coat the wires, with the gold coating serving as a seed layer.

Atmospheric sputtering of gold is suitable to produce as a seed layer for electroless plating or electroplating; those chemical methods could be used to deposit a dense, highly-conductive layer of metal quickly. If microsputtering was to be used as the sole coating for a bundle of nanofibers, roll-to-roll manufacturing methods would be necessary. A short length of a bundle of fibers would be coated without the benefit of a negative bias on the wires, much like our case. That length could then be attached to a negative bias. The bundle of fibers would be slowly passed under the microsputterer. As a thin film of sputtered gold built up on the bundle, the thin film would become negatively charged, and would attract denser films to attach themselves to the initial, porous films. This method would necessarily be slow, as any method involving the microsputterer is, but it would lead to dense, highly conductive films produced in a single step.

7.4. Conclusion

In this chapter, the proof-of-concept use of the microsputterer to implement RF interconnects based on ultra-thin (5-µm diameter) wires is reported. The microsputterer can coat fibers, integrating itself in a non-vacuum manufacturing process. This is in stark contrast to traditional sputtering, which requires switching from atmospheric pressure (for the fiber production) to vacuum (for the coating) and rotation of the wires as the metal coating is applied. In the method described in this chapter, the coating covers both sides of the fiber in a single process due to the high collisionality of atmosphere that fosters mass transport across the surface. The coatings produced with this method are of high mechanical quality and sufficient electrical quality; a step forward to improve the electrical conductivity is outlined.

7.5. References

[7:1] Kombluth Y, Velásquez-García LF, Ehrenberg I, Carter D, Russell KJ. Atmospheric microplasma-sputtered micro and nanowires for advanced THz interconnects. In 2020 33rd International Vacuum Nanoelectronics Conference (IVNC) 2020 Jul 6. IEEE.

[7:2] Couch AM. *A novel method for the production of microwires* (Masters dissertation, Massachusetts Institute of Technology), 2019.

[7:3] Espinosa-Gayosso A, Ghisalberti M, Ivey GN, Jones NL. Particle capture and low-Reynolds-number flow around a circular cylinder. Journal of Fluid mechanics. 2012 Nov 10;710:362-78.

Chapter 8 – **Fully-Printed Multimaterial Capacitors**

8.1. Introduction

This chapter reports the proof-of-concept demonstration of working, multi-material, microplasma-printed electrical capacitors. To the best of our knowledge, this is the first entirely-printed devices produced via microsputtering, and serves as an important milestone towards the maturation of microsputtering as a technology for manufacturing agile electronics. While most of this thesis was devoted to the development and characterization of a microsputtering process for gold for use as an electrical conductor, these capacitors also showcase the possibility to print high-quality dielectrics, printed using the same additive manufacturing technology. Dielectrics allow for the layering of interconnects, preventing signals from one interconnect from interfering with an intersecting trace.

The multimaterial head, first described in Chapter 2, which allows the use of two materials (e.g., aluminum and gold) in sequence, is also demonstrated in this chapter. The chapter first describes the fabrication of a capacitor. It will then describe the characterization of the capacitor, namely its response to both DC and AC signals. The DC response is shown to be typical of traditional alumina. However, the AC response includes the effect of the universal dielectric response, a commonly-found frequency dependence in the electrical behavior of heterogeneous dielectrics due to the porosity of the film. Based on data analysis, it is hypothesized that the microsputtered dielectric material is a mixture of alumina and small water-filled nanopores; a precedent in the literature of such film structure is found.

8.2. Fabrication of a Fully Microsputtered Capacitor

A structure of the fully-microsputtered parallel capacitor consists of two (7-mm long) gold lines, printed perpendicular to each other and intersecting at their centers (Figure 8-1). Between the gold lines is a (3-mm) square layer of alumina, which caps the bottom gold line at the point of intersection. The capacitor is printed on a silicon wafer with a 300 nm thermal layer of SiO_2 film. All parts of the capacitor use the combined innovations of Chapters 3 to 6: vat polymerization-printed FunToDo nozzles (1-mm wide aperture), -300 V bias voltage on the substrate, moderate gas flow (~4 slm), and 5% argon content. The area in which the two gold traces overlap was examined with an optical microscope and found to be 800 µm by 1.1 mm. The gold traces were printed by rastering the printhead 20 times at a speed of 50 µm/s with a total thickness of 150 nm, while the alumina patch was printed by coating a square 3 mm on each side for 120 minutes; the two stages moved at different speeds (80 µm/s and 110 µm/s) to produce a uniform coating pattern over the entire area. After the first gold line was deposited, the substrate was rotated to allow the dielectric cap and second gold line to be printed. The alignment was done with the use of reference marks.

After the dielectric and electrically conductive layers were deposited, thin copper wires (36 AWG, 127 µm diameter) are connected to the four ends of the gold imprints using conductive epoxy, to facilitate the electrical characterization of the devices.

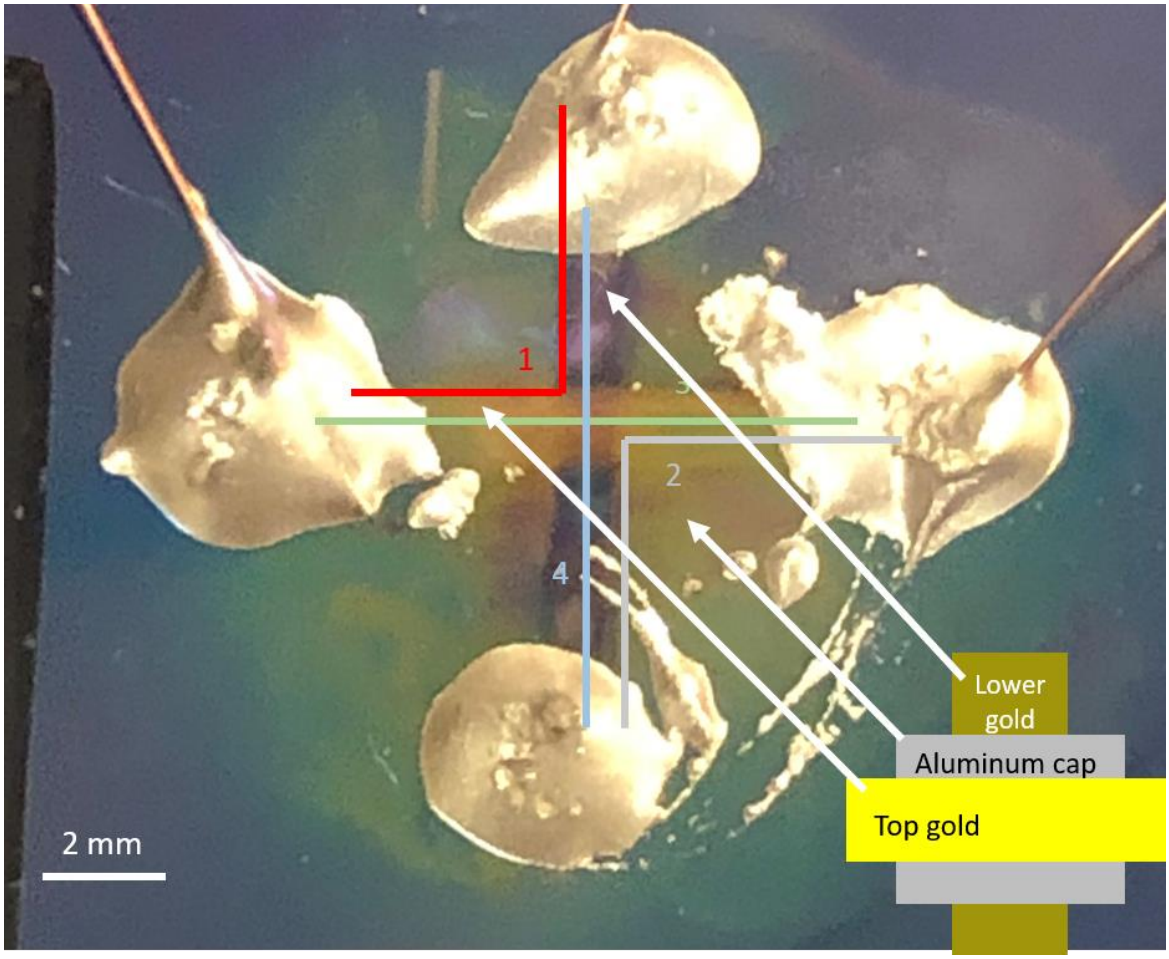

Figure 8-1. A photograph of a completed capacitor, consisting of a bottom gold trace (vertical), an alumina cap (center) and a top gold trace (horizontal). Conductive epoxy and copper wires are visible in three of the terminals of the gold traces (the copper wire at the bottom of the image was not installed for clarity). The colored lines represent the AC electrical measurements taken; to eliminate the effects of the gold traces on the frequency response, the impedance was measured by adding paths 1 and 2, subtracting 3 and 4 from that sum, and dividing by two. That eliminates the gold traces' contribution, while accurately capturing the alumina's electrical response. A schematic drawn in the lower right corner illustrates the parts and layout of the capacitor.

After the electrical characterization was complete, one of the capacitors was cleaved and an SEM was taken of its cross-section (Figure 8-2). From the metrology of the SEM, the alumina was found to be 35 nm thick.

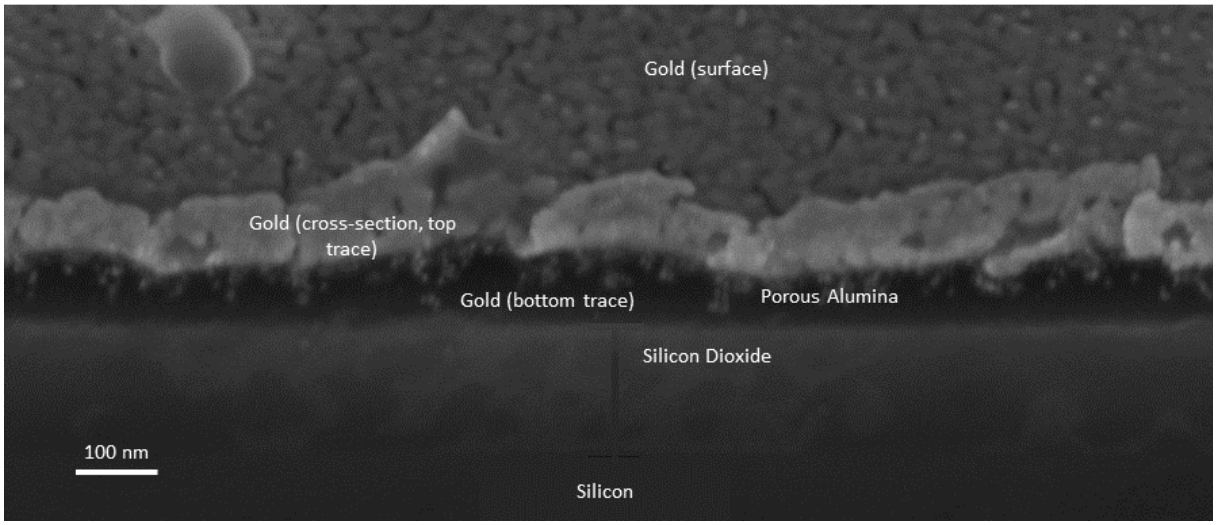

Figure 8-2. SEM micrograph of cross-section of the capacitor. The cross section is taken off-center from the center of the capacitor; as a result, the bottom trace is extremely thin. Nonetheless, the two gold traces, the porous alumina, the silicon dioxide, and the silicon are all visible

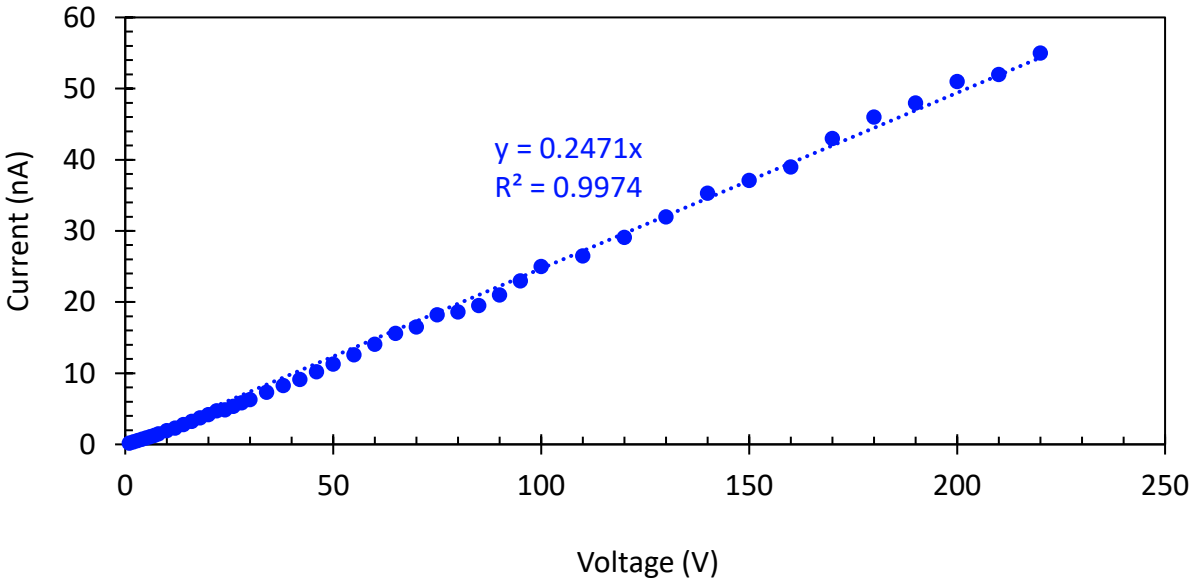

Figure 8-3. A DC IV characteristic of the microplasma-printed alumina capacitor before breakdown of the capacitor's DC response. The leakage current is minimal and linear, showing a resistance of 4 GΩ. The breakdown voltage of the film is equal to 220 V.

8.3. Breakdown Voltage and DC Response

To test the quality of the dielectric, a DC bias voltage was applied between the two gold traces and the current was measured with a Keithley 2657A power source. A 10 kΩ resistor was inserted in series to prevent damage to the power source. The breakdown measurement was taken

after all other electrical measurements; once the breakdown voltage was reached, the capacitor was no longer functional.

The resistance was found to be 4.05 GΩ (Figure 8-3). Given the alumina's thickness and the area in which the gold traces overlap, this suggests a resistivity of 1.0 X 10^{11} Ω·m. This is approximately 10% of the resistivity of bulk (crystalline) alumina and 10x the reported resistivity of amorphous alumina [8:1].

The capacitor's breakdown voltage was 220 V. Thus, the alumina has a dielectric strength of 6.2 GV·m^{-1}, which is fivefold the best results for bulk alumina reported thus far [8:2], and double the best results reported value for ultrathin (~1 nm) alumina films [8:3].

8.4. Electrical Characterization: Frequency Response

A Digilent Analog Discovery 2 USB oscilloscope was used to measure the frequency response of the dielectric film. To eliminate the response of the gold, measurements from four pairs of pads were taken and a linear combination of the results was taken to eliminate all but the alumina's response (Figure 8-1). The impedance was measured, divided into real and imaginary parts, and found to follow a power law dependency on the frequency over 5.5 orders of magnitude (10 Hz–5 MHz) (Figure 8-4). Knowing the dimensions of the capacitor, the permittivity was extracted from this response, and both real and imaginary parts (corresponding to reactance and resistivity, respectively) follow a power law where

$$\epsilon = \epsilon_0 \left(10.92 \frac{\omega}{\omega_0}^{-0.133} - 3.68i \frac{\omega}{\omega_0}^{-0.152}\right) \quad (8\text{-}1)$$

where ϵ_0 is the permittivity of free space, ω is the frequency of the AC signal, and ω_0 is a reference frequency, i.e., 1 Hz (Figure 8-5). It is notable that the exponents are nearly the same, making the elements of the impedance proportional; this is characteristic of the universal dielectric response. The imaginary permittivity, which corresponds to the ohmic loss of the material, is less than the real permittivity; this signifies that if the device were modelled as a resistor and capacitor *in parallel*, the capacitor would have the lesser impedance (in magnitude) at all frequencies, most of the current would flow through the capacitor, and the phase shift would be close to 90 degrees. (Conversely, if the device were modelled as a resistor and capacitor *in series*, the capacitor would have the greater impedance and would be responsible for most of the signal's behavior.) Thus, the device behaves primarily as a capacitor, albeit with a significant resistive loss.

The permittivity has real and imaginary parts (Figure 8-5). The real part is, by definition, inversely proportional to the reactance, while the imaginary part is inversely proportional to the AC resistance. At the low-frequency limit (10 Hz), the real part of the permittivity (i.e., the part which contributes to the impedance) is 8.0, which is within the range of reference values for alumina [8:4] for low-frequency measurements (i.e., 7–11). Many other reported measurements of permittivity, taken in the GHz range, are within the same range [8:4]–[8:8]. Thus, the behavior of the dielectric film at low frequency matches the known behavior of alumina. Combined with the metrology of Section 6.6, where the film was shown to contain aluminum and oxygen, we are

confident that this material is primarily made of alumina.

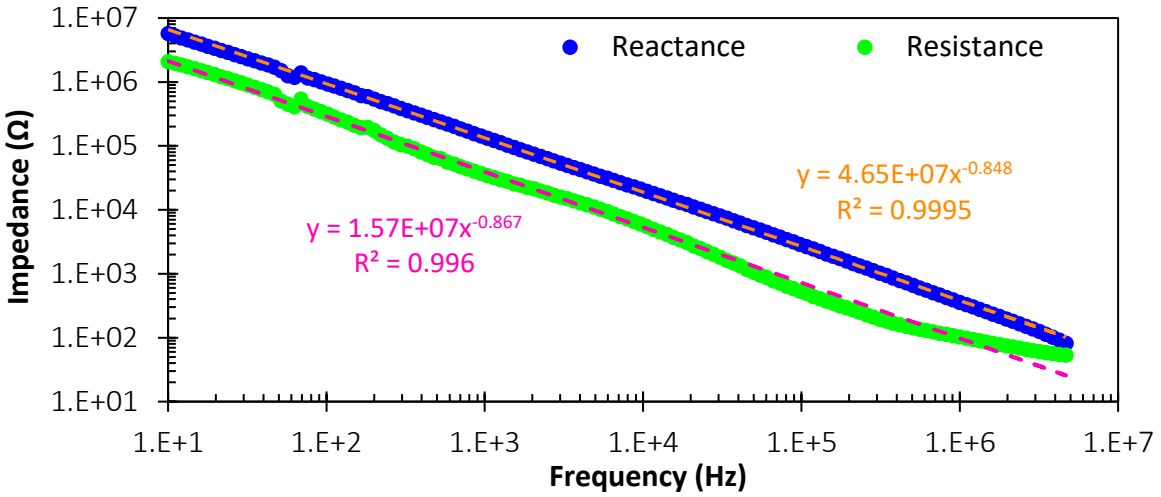

Figure 8-4. Frequency response of resistance and reactance of the device modelled as a resistor and capacitor in series. The reactance is larger than the resistance, signifying that the device is primarily capacitive. The power law, where both terms of the impedance have similar exponents, is typical of the universal dielectric response. The aberrations near 60 Hz are likely due to line voltage. The resistance diverges slightly above 1 MHz, as is typical for the universal dielectric response, which is limited to a given frequency range.

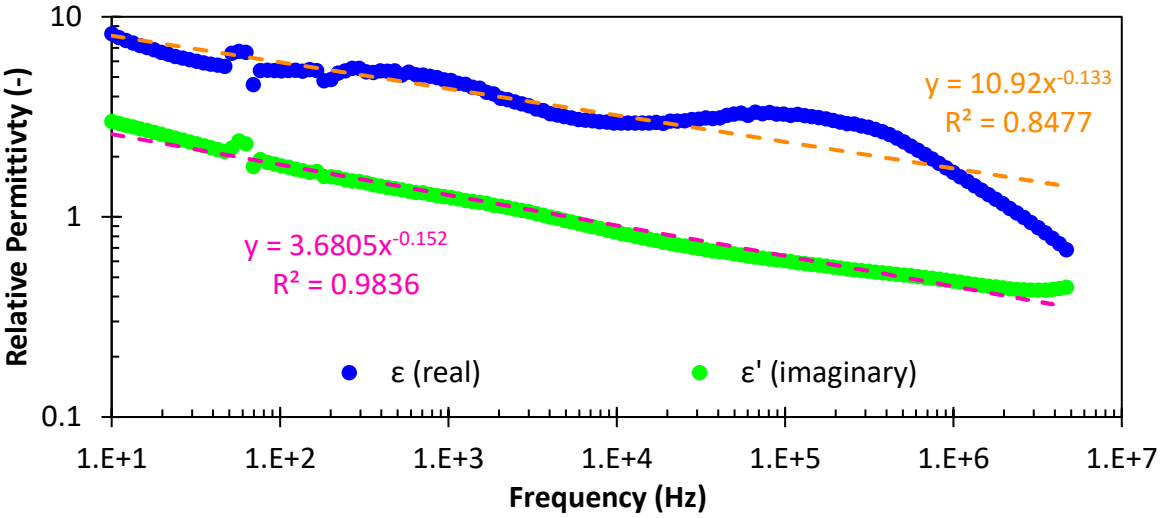

Figure 8-5. The relative permittivity of the alumina layer as a function of frequency. The real component is greater than the imaginary one, classifying this material as a lossy dielectric. As noted in Figure 8-4, the slight divergence of the permittivity from the power law at high frequencies is typical of the universal dielectric response [8:6].

8.5. Universal Dielectric Response

However, unlike typical dielectric measurements of alumina, the microsputtered capacitor has a frequency dependence in the real part of the permittivity and a significant imaginary part to

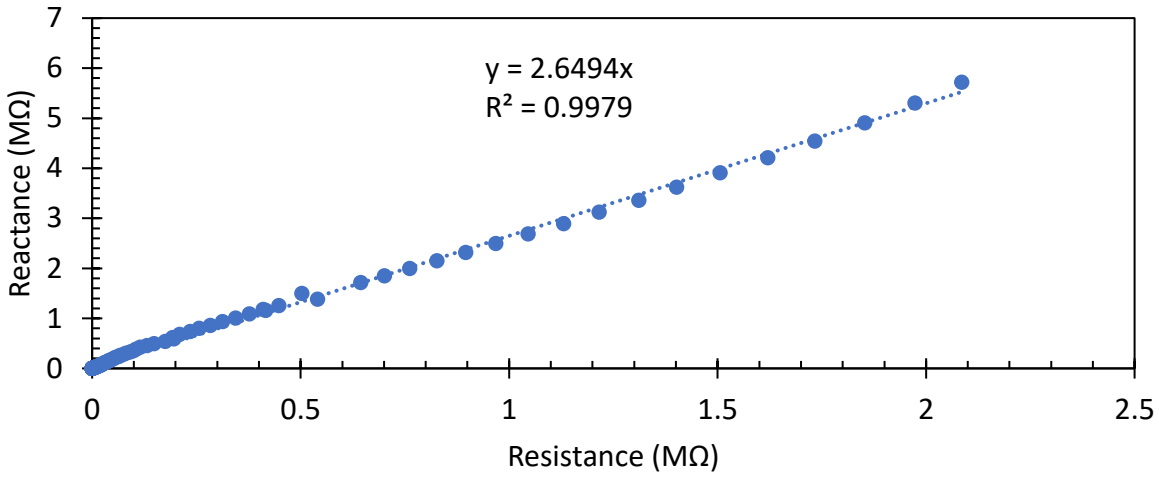

Figure 8-6. A Bode-Bode plot of the frequency response of the capacitor, from 10 Hz to 5 MHz. The relationship between the reactance and resistance is linear, which is characteristic of the universal dielectric response. The reactance is greater than the resistance, showing that the device acts primarily as a capacitor, not a resistor.

the permittivity. Both phenomena, and particularly the presence of a power law in both real and imaginary parts, with identical exponents and similar prefactors to both parts (Figure 8-6), has been seen in a wide variety of dielectrics, and is referred to as the universal dielectric response. Usually, it appears in heterogeneous dielectrics, i.e., those with both dielectric and conductive components [8:12].

The universal dielectric response has been attributed to the interaction between capacitive elements and conductive elements within the dielectric. At a microscopic level, the dielectric is not homogenous; there are dielectric and conductive elements. This heterogeneity, likely due to the presence of grains and nanoparticles discussed in Chapter 4, can be modelled as an electrical network. Each element (i.e., dielectric or conductive nanoparticle) acts as a single link (capacitive or resistive, respectively) in an electrical network. As the frequency increases and the impedance of the capacitive elements decreases, more current flows through the capacitive elements. This shift to the capacitive elements has the effect of decreasing the effective resistance through the conductive regions and increasing the total current flow. Given that the microsputtered dielectric film is porous and comprised of nanoparticles, it is not surprising to see this behavior in the microsputtered capacitor.

Specifically, [8:12] suggests the following equations for the resistance and impedance, if we model the system as a resistor and capacitor *in series*:

$$R = (\omega\epsilon\epsilon_0)^{-\alpha}\sigma^{\alpha-1}\cos\left(\frac{\alpha\pi}{2}\right)\left[\sin\left(\frac{\alpha\pi}{2}\right)+\cos(\frac{\alpha\pi}{2})\right] \quad (8\text{-}2)$$

$$Z = (\omega\epsilon\epsilon_0)^{-\alpha}\sigma^{\alpha-1}\sin\left(\frac{\alpha\pi}{2}\right)\left[\sin\left(\frac{\alpha\pi}{2}\right)+\cos(\frac{\alpha\pi}{2})\right] \quad (8\text{-}3)$$

where R and Z are the real and imaginary parts of the impedance of the material (or equivalently, the resistance and reactance of the in-series resistor and capacitor), α is the fraction of the material that is dielectric, σ and ϵ are the conductivity and real permittivity of the conductive and dielectric components of the material, respectively, and ϵ_0 is the permittivity of vacuum. From the frequency dependence of R and Z (Figure 8-3), we can estimate $\alpha \sim 0.85$, and, substituting in for $\alpha = 0.85$ and $\epsilon_0 = 8.84 \times 10^{-12}$, we find:

$$R = 8.94 \times 10^{7} (\mathrm{F}^{-0.85}\mathrm{m}^{0.85})\, \epsilon^{-0.85}\sigma^{-0.15}\omega^{-0.85} = 7.53 \times 10^{7}\,\Omega\,\mathrm{Hz}^{0.85}\omega^{-0.85} \qquad (8\text{-}4)$$

$$Z = 3.72 \times 10^{8} (\mathrm{F}^{-0.85}\mathrm{m}^{0.85})\, \epsilon^{-0.85}\sigma^{-0.15}\omega^{-0.85} = 2.00 \times 10^{8}\,\Omega\,\mathrm{Hz}^{0.85}\omega^{-0.85} \qquad (8\text{-}5)$$

With the prefactors of the right-hand sides of Equations 8-4 and 8-5 derived from the data of Figure 8-4 (and adjusted for the conversion to angular frequency)

We can thus conclude, by dividing the prefactors of the right sides of Equations (8-4) and (8-5) by the prefactors of the middles of those equations, that that $\epsilon^{-0.85}\sigma^{-0.15} \sim 0.68 \pm 0.15\ \mathrm{S}^{-0.15}\mathrm{m}^{0.15}$.

The power-law dependence of the universal dielectric response has also been seen in porous anodized alumina—another form of porous alumina. Like our films, porous anodized alumina exhibits the same behavior over a wide range (mHz-GHz) of frequencies [8:13]. It is hypothesized that water vapor in the air may condense to fill the pores and act as the conductive element.

In our case, if the dielectric element is pure alumina, with relative permittivity of ~10, then the conductive element has a conductivity of approximately 7×10^{-6} – 1.4×10^{-4} S·m^{-1}. We posit that in our case the conductive element is also pure water, condensed from vapor in the atmosphere. Water, unlike any common alumina compound (e.g., aluminum, aluminum oxide, aluminum nitride) has a conductivity of approximately 10^{-4} S·m^{-1}, which falls within this range.

8.6. Conclusion

This chapter described the first demonstration of a multi-material microsputtered device, namely, a functional electrical capacitor. The microsputtered alumina was shown to have electrical properties similar to those of traditionally manufactured alumina (i.e., bulk resistivity of 10^{11} Ω·m, relative permittivity ~10 for low-frequency signals, breakdown voltage of ~11 GV·m^{-1}). The microsputtered film also demonstrates the universal dielectric response—common to many heterogenous dielectrics. Based on the frequency response of the impedance, it was concluded that this material is 85% alumina (based on the exponent of the power law), with nanopores filled with pure water.

8.7. References

[8:1] Li Q, Yu YH, Singh Bhatia C, Marks LD, Lee SC, Chung YW. Low-temperature magnetron sputter-deposition, hardness, and electrical resistivity of amorphous and

crystalline alumina thin films. Journal of Vacuum Science & Technology A: Vacuum, Surfaces, and Films. 2000 Sep;18(5):2333-8.

[8:2] Carreri FC, Bandorf R, Gerdes H, Vergöhl M, Bräuer G. Highly insulating alumina films by a bipolar reactive MF sputtering process with special arc handling. Surface and Coatings Technology. 2016 Mar 25;290:82-6.

[8:3] Lin HC, Ye PD, Wilk GD. Leakage current and breakdown electric-field studies on ultrathin atomic-layer-deposited Al_2O_3 on GaAs. Applied physics letters. 2005 Oct 31;87(18):182904.

[8:4] Mollá J, Moreno R, Ibarra A. Effect of Mg doping on dielectric properties of alumina. Journal of applied physics. 1996 Jul 15;80(2):1028-32.

[8:5] Birey H. Thickness dependence of the dielectric constant and resistance of Al2O3 films. Journal of Applied Physics. 1977 Dec;48(12):5209-12.

[8:6] Gershon D, Calame JP, Birnboim A. Complex permittivity measurements and mixing laws of porous alumina. Journal of Applied Physics. 2001 Jun 15;89(12):8117-20.

[8:7] Molla J, Gonzalez M, Vila R, Ibarra A. Effect of humidity on microwave dielectric losses of porous alumina. Journal of applied physics. 1999 Feb 1;85(3):1727-30.

[8:8] Jimenez-Saez A, Schubler M, Krause C, Pandel D, Rezer K, Vom Bogel G, Benson N, Jakoby R. 3D Printed Alumina for Low-Loss Millimeter Wave Components. IEEE Access. 2019 Jan 1;7:40719-24.

[8:9] Jonscher AK. The ‘universal’ dielectric response. nature. 1977 Jun;267(5613):673-9.

[8:10] Ngai KL, Jonscher AK, White CT. On the origin of the universal dielectric response in condensed matter. Nature. 1979 Jan;277(5693):185-9.

[8:11] Jonscher AK. The universal dielectric response and its physical significance. IEEE Transactions on Electrical Insulation. 1992 Jun;27(3):407-23.

[8:12] Bowen CR, Almond DP. Modelling the 'universal' dielectric response in heterogeneous materials using microstructural electrical networks. Materials Science and Technology. 2006 Jun 1;22(6):719-24.

[8:13] Tahir M, Mehmood M, Nadeem M, Waheed A, Tanvir MT. On the variation in the electrical properties and ac conductivity of through-thickness nano-porous anodic alumina with temperature. Physica B: Condensed Matter. 2013 Sep 15;425:48-57.

Chapter 9 – **Conclusions**

9.1. Accomplishments

This thesis on microplasma sputtering for agile electronics lies at the intersection of manufacturing, material science, and plasma physics. By combining insights in those fields and others, we have

- Outlined methods to achieve, in practical terms, hundreds of microns-level, in-plane features using electric fields and masks to shape the deposition
- Used a high-collisionality, high-energy plasma to produce adhesion-enhanced deposits that greatly surpass the adhesion of traditionally sputtered films
- Produced films at room temperature and atmospheric pressure with 80% of bulk electrical conductivity by harnessing electric fields and nanoparticles, with no pre or postprocessing
- Demonstrated the use of an engineered gas mixture to double the sputter yield and allow for reactive sputtering of alumina
- Demonstrated our technology in the atmospheric pressure coating of microwires, attaining fully azimuthal coverage from depositing in one direction, with no rotation
- Produced fully-printed capacitors, with the material qualities of traditionally produced gold and porous alumina

These together have served as a demonstration of the potential of microsputtering as a tool in the arsenal of the manufacturer. When microsputtering technology is mature, it will allow electronics manufacturing to undergo the same revolution that structural manufacturing has in the last decade—low-volume, low-cost customized printing. However, there is work to do before this technology is mature. Some of it, of course, is related to reliability—the ability to produce our best results consistently and reliably. Other parts involve integration for a microsputtering system with existing additive manufacturing technology. This would allow developers to take advantage of a decade of maturity when designing the ancillary systems (e.g., mobility systems, computer control) of microsputtering, and allow for the easier integration of microsputtered features into 3-D printed plastic devices.

9.2. Future Work

The microsputterer, as it stands, is a proof-of-concept of atmospheric pressure sputtering as a reasonable method to produce high-quality films, suitable for electronics, without a clean room, pre- or post-processing, or elevated temperatures. In fact, the material quality of microsputtered films, in many ways (e.g., electrical conductivity, adhesion, dielectric strength), meets or (in adhesion and dielectric strength) surpasses the quality of traditionally sputtered films. However, the technology is not yet mature, and thus, to improve the microsputterer or to harness its abilities, some fundamental areas of interest may be:

9.2.1. Chapter 3- Resolution

Better modelling of the plasma effects and fluid effects, and tighter tolerances in manufacturing, might lead to a more concentrated flow of sputtered material, and thus higher resolution and throughput. Specifically, as the microsputtering system stands now, focusing confines the plasma to a line approximately 1 mm in width, which is further defined by the aperture. If further hydrodynamic and electromagnetic focusing could confine the plasma to 10 μm, the yield (measured in nm/s, linear film thickness growth) could improve hundredfold, even without increasing the sputtering rate and the volumetric deposition rate.

9.2.2. Chapter 4- Adhesion

The ability to produce of nanoparticles in an atmospheric plasma can also be controlled and harnessed. Depositing nanoparticles in specific patterns can be useful to modulate their optical or plasmonic effects (e.g., camouflage, optics), or as a single-material adhesion layer in traditional cleanroom environments. Nanoparticles can also be harnessed to produce strain gauges. If the electrical behavior of a microsputtered film is dominated by the current's movement between nanoparticles, using current to measure the underlying substrate's deformation is possible. This is useful both in direct-write printing and outside of it.

9.2.3. Chapter 5- Electrical Conductivity

The dependence of microsputtered gold films' electrical conductivity on the substrate voltage can be used to fine-tune the electrical properties of films. Given that the conductivity of gold can be modulated by modifying the electric field, a single material (e.g., gold) can be used as an interconnect or resistor, or anything in between, simply by modifying process parameters. This could lead to interesting gradients for integrated electronic components. In particular, complex broadband antenna shapes may be possible by varying the electrical properties, rather than the width of the trace.

Additionally, while the electrical properties of the film due to variations in the nanostructure have been examined, it would be illuminating to investigate the mechanical properties—is the film under any strain? One would assume that the deposition of nanoparticles without any annealing would lead to minimal strain, but investigations should be done to elucidate this matter.

9.2.4. Chapter 6- Ion Energy

Similarly, by adjusting the gas flow, different aluminum-based compounds could be produced (e.g., oxygen-rich alumina in an oxygen-rich atmosphere, oxygen-poor alumina in a low-oxygen atmosphere, aluminum nitride in pure nitrogen, aluminum in a mixture of noble gases) with a smooth gradient between different parts of the feature. Hydrogen can also be used to prevent oxidation. In particular, aluminum nitride would be a useful semiconductor, albeit a wide bandgap one. A nitrogen atmosphere, mixed with argon for improved sputtering and hydrogen to reduce any oxygen contamination, could produce it well. To further control the gas content, an enclosure may be necessary, to ensure that the sputtering atmosphere matches the incoming gas.

Additionally, this thesis has demonstrated an improved sputtering rate by using nitrogen as a dielectric gas (i.e., a gas that increases the electric field necessary for breakdown by absorbing electron energy). Diatomic nitrogen absorbs energy through its rotational mode at 3-4 eV of electron energy. If a mixture of gases could be found, each absorbing electron energy at a different range, a more perfect dielectric gas could be made. This would both be useful for our purposes (i.e., to improve the sputtering rate further), as well as for industrial uses of dielectric gases. Most common dielectric gases are toxic, as discussed in section 6.5; a safer mixture would be helpful.

Specifically, it appears that a mixture of hydrogen and nitrogen is a good choice. Hydrogen can be excited rotationally at ~1 eV, and electronically at ~8 eV [9:1]. The combination of nitrogen and hydrogen thus will absorb many electron energies between 1-10 eV, below the ionization threshold. However, care must be taken to avoid igniting the hydrogen; it is recommended that oxygen not be present in the plasma wherever possible. Additionally, the fraction of hydrogen should be kept low. A mix of 5% hydrogen in nitrogen is an easily procured and relatively safe gas blend; it should be used initially, with oxygen or water vapor (as an oxygen source) added as necessary for any desired oxidation. Water vapor is also effective at absorbing electron energy from electrons with approximately 10 eV of energy [9:2], further increasing the electric field. The exact mixture and the exact proportions should likely be found experimentally.

9.2.5. Chapter 8 - Capacitor

This thesis has demonstrated microsputtering printing of two kinds of materials: an electrical conductor and a dielectric. A semiconductor would add more to the toolbox. Amorphous

silicon or selenium are reasonable candidates; both are semiconducting in the presence of light. However, an oxygen-free environment would be necessary to prevent the oxidation of silicon, and again, nitrogen with argon and hydrogen is the best candidate. Silicon is less malleable than selenium and would likely need a modified wire feed to accommodate rigid sticks of silicon. Aluminum nitride, as described earlier, could also be used.

If it becomes necessary to sputter dielectrics directly, an RF plasma could be introduced, albeit at the cost of increasing complexity of the apparatus and preventing the use of the electrostatic focusing system. Thus, it is probably simpler to sputter conductors and synthesize compounds in the plasma.

Compounds can be easily created by simultaneously sputtering multiple elements (whether as an alloyed wire or multiple plasmas reacting with multiple elemental wires). These elements will combine in the high-energy plasma to produce high-quality compounds (e.g., ceramics); the plasma will ensure that they mix well.

A high-quality film that observes the universal dielectric response can be harnessed for novel filters; a capacitor whose reactance has a tunable power-law dependence on the frequency allows the customization of filters. Although a dense dielectric has a stronger power-law dependence (i.e., an exponent of -1, rather than something between 0 and -1), the tunability of porous microsputtered alumina may still be valuable. The exact structure of the alumina likely depends on the production of nanoparticles, as described in Chapter 4; adjusting the process parameters can adjust the porosity of the nanoparticles and the exponent of the power law.

Additionally, this thesis has demonstrated a simple electrical device (a capacitor) fully microsputtered. More devices, such as antennae, pressure sensors, temperature sensors, and actuators, can be printed using similar methods. Future devices can take advantage of the variety of substrate choices that are available (e.g., 3-D printed, non-planar, flexible).

Outside of microplasmas, there are several directions in which this research can be taken or used:

- Although substrate heating is a valid and well-studied way to enhance the energy of impinging atoms, our research has shown that a plasma, combined with an electric field, has the same effect. This can be used to allow for other processes that require high impinging ion energy (e.g., chemical reactions) on temperature sensitive substrates.

- Gas blends could have their place in traditional sputtering. Although, as described in Chapter 6, insufficient ion energy and runaway ionization are not typically problems in

traditional sputtering, the use of a gas blend to tailor the ion energy might be helpful to allow for low-vacuum sputtering.

Beyond the application of this thesis to microsputtering, it has also involved a return to first principles for one of the workhorses of CMOS manufacture—sputtering. It serves as a reminder that industrial practice and basic research have much to learn from each other, and that a deep physical understanding of well-used processes is highly valuable, to allow for the expansion and extension of the state-of-the-art.

9.3. References

[9:1] Schulz GJ. Resonances in electron impact on diatomic molecules. Reviews of Modern Physics. 1973 Jul 1;45(3):423.

[9:2] Jain A. Theoretical study of the total (elastic+ inelastic) cross sections for electron-H2O (NH3) scattering at 10-3000 eV. Journal of Physics B: Atomic, Molecular and Optical Physics. 1988 Mar 14;21(5):905.